TECHNISCHE UNIVERSITÄT MÜNCHEN

Fakultät für Chemie

Croconaine-based nanoparticles for efficient optoacoustic imaging and tumor theranostics

Nian Liu

Abstract

Near-infrared (NIR) light-triggered optoacoustic tumor imaging and phototherapy are valuable oncology techniques due to high image contrast, noninvasiveness, and spatiotemporal selectivity. Croconaine dyes, constitute superior NIR probes, exhibiting high optoacoustic generation efficiency, photothermal conversion efficiency, and good photostability, all of which can be leveraged to achieve precise diagnosis and efficient treatment of tumors. In this thesis, three croconaine-derived dyes with different maximum absorption wavelengths were synthesized and formulated into nanoparticles. First, we constructed croconaine-derived CR760 nanoformulations using facile synthesis for optoacoustic imaging-guided photothermal therapy of subcutaneous tumors. Enabled by the excellent optical absorption properties, and an active targeting effect (*via* an RGD peptide), CR760RGD-NPs could actively bound to certain tumor types, and were also suitable for both optoacoustic imaging and tumor elimination *via* NIR laser irradiation. Secondly, to achieve efficient optoacoustic imaging of challenging brain tumors, we developed croconaine-derived CR780 nanoparticles with a slightly longer absorption maxima. Through nanoformulation and ligand targeting, ultrasmall CR780RGD-NPs were able to pass the blood brain barrier and efficiently target the brain tumor area, allowing visualization by optoacoustic imaging. Finally, because the absorption peaks of both CR780 and CR760 fall mainly below 800 nm and are still affected by strong background absorbance from tissue and hemoglobin, croconaine-derived CR880 nanoparticles with 880 nm absorption peak were developed to enable deeper tissue penetration for tumor imaging, and efficient photothermal therapy. Through independent preclinical toxicity studies, we demonstrated that the croconaine based nanoparticles are safe for *in vivo* application. In summary, we have

developed chemically tuned croconaine-derived nanoparticles for specific applications in cancer diagnosis and therapy.

Zusammenfassung

Nahinfrarot (NIR)-lichtgetriggerte optoakustische Tumorbildgebung und Phototherapie sind wertvolle onkologische Techniken aufgrund des hohen Bildkontrasts, der Nichtinvasivität und der räumlich-zeitlichen Selektivität. Croconain-Farbstoffe stellen überlegene NIR-Sonden dar, die eine hohe optoakustische Erzeugungseffizienz, photothermische Umwandlungseffizienz und gute Photostabilität aufweisen, die alle für eine präzise Diagnose und effiziente Behandlung von Tumoren genutzt werden können. In dieser Arbeit wurden drei von Croconain abgeleitete Farbstoffe mit unterschiedlichen maximalen Absorptionswellenlängen synthetisiert und zu Nanopartikeln formuliert. Zunächst haben wir CR760-Nanoformulierungen aus Croconain durch einfache Synthese für die optoakustische Bildgebung-geführte photothermische Therapie von subkutanen Tumoren hergestellt. Durch die exzellenten optischen Absorptionseigenschaften und den aktiven Targeting-Effekt (über ein RGD-Peptid) konnten die CR760RGD-NPs aktiv an bestimmte Tumortypen binden und waren sowohl für die optoakustische Bildgebung als auch für die Tumorelimination durch NIR-Laserbestrahlung geeignet. Um eine effiziente optoakustische Bildgebung von anspruchsvollen Hirntumoren zu erreichen, entwickelten wir zweitens von Croconain abgeleitete CR780-Nanopartikel mit einem etwas längeren Absorptionsmaximum. Durch Nanoformulierung und Liganden-Targeting konnten die ultrakleinen CR780RGD-NPs die Blut-Hirn-Schranke passieren und den Hirntumorbereich effizient anvisieren, was eine Visualisierung durch optoakustische Bildgebung ermöglichte. Da das Absorptionsmaximum sowohl von CR780 als auch von CR760 hauptsächlich unterhalb von 800 nm liegen und immer noch durch eine starke Hintergrundabsorption von Gewebe und Hämoglobin beeinträchtigt werden, wurden von Croconain abgeleitete CR880-Nanopartikel mit einem Absorptionsmaximum von 880 nm entwickelt, um eine tiefere Gewebepenetration für

die Tumorbildgebung und eine effiziente photothermische Therapie zu ermöglichen. Durch unabhängige präklinische Toxizitätsstudien haben wir gezeigt, dass die Croconain-basierten Nanopartikel sicher für die in vivo Anwendung sind. Zusammenfassend haben wir chemisch abgestimmte, von Croconain abgeleitete Nanopartikel für spezifische Anwendungen in der Krebsdiagnose und -therapie entwickelt.

Table of content

1 Introduction

1.1 Optoacoustic imaging

The concept of the optoacoustic effect was first reported in 1976 and is the basis of the generation of an optoacoustic signal.[1] Here optoacoustic contrast agents absorb the optical energy of a pulse laser and simultaneously convert it into thermal energy, undergoing thermoelastic expansion and generating ultrasonic signals (**Figure 1.1**).[2, 3] The optoacoustic effect has been used as an alternative to optical imaging to achieve higher resolution, deeper tissue penetration, and greater image contrast, and can in some cases overcome the disadvantages of low image quality caused by photon scattering in conventional optical imaging.[4] Therefore, this technique has attracted much attention for preclinical and clinical applications. The optoacoustic method can effectively visualize the structure and function of biological tissues, offering the necessary information to study the morphological structure, physiological features, metabolic functions, and pathological characteristics of tissues, especially for the early detection of cancer.[5]
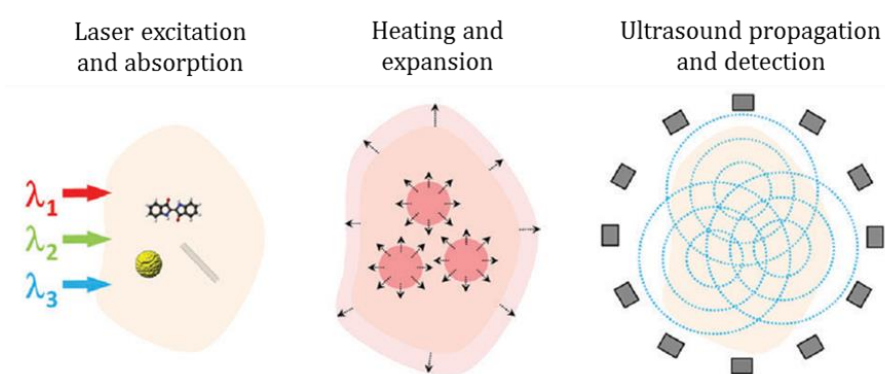
Figure 1.1. Schematic illustration of the optoacoustic signal production and detection. Reproduced with permission.[3] Copyright 2017, Royal Society of Chemistry.

1.2 Multi-spectral optoacoustic tomography (MSOT)

MSOT inVision 256-TF (iThera Medical, Munich, Germany) serves as the *in vivo* optoacoustic system for small animals (**Figure 1.2a**).[6] Benefiting from the advantages of high resolution, high penetration depth, detailed molecular information, and an easy unmixing process, it has been used for many biological applications, such as cancer, neuroimaging, and cardiovascular disease.[7] Throughout the MSOT scanning is operated from 680 to 980 nm with a step size of 10 nm and 10 signal averages. Nanosecond illumination of the sample uniformly from 5 different directions is accomplished using a one to ten (five pairs) fiber bundle. The generated acoustic signals are acquired using a 256-element transducer array (5 MHz center frequency) with 270-degree angle coverage and 40 Ms/sec DAQ sampling rate. Acquired sinogram data is initially filtered using a Chebyshev filter having a bandwidth of 0.1-8 MHz. The filtered sinogram data is used to reconstructing the mice/phantom image using a model-based reconstruction with a least squares QR inversion method running for 100 iterations. The model-based reconstructions are performed at all the wavelengths i.e. 680 nm to 980 nm with a step size of 10 nm. The reconstructed images are used to detect the contrast agents' signal using the contrast agents' reference spectral information, the contrast agents' signal is detected using a linear regression approach (unmixing method) (**Figure 1.2b**).
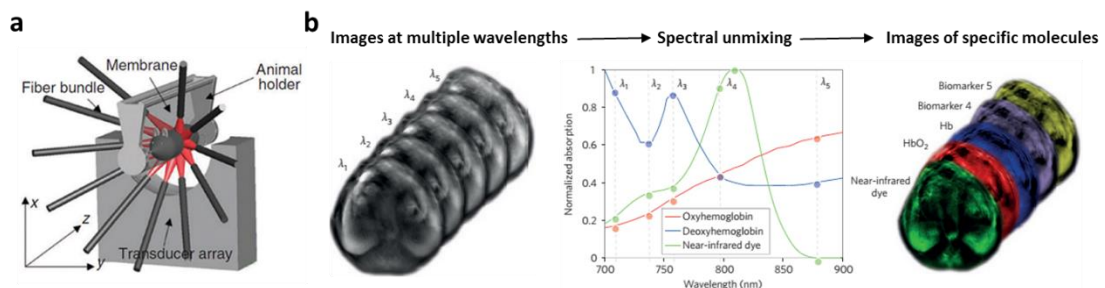
Figure 1.2. (a) Schematic of the real-time cross-sectional imaging system for *in vivo* MSOT imaging. (b) Images processing steps of MSOT imaging. Reconstructed images

at multiple wavelengths are associated with spectral unmixing algorithms to distinguish specific molecules. Reproduced with permission.[6] Copyright 2015, Nature Publishing Group.

1.3 Optoacoustic contrast agents

1.3.1 Endogenous agents

Numerous light-absorbed agents exist in biological tissue, such as hemoglobin, melanin, and lipids. These chromophore-containing molecules have characteristic absorption spectra in the visual and NIR range. Optoacoustic imaging enables the relative quantification of endogenous chromophores, thereby providing insight into the physiological changes that occur in certain disease states.[8-10] In particular, the quantification of hemoglobin concentration and oxygen saturation can be differentiated by optoacoustic imaging, which provides important information regarding tumor angiogenesis, ischemia, hypoxia, or hypoxemia physiological states.[11-13] Melanin with strong optical absorption makes it possible to sensitively image pigmented lesions, melanoma, and hair follicles.[14] Furthermore, lipid consumption in some certain areas (sebaceous glands and arterial plaques) can be characterized by optoacoustic imaging at wavelengths from 930 and 1210 nm.[15] However, endogenous chromophores are only available for imaging a limited range of biological processes due to the weak image contrast.[5] Therefore, it is necessary to employ exogenous contrast agents to enable significantly richer profiling of biological activities.

1.3.2 Exogenous agents

Exogenous agents can enhance the optoacoustic image contrast ratio and improve the resolution by altering the optical and acoustic properties of local tissue, thus remarkably boosting the image output.[7] An ideal optoacoustic agent should have a high molar absorption coefficient with a narrow NIR spectral profile, low quantum yield, and high optoacoustic generation efficiency (OGE) for more accurate and

sensitive spectral unmixing.[16] Moreover, optoacoustic imaging agents should have good photostability, target-specific ability, biocompatibility, and minimal toxicity.[16] A variety of inorganic and organic contrast agents has been developed for optoacoustic contrast enhancement (**Table 1.1**).[17] Metal-based inorganic contrast agents have strong NIR absorption contrast and excellent photothermal conversion ability due to localized surface plasmon resonance.[17-21] However, inorganic agents undergo structural deformation (shape and size changes) upon light irradiation, which alters their optical behavior and their photostability.[22] Carbon nanostructures exhibit broad NIR absorption, as well as facile synthesis and easy functionalization, thus they are still one of the promising optoacoustic agents even though the slightly lower molar-extinction coefficients.[23, 24] However, concern has been expressed regarding the long-term toxic side effects of metal and carbon-based agents due to low biodegradability and long deposition time in the body after systemic administration.[25] Organic dyes can overcome the challenges of inorganic agents because their chemical structures can be easily modified, and they often exhibit good biocompatibility, easy metabolism, rapid clearance, and low toxicity. [26]
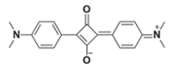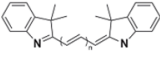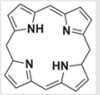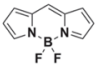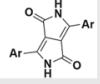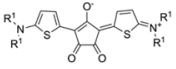
Table 1.1. Optoacoustic contrast agents and their advantages and disadvantages

Materials	Types	Advantages	Disadvantages
Inorganic	Gold nanoparticles, Palladium nanoplates, CuS, WS_2, MoS_2, Bi_2S_3, Co_9Se_8 Carbon nanostructure	Tunable physiochemical properties	Non-biodegradability; suboptimal photothermal stability, toxicity
Organic	Cyanines, Porphyrin, Squaraines, BODIPY, Diketopyrrolopyrrole, Croconaine	Easy chemical structure tuning, good biocompatibility, low-toxicity, easy metabolism, and relatively low cost	Low aqueous solubility, poor photostability

Various organic dyes with NIR absorbance, such as cyanine, squaraine, BODIPY, and tetrapyrrole, have been widely developed for the application of optoacoustic imaging (**Table 1.2**).[26] Cyanine dyes, consisting of aromatic nitrogen-containing heterocycles, are most widely used for optoacoustic imaging, such as IR780 iodine,

IR820, IRDye800CW, IR825, and FDA approved indocyanine green (ICG).[27-29] However these commercially available cyanine dyes have major drawbacks as an optoacoustic contrast agent because of poor photostability and low optoacoustic generation efficiency.[30] Squaraine dyes exhibit sharp absorption peaks and strong NIR emission, but their self-aggregation and poor water-solubility limit their *in vivo* application.[31, 32] BODIPY dyes display strong NIR fluorescence with high quantum yield, making them suitable for fluorescent imaging, although structural modifications are used to obtain the red-shifted and water-soluble compounds.[33, 34] Tetrapyrole structures such as porphyrin and phthalocyanines belong to the class of photosensitizers, and are widely used as photodynamic therapy (PDT) agents in treating cancers.[35] Thus, these structures have lower molar extinction coefficients, which are not good for producing efficient optoacoustic signals.[36, 37] Croconaine dyes and their derivatives could be the most promising optoacoustic agents because of thermal stability, photobleaching resistance, solvatochromism, and spectral tenability.[38]

Table 1.2. Common organic dyes and their photophysical properties (The parameters of photostability: level 1 (very low), level 9 (very high))

Organic dyes	Basic structure	Abs$_{max}$(nm)	Em$_{max}$(nm)	Molar absorption coeffcient	Photostability
Squaraine		650-800	800-1000	>10^5	Level 4
Cyanines		700-900	800-1000	=10^5	Level 4
Porphyrin		600-800	700-900	>10^5	Level 6
BODIPY		600-900	700-1100	>$0.8*10^5$	Level 8
Diketopyrrolo pyrrole		550-750	600-900	>$0.25*10^5$	Level 8
Croconaine		680-1000	800-1000	>$2*10^5$	Level 9

1.4 Croconaine

1.4.1 Concept and optical properties

The first croconaine derivative was described in 1970[38] and since then many derivatives have been developed, mainly for use in optical data storage,[39] xerography,[40] biosensing,[41-44] and photovoltaic cells.[45] Croconaines are pseudooxocarbon dyes derived from croconic acid with a strong electron-withdrawing character.[38] They can be used to synthesize dyes with "donor-acceptor-donor (D-A-D)" type chromophores by a condensation reaction between croconic acid and electron-rich aromatic and heteroaromatic compounds or heterocyclic methylene bases.[46] The resulting mesoionic structures give rise to strong π-π transitions. Croconaine dyes can be easily modified by varying the steric and electronic characteristics of the donor moiety. Generally, croconaine dyes are either symmetric (D1-A-D1 type) or asymmetric(D1-A-D2 type),[46, 47] and have good optical properties, such as low photobleaching, strong solvatochromism, and a tuneable absorption spectrum.

(1) Physicochemical properties: The absorption spectra of croconaines display strong solvatochromism, i.e. where the absorption peaks are shifted by the solvent polarity. Compared with squaraine, the croconaine ring is more strongly electron-withdrawing, and therefore the absorption peak of croconaines is redshifted by approximately 100nm relative to similarly structured squaraines.[38] This redshifting occurs for two reasons: the strong π-electrons in the central region of the molecule and the lactone group act as a super-absorbing group, and the reversal of the overall stereological configuration of the benzofuran.

(2) Self-aggregated properties: Croconaines have good solubility in organic solvents, such as tetrahydrofuran, dichloromethane, trichloromethane, acetonitrile, methanol, acetone, ethanol, DMF, but are difficult to dissolve in water. There exist strong van der Waals forces between croconaine molecules, which are not only hydrophobic in nature, but tend to result in self-aggregation in solution. In different solutions and solid media, croconaines also can form aggregates, where their absorption peaks are very different from the monomers. Furthermore, most of croconaine dyes

which we synthesized exhibit self-aggregation (H-aggregation or quenching) (**Figure 1.3**).[48]
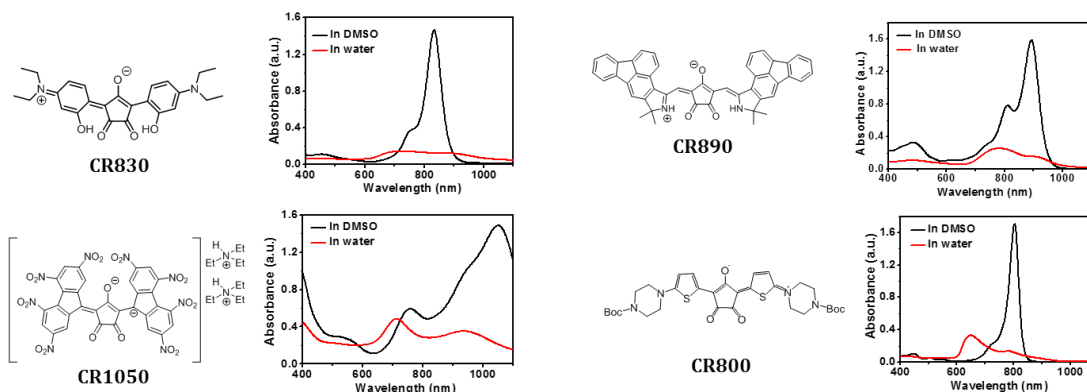
Figure 1.3. The synthesized croconaine dyes and corresponding optical spectrum in DMSO and water.

(3) Photostability: Under light irradiation, the structure of dye molecules can become irreversibly changed, resulting in color change or fading. The photobleaching of cyanine dyes is mainly caused by light-induced oxidation.[49] In the energy transfer process, the dye molecule acts as a singlet sensitizer activating oxygen which usually exists in a triplet ground state, where singlet oxygen can oxidize the dye structure. Therefore, if the structure of the dye molecules can delay this process, the photostability of the dyes can be improved. Compared to straight-chain cyanine dyes, croconaine dyes possess conjugated units in a ring system, which provide the structural rigidity enhancement and spatial potential resistance to prevent the generation of singlet oxygen, as well as improve the photostability.[50]

1.4.2 Biomedical application

Benefiting from the D-A-D type structure, croconaine dyes display efficient intramolecular charge transfer ability to generate strong NIR absorption and high molar extinction coefficients, thus allowing for high-efficient *in vivo* photo-theranostics application. However, most of the proposed croconaine derivatives suffer from H-aggregation and low solubility and therefore are not suitable for *in vivo* application.[48] A reduction in the structural stacking and dye aggregation can be achieved by chemical

modifications. At the time of writing, and to the best of our knowledge, there exist three reported croconaine structures developed into nanoformulations for *in vivo* optoacoustic imaging and theranostics. These are CR780,[51] Croc,[52] and A1094,[53] which are all outlined below.

CR780 was reported in 2008.[51] With superior properties and easy modification, it has been used for many biomedical applications. Tang et al. have published a series of papers regarding cancer theranostics based on CR780. First, Tang et al. proposed polyethylene glycol (PEG) conjugated CR780 (CR780-PEG5000) for enhanced tumor accumulation and theranostics (**Figure 1.4**).[54] The PEGylated CR780 could be easily self-assembled into uniform nanostructures (17nm). After intravenous injection, it could be visualized in tumor regions by NIR fluorescence and optoacoustic imaging. Additionally, due to the good photothermal conversion efficiency, it could also be used for photothermal therapy (PTT). Tumor targeting was improved using c(RGDfK) conjugates formulated as nanoparticles. Then ^{125}I labeled RGD-CR780-PEG5000 were tested in a U87MG subcutaneous tumor model. The tri-model imaging (SPECT, fluorescence, and optoacoustic) clearly showed that the active targeting effect of ^{125}I labeled RGD-CR780-PEG5000 compared to the non-targeted group.[55] Later, to achieve combined therapy with chemodrugs guided by optoacoustic imaging, Tang et al. designed two strategies for chemophotothermal therapy of cancerous tumors. One was to prepare the trimeric prodrugs by linking chemodrug and CR780 via a GSH-sensitive disulfide linker and then encapsulated into folic acid–PLGA NPs.[56] Due to the high concentration of GSH inside cancerous cells and photothermal-acceleration, the disulfide bonds were easily cleaved, thereby releasing the chemodrugs under laser irradiation. Meanwhile, strong optoacoustic signals from the nanoformulations were used to monitor the tumor accumulation and further guide chemophotothermal therapy, which showed complete tumor elimination. Another strategy that was explored was to first conjugate DOX with CR780 by Edman linkers (CED2), and then co-load CED2 and AIPH (2,2'-azobis[2-(2-imidazolin-2-yl)propane] dihydrochloride) into ROS-responsive amphiphilic block-polymer of poly(propylene sulfide)-poly(ethylene glycol) (PPSPEG).[57] These nanovesicles required dual activation for drug release. This first mode of activation employed the mild hyperthermia and tumor acidic pH condition to

degrade the Edman linkers for DOX release in the nanovesicles. The second mode of activation uses the photothermal effect to activate AIPH to generate radicals for oxidizing and disassembling the PPSPEG. *In vivo* optoacoustic imaging confirmed the efficient tumor accumulation of v-A-CED2 after intravenous injection. Thus, the photothermal effect induced on-demand chemotherapy under optoacoustic imaging guidance and can significantly inhibit tumor progression.
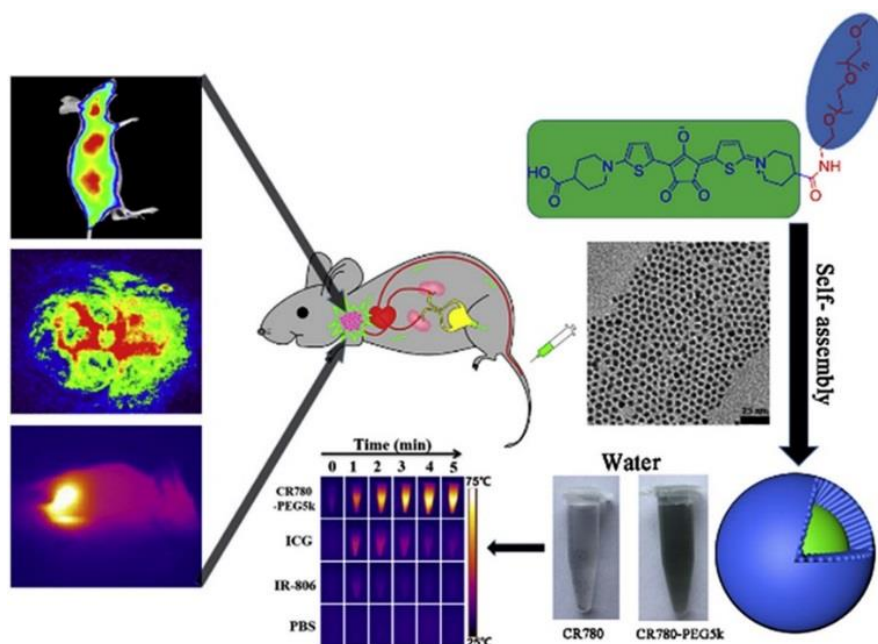
Figure 1.4. Schematic illustration of CR780-PEG5000 assembled nanoparticles for fluorescence and optoacoustic imaging-guided PTT. Reproduced with permission.[54] Copyright 2017, Elsevier.

The pH-sensitive Croc structure has been reported in 2002, which showed a pH-dependent absorption shift in ethanol.[52] To apply the hydrophobic Croc into *in vivo* application, Guha et al. first made interlocked Croc-rotaxane complexes to prevent self-aggregation of free Croc, and then encapsulated them into stealth liposomes (CroRot-SL).[58] The CroRot-SL showed similar pH-sensitive properties and good photostability, as well as exhibited the ratiometric optoacoustic imaging of acidic pH. On the other hand, Chen et al. employed human serum albumin (HSA) to be the nanocarriers to load Croc (HSA-Croc) by hydrophobic interaction.[59] Due to the unique pH-responsive absorption, it could be used for optoacoustic imaging of timely

tumor pH change, where the acidic tumor region provides enhanced optoacoustic signals (**Figure 1.5**). Moreover, compared with HSA-ICG, HSA-Croc exhibited excellent photothermal effect for the suppression of large tumors under laser irradiation.
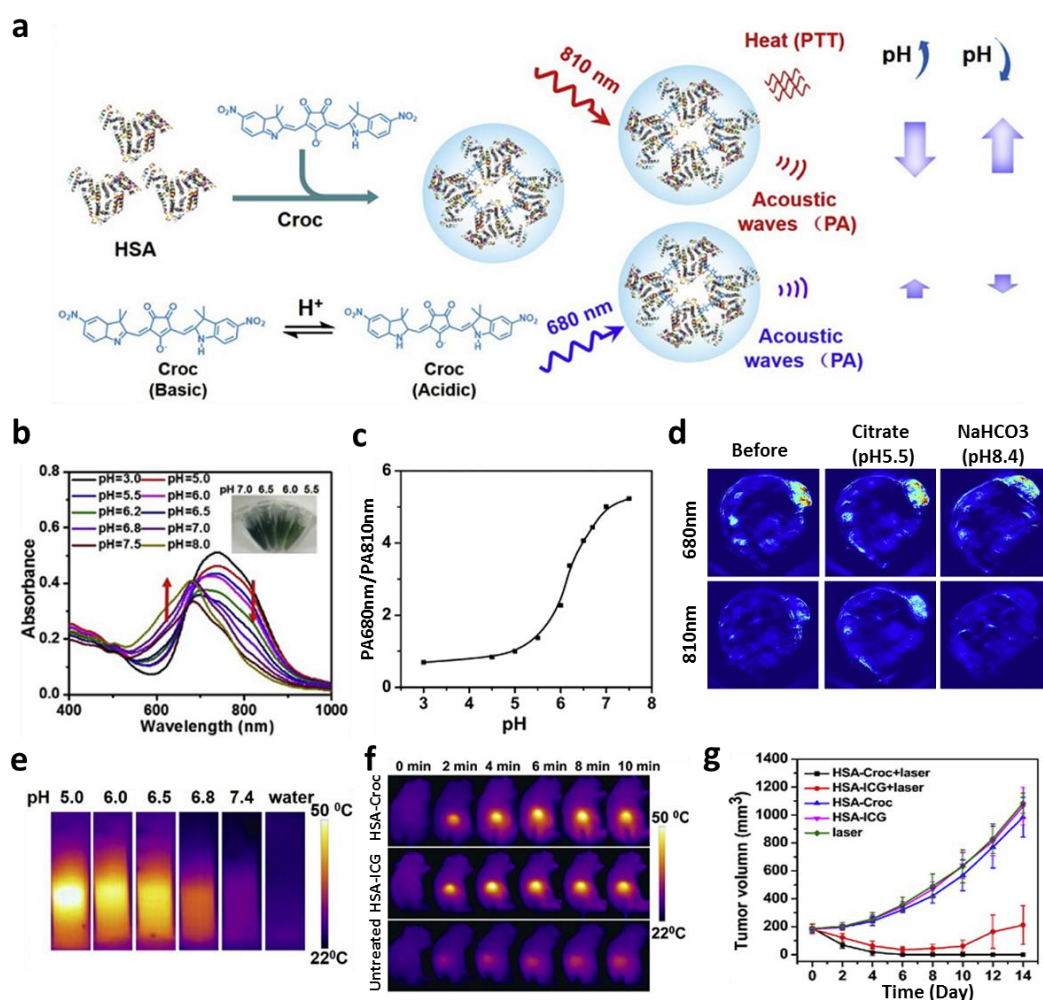
Figure 1.5. (a) Schematic illustration of HSA-Croc with pH-responsive optoacoustic signals and enhanced photothermal effect. (b) Absorption spectra of HSA-Croc in different pH buffer. (c) The ratio of PA680nm/PA810nm of HSA-Croc measured in different pH conditions. (d) *In vivo* optoacoustic imaging of tumor at 680nm and 810nm under different tumor pH conditions. (e) IR thermal images of HSA-Croc in different pH buffer under 0.5 W/cm^2 808nm laser irradiation. (f) IR thermal images of tumors with different treatments. (g) Tumor growth curves of mice with different treatments. Reproduced with permission.[59] Copyright 2016, Elsevier.

The structure of A1094 has been shown in 2003, with the specific properties of a relatively short backbone structure, a 1100nm absorption peak, and high thermal stability.[53] Liu et al. encapsulated A1094 into RGD peptide-modified hepatitis B virus core protein (RGD-HBc) for NIR-II optoacoustic imaging of brain tumor.[60] The formulated A1094@RGD-HBc exhibited the performance of aggregation-induced-absorption-enhancement (AIAE) due to the strongly absorbing conjugated chromophore. Meanwhile, A1094@RGD-HBc showed a stronger optoacoustic signal at 1200-1300nm than 900-950nm. Then the brain tumor-bearing mice were administrated with A1094@RGD-HBc to check the deep tissue imaging. Due to the nanosize and active targeting effect, A1094@RGD-HBc can bind at the brain tumor region, which can be detected from the depth of 5.9 mm under the skull. Also, ^{131}I-labeled A1094@RGD-HBc endow the SPECT properties to dual-modal imaging of glioblastoma. On the other hand, Liu et al. employed DSPE-PEG2000 as nanocarriers for hydrophobic A1094 to formulated A1094@DSPE-PEG2000 nanoparticles, which showed excellent 1200-1300 nm NIR-II absorption (**Figure 1.6**).[61] Thus the deep brain tumor and inguinal lymph nodes were clearly detected at 1200nm after i.v. injection of A1094@DSPE-PEG2000, which had a lower background than NIR-I imaging. Additionally, the in-situ surgery of brain tumors was successfully conducted with the help of NIR-II optoacoustic imaging. However, the *in vivo* safety of such viral nanoparticles still remains to be thoroughly evaluated.
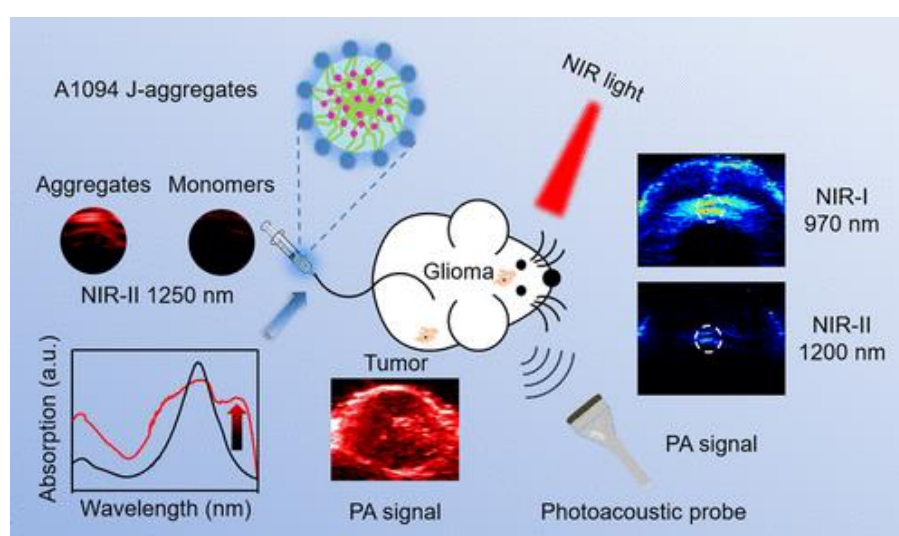
Figure 1.6. Schematic illustration of A1094@DSPE-PEG2000 with J-aggregation for enhanced NIR-II optoacoustic imaging of brain tumor. Reproduced with permission.[61] Copyright 2019, American Chemical Society.

1.5 Objectives and outline

The goal of this dissertation is to explore efficient optoacoustic contrast agents for precise diagnosis and phototherapy of various tumors. Croconaine dyes can overcome the challenges associated with various organic dyes such as complicated synthetic routines, poor photostability, low optoacoustic generation efficiency, low photothermal conversion efficiency, and biocompatibility. Croconaine dyes offer several advantages such as superior thermal stability, photobleaching resistance, solvatochromism, and spectral tenability shortcomings. However, most of the reported croconaine structures undergo H-aggregation during the nanoformulation process, which makes them unsuitable for cancer photo-theranostics in the NIR region. Therefore, it is necessary to develop stable formulations of crocoanine nanoparticles. This dissertation focuses on the development of a series of crocoanine nanoparticles with range of NIR absorption to assure deep opotoacoustic imaging and efficient PTT of various tumors.

This thesis is structured as follows. Chapter 1 introduces the principles of optoacoustic imaging, equipment, and corresponding contrast agents, then details the properties of croconaine dyes and their current biological applications. Chapter 2 focuses on the optoacoustic imaging and photothermal treatment of tumors using facile-synthesized CR760RGD-NPs. The synthesis of CR760 dye and its nano-modification and optoacoustic-photothermal characterization are discussed in detail, followed by *in vitro* and *in vivo* optoacoustic imaging and PTT. Chapter 3 focuses on the efficient optoacoustic imaging of brain tumors using CR780RGD-NPs, detailing its synthesis, characterization, *in vitro* and *in vivo* studies as well as its biocompatibility, thus highlighting the advantages of CR780RGD-NPs as optoacoustic contrast agents.

Chapter 4 focuses on the optoacoustic imaging and photothermal treatment of deep tissues using 880 nm-absorbed croconaine nanoparticles. In Chapter 5, we summarize the optical performance of developed croconaine-based nanoparticles for cancer theranostics, and discuss new ideas about future developments, optimization, and more biomedical application.

2 760nm-absorbed croconaine nanoparticles for optoacoustic imaging and photothermal therapy

Content in this chapter is based on (at parts verbatim) my published paper.

Author contributions: Nian Liu identified the CR760 dye, developed CR760RGD-NPs, carried nanoparticle characterization (DLS, zeta potential, photophysical properties, optoacoustic signals, photostability, photothermal performance) and cell experiments (MTT assay, AM/PI, cell uptake), whereas *in vivo* experiments (optoacoustic imaging, photothermal therapy, and biosafety) were assisted by Dr. Vipul Gujrati and technician Sarah Glasl. Dr. Patrick O'Connor synthesized and characterized the CR760 dye, carried out the conjugation of PEG and RGD with CR760 dye and finally carried out the DFT calculations. Dr. Vipul Gujrati along with Nian Liu designed the *in vitro* and *in vivo* experiments and analyzed the data. Dr. Dimitris Gorpas provided CW laser (780nm) setup for phototherapy. Sarah Glasl assisted with animal experiments and maintenance. Dr. Andreas Blutke, Prof. Axel Walch carried out TEM measurements and analysis. Dr. Karin Kleigrewe did the MALDI-TOF characterization. Prof. Oliver Plettenburg supervised dye synthesis, characterization, and provided intellectual input, and Prof. Michael Sattler and Prof. Vasilis Ntziachristos helped interpret the results, provided significant intellectual input, and supervised the research. All authors contributed to writing the paper.

2.1 Motivation

Theranostics agents that integrate real-time diagnosis with a therapeutic effect have the potential to accurately target diseased tissues and optimally exert therapy, representing a promising and cost-effective type of precision medicine.[62, 63] Among the reported theranostics agents, NIR absorbing agents are characterized by a simple but effective design: these agents only utilize light to generate optical or ultrasound signals for diagnosis while simultaneously liberating either heat or reactive oxygen species (ROS), resulting in tumor elimination.[64] A wide spectrum of biocompatible NIR absorbing organic dye-based agents have been recently explored for enhancing contrast in optoacoustic imaging and for photothermal therapy (PTT).[65, 66] Optoacoustic imaging can visualize tumor tissue at centimeter depths with high contrast and spatial resolution [7, 67], and PTT has the advantages of minimal invasiveness, spatiotemporal selectivity, and reduced side effects.[68]

Croconaine dyes have been suggested to overcome common limitations of other organic dyes considered for optoacoustic imaging and PTT.[46] In particular, croconaine dyes improve on the thermal stability, photobleaching resistance, solvatochromism, and spectral tenability shortcomings of most common organic dyes such as cyanine, squaraine, BODIPY, and tetrapyrrole dyes.[26, 69] Nevertheless, most of the proposed croconaine derivatives suffer from H-aggregation, modest chemical instability, and low solubility and are therefore not suitable for *in vivo* applications.[48] There is therefore a need for a croconaine dye with improved properties.

Some of these challenges, such as the structural stacking and dye aggregation of croconaine dyes, can be addressed by chemical modifications. Smith et.al. reported a stearic interaction between a pH-sensitive croconaine dye (Croc) and rotaxane, which prevented the aggregation of Croc.[58] The interlocked Croc-Rotaxane complex was loaded into liposomes and used for optoacoustic imaging applications.[58] However,

the synthesis of Croc and rotaxane consists of a multistep protocol. In another approach, Song et al. prevented dye aggregation via electronic effects by incorporating anionic carboxylates into croconaine-derived CR780,[51] which was followed by its modification with polyethylene glycol (PEG) and use in optoacoustic and phototherapy applications.[54] However, the synthesis and purification of CR780 also involve multistep protocols.

Here, we use the croconaine-based dye CR760 that, similarly to Croc and CR780, provides superior theranostic properties compared to most existing croconaine derivatives and, unlike any other croconaine derivative, can also be easily synthesized via a single-step protocol. We report for the first time the development of PEGylated CR760-based dye nanoparticles for theranostic (optoacoustic imaging and phototherapy) applications (**Scheme 2.1**). The croconaine-derived CR760 structure was previously reported for photovoltaic cell applications.[70] Importantly, we found that CR760 has no aggregation, blue shift, or chemical instability issues and is easy to chemically modify. Moreover, CR760 can be synthesized and purified in a single step. Therefore, we conjugated CR760 with NH_2-PEG2000-SH and c(RGDyC) peptide to generate self-assembling nanoparticles (CR760RGD-NPs) with tumor-targeting capability. CR760RGD-NPs exhibit a strong absorption peak at 760 nm (no quenching), high optoacoustic generation efficiency (OGE), high photothermal conversion efficiency (45.37%), and photostability as compared with various organic dyes or their derived nanoparticles, including the FDA-approved gold standard ICG. Modification with RGD increased the effect of CR760 on tumor-specific binding and accumulation. Additionally, CR760RGD-NPs displayed good biocompatibility and biosafety. In summary, we report CR760-derived nanoparticles as promising and highly efficient photo-theranostic agents for cancer diagnosis and therapy.
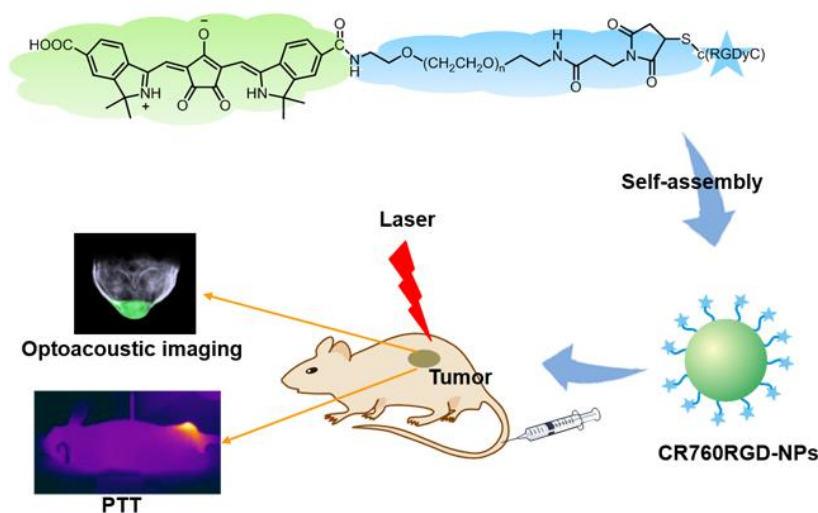
Scheme 2.1. Schematic of the CR760RGD-NPs synthesis and the application of optoacoustic imaging and photothermal therapy.

2.2 Experimental section

2.2.1 Materials

Croconic acid, 2,3,3-trimethyl-3H-indole-5-carboxylic acid, 2-ethoxyethanol, toluene, and 9,10-dimethylnathracene were bought from abcr GmbH (Germany). c(RADyC) and c(RGDyC) were obtained from GL biochem (Shanghai, China). NH_2-PEG2000-SH were obtained from Creative PEGWorks (Chapel Hill, USA). Indocyanine green (ICG) and 3-(4,5-dimethylthiazol-2-yl)-2,5-diphenyltetrazolium bromide (MTT) were purchased from Sigma-Aldrich (Germany). Calcein-acetoxymethyl (AM) and ethidium homodimer-1 (EthD1) were bought from Thermo Fisher Scientific. Other chemical reagents were obtained from abcr GmbH (Germany).

2.2.2 Synthesis of CR760, CR760-PEG-RAD, and CR760-PEG-RGD

Croconic acid, 142.1 mg (1 mmol), and 2,3,3-trimethyl-3H-indole-5-carboxylic

acid 385.8 mg (2 mmol) were dissolved in 1:1 anhydrous toluene/*n*-butanol (20 mL). Then the mixture was heated to reflux overnight and cooled to room temperature. The product was collected by filtration, washed with isopropanol, sonicated in EtOAc and the filtrate collected to give the title product as a black solid (394 mg, 81 %). ^{1}H NMR (400 MHz, DMSO-d_6) δ: 8.12 (s, 2H), 7.99 (d, J=8.1Hz, 2H), 7.65-7.55(m, 2H), 6.06(s, 2H), 1.54(s, 12H). MALDI: m/z = 513.175 [M + H]$^+$.
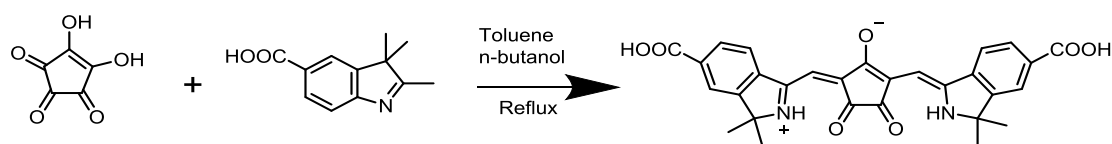
Scheme 2.2. Synthetic method of CR760
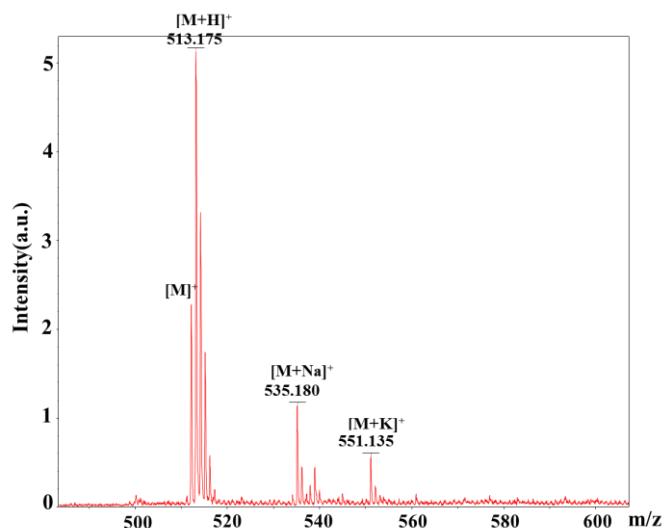
Figure 2.1. MALDI-TOF mass spectrum of CR760.

CR760-PEG-RAD was synthesized in two steps. CR760 (0.1 mmol), EDC•HCl (0.12 mmol), and NHS (0.12 mmol) were stirred in DMF (1 mL) at room temperature for 2 h, after which time NH$_2$-PEG2000-SH (0.1 mmol) was added, and the mixture was stirred for a further 24 h. The crude mixture was directly purified by C18 reversed-phase chromatography. Then c(RADyC) (0.1 mmol) was reacted with the above samples in PBS buffer (pH 6.0) for 2 h and purified with reverse-phase HPLC column. CR760-PEG-RGD were synthesized in a similar way.
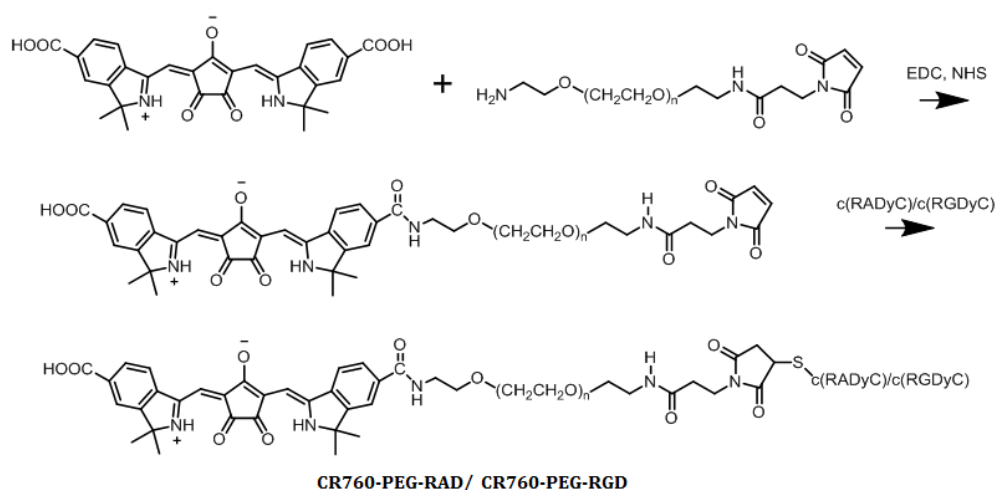
Scheme 2.3. Synthetic steps of CR760-PEG-RAD and CR760-PEG-RGD.

2.2.3 Preparation of CR760RAD-NPs and CR760RGD-NPs

CR760-PEG-RAD (1 mg) or CR760-PEG-RGD (1 mg) was dissolved in 1 mL deionized water and sonicated for 5 min, resulting in the nanometer-sized CR760RAD-NPs or CR760RGD-NPs.

2.2.4 Characterization

^{1}H NMR spectrum was measured on a Bruker spectrometer at 400 MHz. The m/z ratios of the compounds were recorded with a MALDI UltrafleXtreme (Bruker) using dihydroxybenzoic acid as the matrix. The molar absorption coefficient and quantum yield of CR760 were calculated as previously described.[71] CR760RGD-NPs were measured by ZEISS Libra 120 PLUS transmission electron microscopy (TEM) and dynamic light scattering (DLS) (Malvern Zetasizer). Absorption spectra were measured with a UV-1800 spectrometer (Shimadzu, Japan). Optoacoustic spectra of samples were carried out using an MSOT inVision 256-TF and the normalization was performed with India ink and Brilliant Black BN.[72] The optoacoustic generation efficiency (OGE) of samples was equal to the slope of the line where corrected optoacoustic intensities are plotted against absorbance.[72] The photostability of samples was

detected by an MSOT inVision 256-TF with pulsed laser irradiation for 30 min (fluence 10 mJ/cm^2).

2.2.5 Photothermal effect of CR760RGD-NPs

The photothermal performances of CR760RGD-NPs were assessed by measuring the temperature changes at different concentrations of CR760RGD-NPs upon exposure to a 780 nm CW laser at different laser power using an IR thermal camera. The photothermal conversion efficiency (PCE) of CR760RGD-NPs was calculated from the reference using the equation $\eta = [(hS(T-T_{surr})-Q_{Dis}]/I(1-10^{-A780})$.[73] Here the absorbance (A780) of CR760RGD-NPs was 0.65 at 780 nm and the power density (I) of 780 CW laser was 1 W/cm^2.

2.2.6 *In vitro* cell uptake

4T1 cells (2×10^5) were cultured in 6-well plate containing sterile cover slips, and then treated with CR760RAD-NPs or CR760RGD-NPs (20 μM) for 4 h. Cover slips were mounted on glass slides with mounting medium-DAPI (Invitrogen™). The prepared slides were imaged using Leica SP8 confocal microscope (Wetzlar, Germany).

2.2.7 *In vitro* PTT

4T1 cells were sub-cultured in a 96-well plate overnight (1×10^4 cells/well). Then the cells were first treated with PBS, CR760RAD-NPs (20 μM), and CR760RGD-NPs (20 μM) for 4 h, followed by laser irradiation (1 W/cm^2, 780nm CW laser) for 5 min. Subsequently, the cells were kept culturing for another 24 h to calculate the relative cell viability by standard MTT assay. Live/dead cell assays were identified with calcine-AM and EthD1. Briefly, 4T1 cells were sub-cultured in 96-well plates and divided based on the different treatments. After 24 h, the cells were co-stained with Calcein-AM and EthD1 for 30 min. Then the cells were rinsed with PBS and imaged with Leica

DMI3000 B Inverted Microscope (Wetzlar, Germany).

2.2.8 *In vivo* optoacoustic imaging

4T1 tumor models were prepared using nude mice (6 weeks) by implanting 4T1 cells (1×10^6) on the back of the mice. *In vivo* optoacoustic imaging and PTT studies were operated on when the tumor size reached ~100 mm^3. All procedures involving animal experiments were approved by the Animal Care and Handling Office of Helmholtz Zentrum München and the Government of Upper Bavaria.

4T1 tumor-bearing mice (n=5) per treatment were i.v. injected with CR760RAD-NPs or CR760RGD-NPs (1 mM). *In vivo* optoacoustic images were acquired at different time points before and after injection (0, 1, 4, 8, 24 h) using an MSOT inVision 256-TF. The averaged optoacoustic signals of tumor regions were extracted using ViewMSOT 4.0 software (iThera Medical, Munich).

2.2.9 *In vivo* PTT

The tumor-bearing mice were randomly divided into five groups (n=5) and subjected to different treatments as follows: (i) i.v. injection of 100 μL PBS, (ii) i.v. injection of 100 μL PBS + laser irradiation, (iii) i.v. injection of 100 μL CR760RAD-NPs (1 mM) + laser irradiation, (iv) i.v. injection of 100 μL CR760RGD-NPs (1 mM) + laser irradiation (iii) i.t. injection of 20 μL CR760RGD-NPs (1 mM) + laser irradiation. The thermal images and temperature changes of tumor regions for each group were recorded using an infrared thermal camera. The tumor volume and body weight were measured every day for 8 days, then the mice were sacrificed and the tumors from each group were resected for hematoxylin-eosin (H&E) staining.

2.2.10 Blood hematology and biochemistry analyses

C57BL/6 mice were randomly separated into 4 groups (n=5). The control group

was i.v. injected with 100 μL of PBS and blood was collected on day 14. The other 2 groups were i.v. injected with 100 μL of CR760RGD-NPs (1 mM) and blood was collected on days 7, and 14. Then hematology and blood biochemistry tests were carried out to analyze the detailed parameters of blood samples using the Hitachi 917 Clinical Chemistry Analyzer (Roche, Germany). The major organs were removed for H&E staining.

2.3 Results

2.3.1 Synthesis and characterization of CR760

CR760 was synthesized in a one-step condensation reaction of croconic acid and 2, 3,3-Trimethyl-3H-indole-5-carboxylic acid, with yields of 81% (**Scheme 2.2**). The chemical structure of CR760 was confirmed by ^{1}H NMR spectroscopy and MALDI-TOF mass spectrometry (**Figure 2.1**). CR760 has moderate solubility in common organic solvents such as chloroform, dichloromethane, and ethanol (**Figure 2.2**). **Table 2.1** shows the experimental comparison of photophysical properties of CR760 with the gold industry standard FDA-approved ICG. Comparative data shows that CR760 has a strong absorption peak at 760 nm and exhibits a significantly higher molar absorption coefficient and 1/16 of the quantum yield observed for ICG in ethanol. Furthermore, the OGE of CR760 and ICG were measured in 10% FBS. The OGE value reflects the ability of a compound to convert optically absorbed energy into pressure waves, which in turn provides information regarding optoacoustic intensity. CR760 exhibits an excellent OGE which is 1.75 times higher than that of ICG.
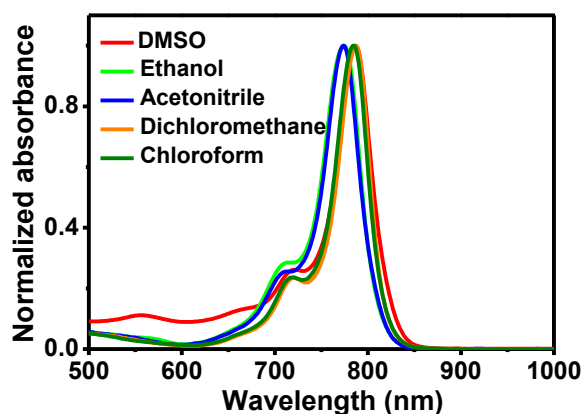
Figure 2.2. Normalized optical spectra of CR760 in different organic solvents.

Table 2.1 Photophysical properties of ICG and CR760.

Dye	Fluorescence Ex/Em (nm)	Molar absorption coefficient ($M^{-1}\,cm^{-1}$) in ethanol	Quantum yield in ethanol	Optoacoustic generation efficiency in 10% FBS
ICG	780/810	$2.1 \cdot 10^5$ at 780 nm	0.05 at 810 nm	0.6855
CR760	760/790	$3.25 \cdot 10^5$ at 780 nm	0.003 at 790 nm	1.20

2.3.2 Synthesis and characterization of CR760RGD-NPs

Self-assembled nanoparticles were prepared by mono-amide conjugation of the bis-carboxylic acid CR760 with NH_2-PEG2000-SH followed by Michael addition of the free thiol to the tumor-targeting c(RGDyC) peptide (**Figure 2.3a**). Although the bis-amide was easier to synthesize, this led to an inferior dye that was blue-shifted by 53 nm relative to the monoamide. Density functional theory (DFT) calculations were used to rationalize the beneficial effect of anionic substituents on the chromophore (**Figure 2.4**). Excitation energies were predictably overestimated,[74] however the calculations did corroborate our experimental finding of a blue-shifting of the neutral bis-amide relative to the anionic monoamide, likely due to a lesser degree of charge transfer in

the singlet excitation state of the bis-amide. A negative control group consisting of CR760RAD-NPs was also synthesized in a similar fashion utilizing a c(RADyC) peptide, which has a molecular weight comparable to the c(RGDyC) peptide but no active targeting ability towards integrin $\alpha_v\beta_3$. **Scheme 2.3** shows the CR760-PEG-RAD and CR760-PEG-RGD synthesis steps, with the corresponding MALDI-TOF analyses indicating the purity of the compounds (**Figure 2.5**). **Figure 2.3b** shows the self-assembled CR760RGD-NPs as a clear olive-green, homogeneous aqueous solution. The shape and size of the nanoparticles were evaluated by TEM and DLS. **Figure 2.3b, c** show that the CR760RGD-NPs were nano-sized aggregates with an average diameter of approximately 23 nm. The CR760RAD-NPs control groups showed a similar size distribution (**Figure 2.6**). **Figure 2.3d, e** show the optical and optoacoustic spectra of CR760RGD-NPs. A narrow and intense peak at 760 nm was similar to data obtained for CR760RAD-NPs (**Figure 2.7**). The zeta potential of CR760RAD-NPs and CR760RGD-NPs is -15.8 mV and -16.3 mV, respectively. Next, **Figure 2.3f** demonstrates that the OGE of CR760RGD-NPs is 1.75 times higher than that of ICG, indicating that CR760RGD-NPs can function as an efficient optoacoustic imaging agent. Furthermore, the photostability of CR760RGD-NPs was evaluated by irradiating the samples continuously with a pulsed laser (fluence 10 mJ/cm^2) for 30 min and benchmarking against ICG. **Figure 2.3g** shows that both CR760-derived nanoparticles are photostable in comparison to ICG, which under the same conditions was photo-bleached by up to 94 %. Next, ROS generation of CR760RGD-NPs was assessed by 9,10-dimethylnathracene (DMA).[75] **Figure 2.8** shows no decrease of DMA fluorescence intensity in CR760RGD-NP samples after laser irradiation, indicating no $^1O_2$ generation and no photodynamic effect. These results of characterization studies clearly indicate that the CR760RGD-NPs self-assemble into ultrasmall nanoparticles which exhibit a high OGE and high photostability, and as such are suitable for *in vivo* optoacoustic imaging and PTT.
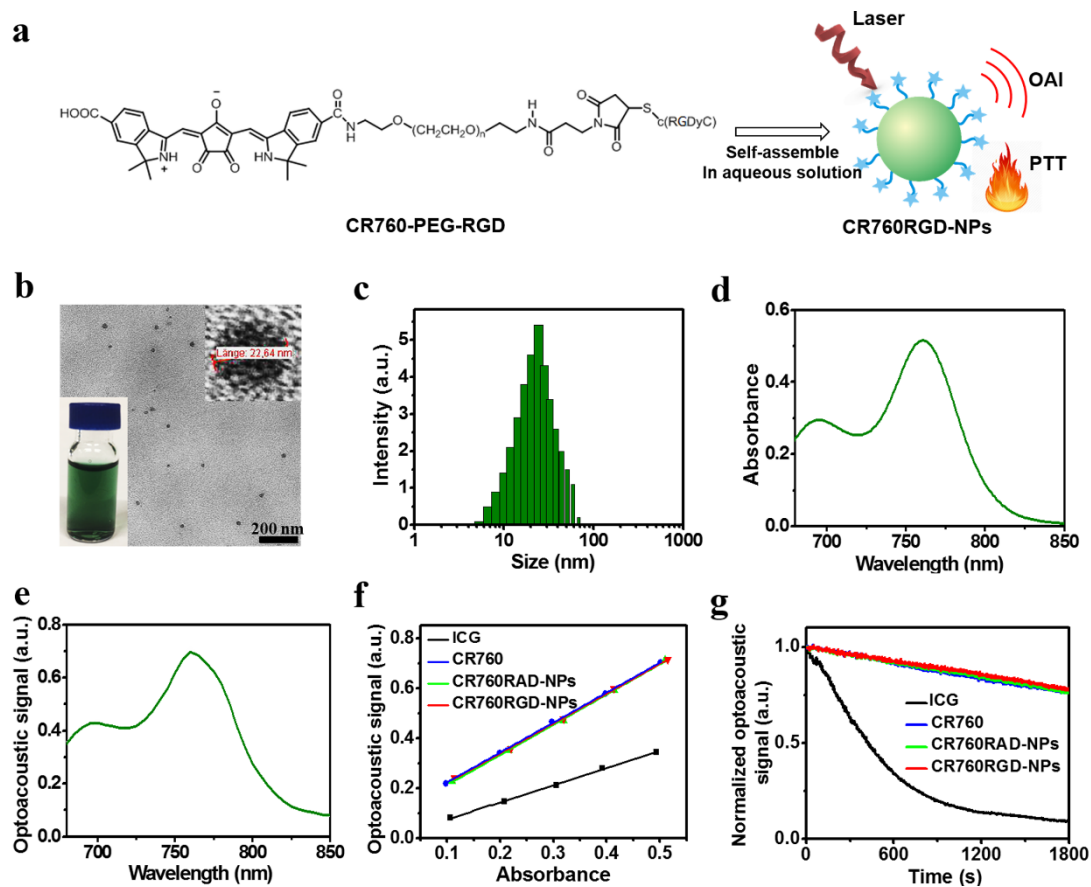
Figure 2.3. Synthesis and characterization of CR760RGD-NPs. (a) Schematic illustration of the preparation of CR760RGD-NPs for optoacoustic imaging and PTT. **(b, c)** TEM image and DLS profile of CR760RGD-NPs. **(d, e)** Optical spectrum and optoacoustic spectrum of CR760RGD-NPs. **(f)** Optoacoustic signal intensity of ICG, CR760, CR760RAD-NPs, and CR760RGD-NPs at different concentrations. **(g)** Optoacoustic signal degradation of ICG, CR760, CR760RAD-NPs, and CR760RGD-NPs after pulsed laser irradiation (fluence 10 mJ/cm^2, 30 min).
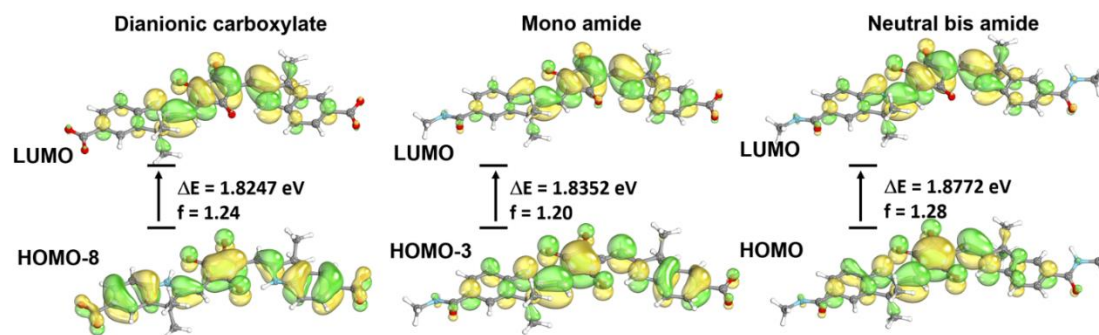
Figure 2.4. Molecular orbitals corresponding to major singlet π->π* excitations, energy levels, and corresponding oscillator strengths (f) for CR760 with neutral bis-amide, monoanion and dianion, gas phase calculations using Gaussian 16 Rev B.01. Geometry optimizations and frequencies at the B3LYP/6-31G(d,p) level. UV absorption using TD-DFT at the B3LYP/cc-pVTZ level. Molecular orbitals appear to show a greater degree of charge transfer for ionized carboxylates relative to their neutral protonated congeners.
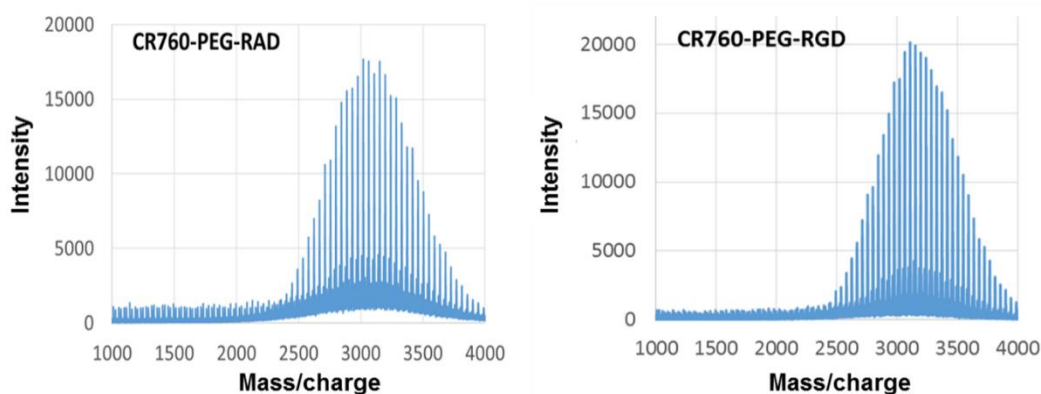
Figure 2.5. MALDI-TOF analyses of CR760-PEG-RAD and CR760-PEG-RGD.
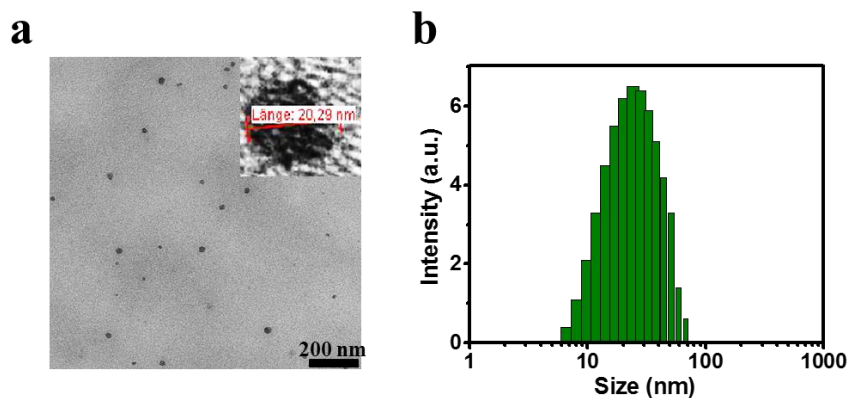
Figure 2.6. TEM image (**a**) and DLS profile (**b**) of CR760RAD-NPs.
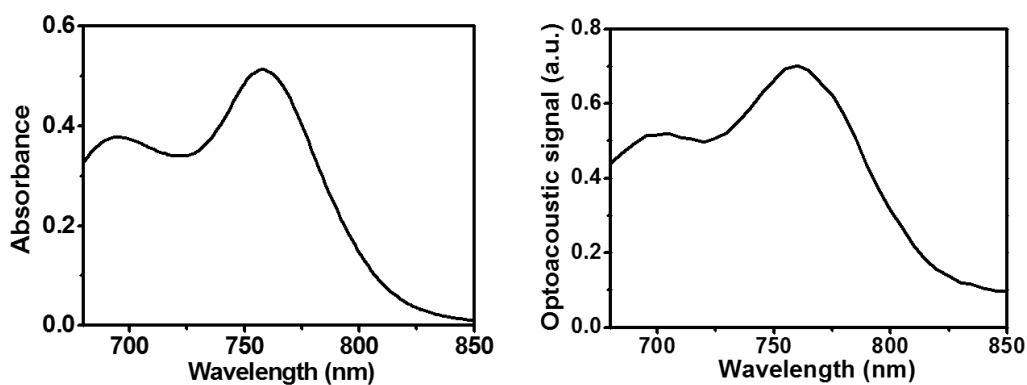
Figure 2.7. Optical spectrum and optoacoustic spectrum of CR760RAD-NPs.
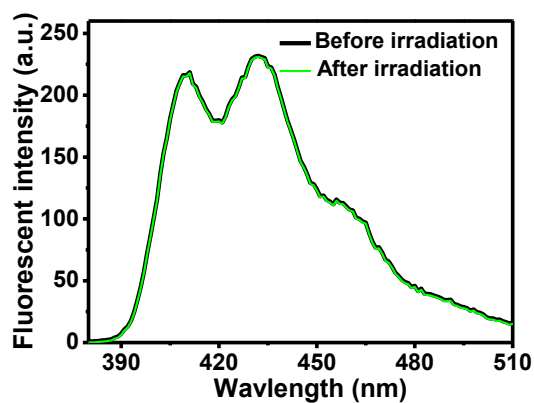
Figure 2.8. Fluorescent spectra of 9,10-dimethylnathracene (DMA) incubated with CR760RGD-NPs before and after laser irradiation. The fluorescent intensity shows no decrease after the treatment, which signifies no $^1O_2$ generation.

2.3.3 *In vitro* photothermal performance of CR760RGD-NPs

To assess the PTT potential of CR760RGD-NPs, increasing concentrations of CR760RGD-NPs at 0, 5, 10, 20, or 30 μM were exposed to a 780 nm CW laser at a power density of 1.0 W/cm^2. **Figure 2.9a** shows a concentration-dependent heating effect. Irradiation of a 30 μM solution of CR760RGD-NP generated a 39.9 ℃ change, which compared favorably to the 12.0 ℃ change observed for the water control. Preclinical studies of photothermal therapeutics show that heating cancer cells to 42–50 ℃ for more than 5 min can be cytotoxic.[65] The effect of laser power intensity (0.3, 0.5, 0.8, or 1.0 W/cm^2) on the temperature change of CR760RGD-NPs (30 μM) was explored next. **Figure 2.9b** shows a clear laser power intensity dependence on the temperature increase. The PCE of CR760RGD-NPs was calculated using CR760RGD-NPs irradiated with 780 nm CW laser for 10 min and cooled to room temperature. The temperature changes were recorded using the IR thermal camera and PCE was calculated to be 45.37% (Figure 2c).

To confirm if the targeting c(RGDyC) peptide is exposed on the surface of the nanoparticles, we carried out a cell uptake assay by confocal imaging *in vitro*. To monitor the difference in cell targeting ability, we compared differences in the uptake of targeted nanoparticles (CR760RGD-NPs) with non-targeted nanoparticles (CR760RGD-NPs) after a 4 h incubation in 4T1 cells. Significant differences in cell uptake efficiency were observed between the two groups, with an enhanced cell uptake of CR760RGD-NPs observed due to the active targeting ability (**Figure 2.10**). To further evaluate the PTT potential of CR760RGD-NPs, photo-cytotoxicity of CR760RGD-NPs on 4T1 cells after a 4 h incubation was evaluated using a standard MTT assay. **Figure 2.9d** shows that both CR760RAD-NPs and CR760RGD-NPs show negligible cytotoxicity at a concentration of up to 20 μM. However, upon 5 min of irradiation with a 780 nm CW laser at 1.0 W/cm^2, the viability of cells treated with CR760RGD-NPs was only 9.5%, while the viability of cells treated with CR760RAD-

NPs was 41.2%. These results point to the enhanced tumor targeting and accumulation of CR760RGD-NPs vs CR760RAD-NP control. To visualize the PTT effect of CR760RGD-NPs, the viability of 4T1 cells was determined by live/dead cells assays. 4T1 cells incubated with PBS, CR760RAD-NPs, and CR760RGD-NPs before and after laser irradiation were co-stained with calcein-AM and EthD-1. The difference in cellular cytotoxicity when incubated with the control groups and CR760RGD-NP is clearly evident, with the latter displaying the most pronounced cytotoxic effect (**Figure 2.9e**).
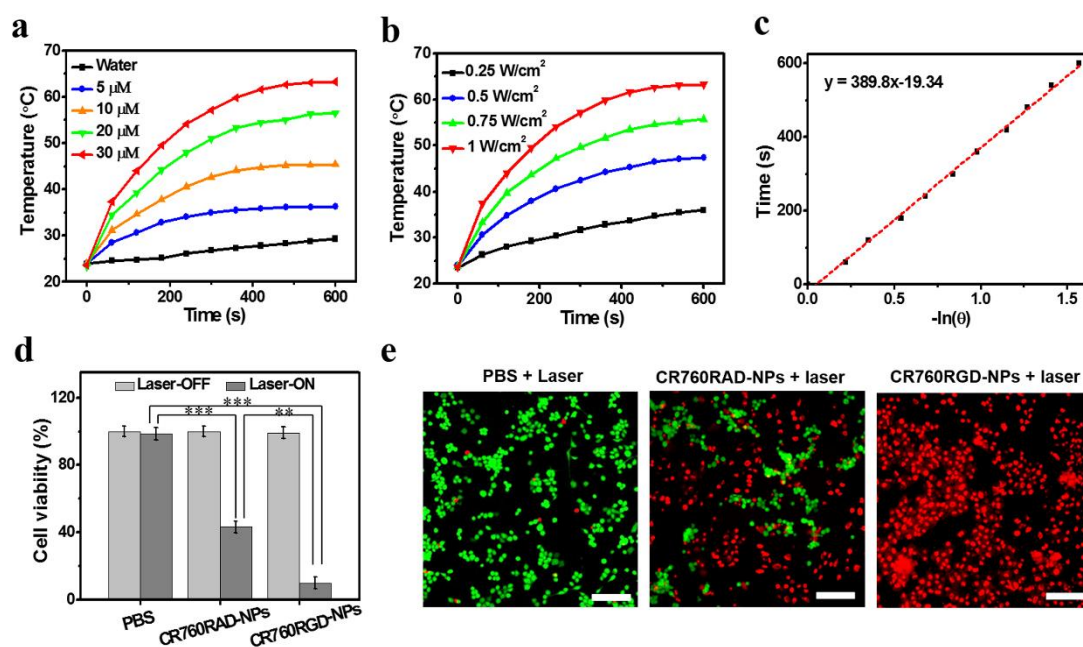
Figure 2.9. **(a)** Temperature change curves of CR760RGD-NPs at different concentrations upon exposure to a 780 nm CW laser (1 W/cm^2). **(b)** Temperature change curves of CR760RGD-NPs (30 μM) upon exposure to a 780 nm CW laser at different power densities. **(c)** Linear correlation of the cooling times of CR760RGD-NPs versus negative logarithm of temperatures.. **(d)** Relative viabilities of 4T1 cells after treatment with PBS, CR760RAD-NPs (20 μM) and CR760RGD-NPs (20 μM) with (or without) laser irradiation (1 W/cm^2, 5 min). **(e)** Fluorescence images of live/dead staining of 4T1 cells after different treatments. Green color, live cells; red color, dead cells. Scale bars, 100 μm. (*P < 0.05, ***P < 0.001)
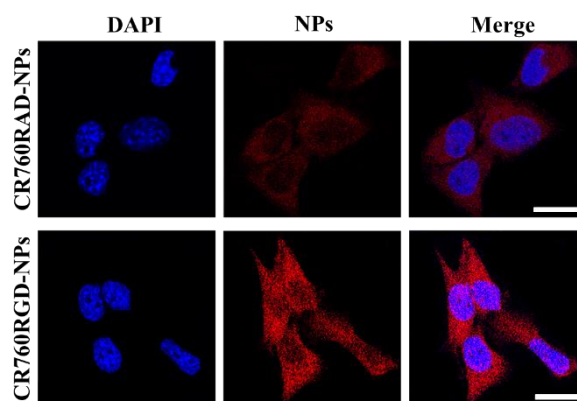
Figure 2.10. Cell uptake assay. Confocal microscope images of 4T1 cells treated with CR760RAD-NPs or CR760RGD-NPs for 4h. (Scale bar, 25 μm)

2.3.4 *In vivo* optoacoustic imaging with CR760RGD-NPs

Based on the excellent optoacoustic properties on phantoms described above, CR760RGD-NPs were next studied in 4T1 tumor models. Five 4T1 tumor-bearing mice per treatment were i.v. injected with control CR760RAD-NPs or CR760RGD-NPs. **Figure 2.11a** shows representative unmixed multispectral optoacoustic tomography (MSOT) images of 4T1 tumor-bearing mice, acquired at different time points post-injection (0h, 1h, 4h, 8h, and 24h). The green signals represent the unmixed CR760 signal. As observed from the signal strength in the tumor regions, both CR760RAD-NPs and CR760RGD-NPs could effectively reach the tumor at the early time points (1 and 4 h), presumably due to the enhanced permeability and retention (EPR) effect. However, because of their active tumor-targeting, CR760RGD-NPs remained in the tumor regions longer. At 24h, the optoacoustic signal from the tumors treated with CR760RAD-NPs was very weak compared to the tumors treated with CR760RGD-NPs due to systemic clearance from the tumor vasculature (**Figure 2.11b**). To validate the results of the *in vivo* MSOT images, tumors were isolated from all animals 24 h after MSOT scanning. Fluorescence images of tumors sectioning from the two groups were acquired with a 750 nm excitation. **Figure 2.11c** shows a strong fluorescence signal from the CR760RGD-NPs treated group but very weak

fluorescence from the CR760RAD-NPs treated group. H&E staining confirmed the presence of tumors. To analyze the biodistribution of both types of nanoparticles, the vital organs (liver, kidney, heart, spleen) were also isolated 24 h after treatment and the optoacoustic measurements were performed using MSOT. The optoacoustic coronal plane images and corresponding optoacoustic signal intensities of different organs are shown in **Figure 2.12**. The two types of nanoparticles showed a similar level of uptake in the liver and a slightly lower uptake in the kidney, spleen, and heart.
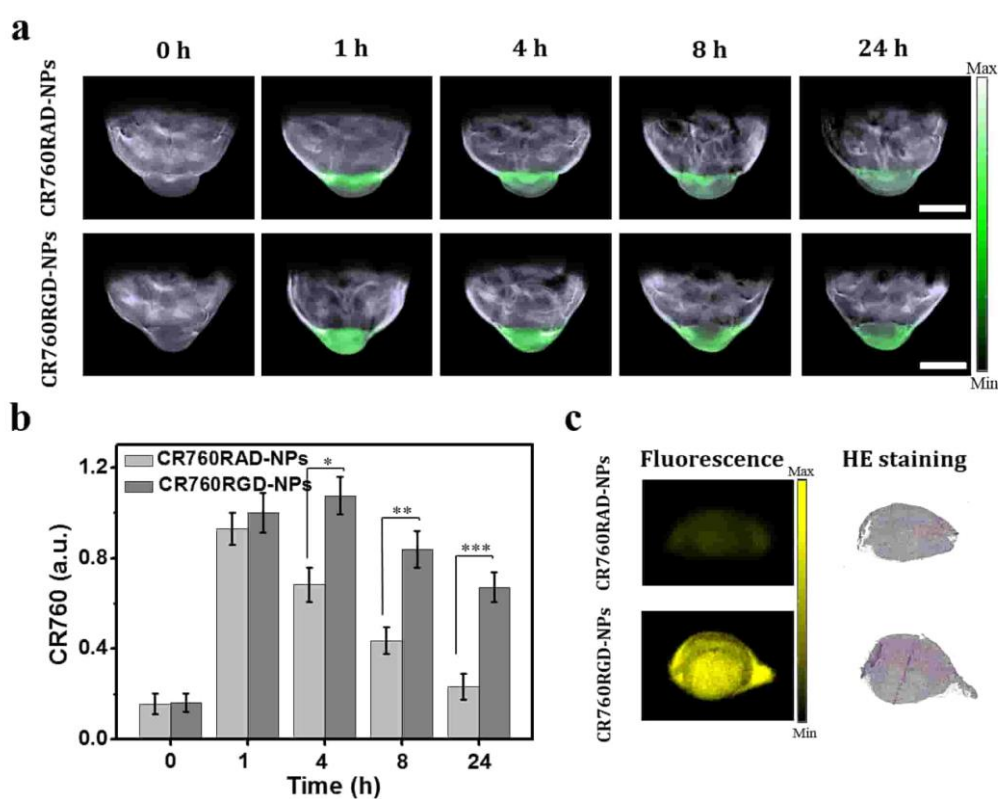
Figure 2.11. *In vivo* MSOT imaging of CR760RAD-NPs and CR760RGD-NPs. **(a)** Representative unmixed MSOT images of 4T1 subcutaneous tumor models i.v. injected with 100 μL of CR760RAD-NPs or CR760RGD-NPs (1 mM), scale bar = 5mm, (n=5). Unmixed CR760 signal is shown by the green color in the tumor region. **(b)** Quantification of panel (a): CR760RAD-NPs and CR760RGD-NPs concentrations in the tumor region measured over time **(c)** Fluorescence images and HE staining of tumor slices which were treated with CR760RAD-NPs and CR760RGD-NPs. (*P < 0.05,

***P < 0.001)
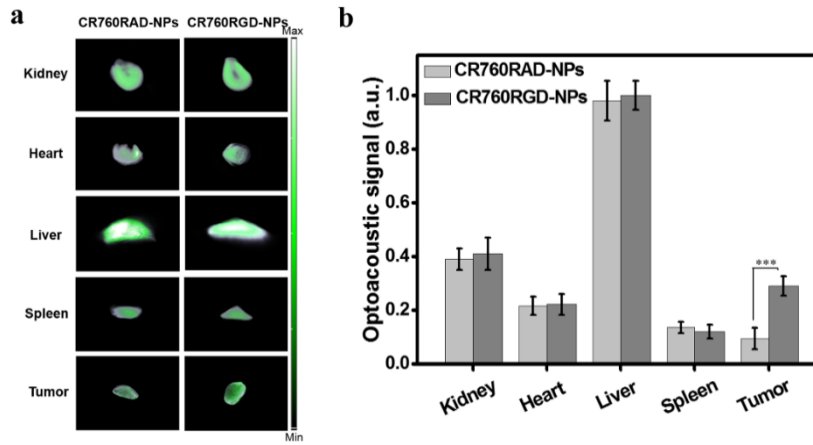
Figure 2.12. The biodistribution of CR760RAD-NPs and CR760RGD-NPs in vital organs at 24 h post-injection. (a) Optoacoustic coronal plane images of major organs. (b) Optoacoustic signal intensities of major organs. (***P < 0.001)

2.3.5 *In vivo* PTT efficacy of CR760RGD-NPs

4T1 tumor-bearing mice were randomized into five groups that received one of the following treatments: (i) i.v. injection of 100 μL PBS, (ii) i.v. injection of 100 μL PBS + laser irradiation, (iii) i.v. injection of 100 μL CR760RAD-NPs (1 mM) + laser irradiation, (iv) i.v. injection of 100 μL CR760RGD-NPs (1 mM) + laser irradiation (v) intratumoral injection of 20 μL CR760RGD-NPs (1 mM) + laser irradiation. An irradiation time of 4 h post-injection was identified as being optimal for optoacoustic imaging. A thermal imaging camera recorded the temperature change of tumor regions from the treated groups until 10 min. As can be seen in **Figure 2.13a, b**, the tumor temperature in the laser-irradiated area treated intratumorally with CR760RGD-NPs reached as high as 59 ℃. Additionally, the temperature of the tumor region i.v. injected with CR760RGDs reached 55 ℃, while the control groups treated with CR760RAD-NPs or PBS reached 46.2 ℃ and 39.2 ℃, respectively. We compared i.v. injected groups with i.t. injected group in which a known concentration of NPs was present in the tumor. This comparison was performed to mainly study the difference of PTT

efficacy upon i.v. injection of targeted CR760RGD-NPs against i.t. injected CR760RGD-NPs. No significant difference in therapeutic efficacy between the i.v. injected and i.t. injected CR760RGD-NPs was observed and indicated that targeted CR760RGD-NPs at selected doses exhibit an effective PTT response independent of the administration mode.

During the subsequent 8-day observation period, the tumor volumes and body weights of the five groups were measured daily. Group (v) with intratumoral injection of CR760RGD-NPs displayed complete tumor elimination. Groups (iii) and (iv) showed significant inhibition of tumor growth, and due to the active tumor-targeting of CR760RGD-NPs, group (iv) exhibited almost completely tumor elimination. In contrast, the tumors from the other two control groups showed consistently high growth rates, suggesting that the PTT induced by CR760RGD-NPs can significantly eliminate cancer cells (**Figure 2.13c, d**). **Figure 2.13e** indicates that no abnormalities in animal body weights were observed. After 8 days, the tumors from each group were isolated and stained with H&E. The tumor slices from CR760RGD-NPs (i.v., i.t.) + laser treated mice exhibited condensed nuclei and shallow staining color, which indicates cell apoptosis or necrosis (**Figure 2.13f**). Collectively, these results suggested that CR760RGD-NPs can be an efficient PTT agent for cancer treatment.
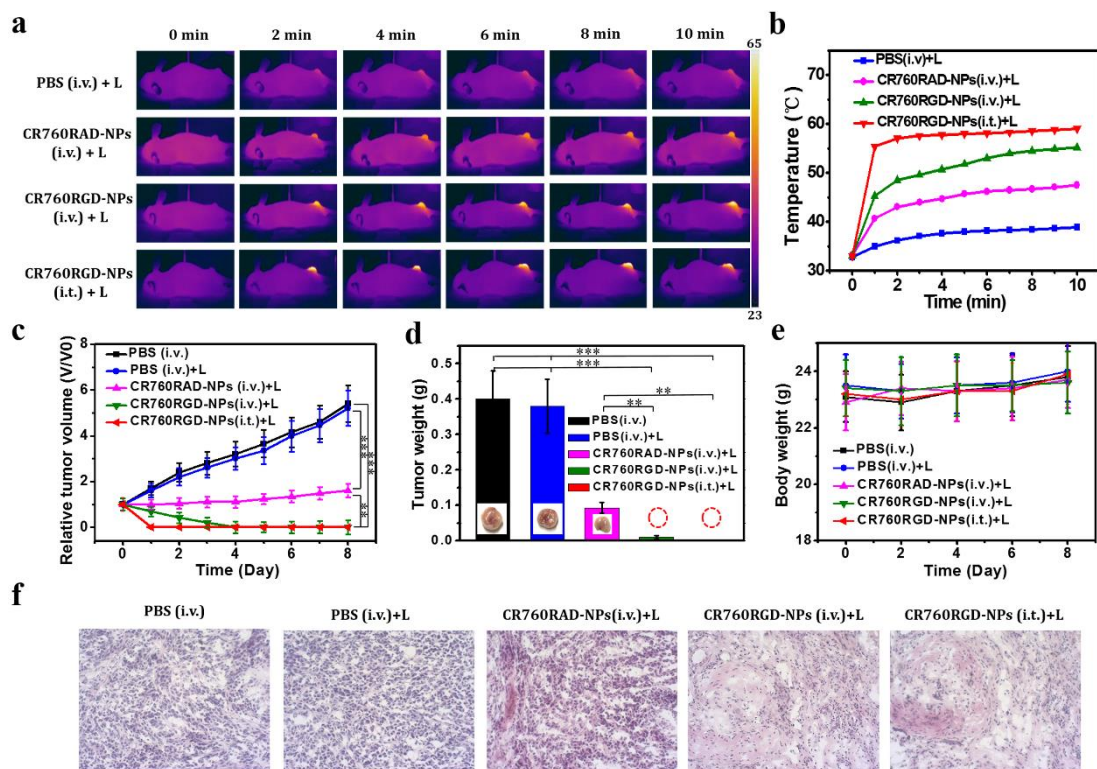
Figure 2.13. (a) Thermal images of 4T1 tumor-bearing mice with different treatments exposed to a 780 nm laser (1 W/cm^2) recorded at different time intervals, respectively. **(b)** Temperature changes of tumors in different treated groups during laser irradiation as indicated in **(a)**. **(c-e)** Relative tumor volumes, tumor weight, and body weight of mice treated with PBS, PBS(i.v.)+laser, CR760RAD-NPs(i.v.)+laser, CR760RGD-NPs(i.v.)+laser, and CR760RGD-NPs(i.t.) +laser. **(f)** H&E staining of tumors isolated from mice at day 8 after various treatment. i.v. = intravenous, i.t. = intratumoral. (*P < 0.05, ***P < 0.001)

2.3.6 *In vivo* biosafety of CR760RGD-NPs

Healthy C57BL/6 mice were injected with 100 μL of CR760RGD-NPs (1 mM) and blood samples were collected on day 1, 7 and 14 post-injection for organ function examination (**Figure 2.14a,b**). The blood chemistry parameters and hematology analysis results showed no noticeable difference between CR760RGD-NPs treated mice and the PBS-treated control mice. The H&E staining and histology analysis of

vital organs (**Figure 2.14c**) further confirmed no evident cytotoxicity or damage to the organs in the treated group. These results provide no evidence of acute toxicity and suggest that CR760RGD-NP's may be well tolerated and suitable for *in-vivo* imaging and phototherapy.
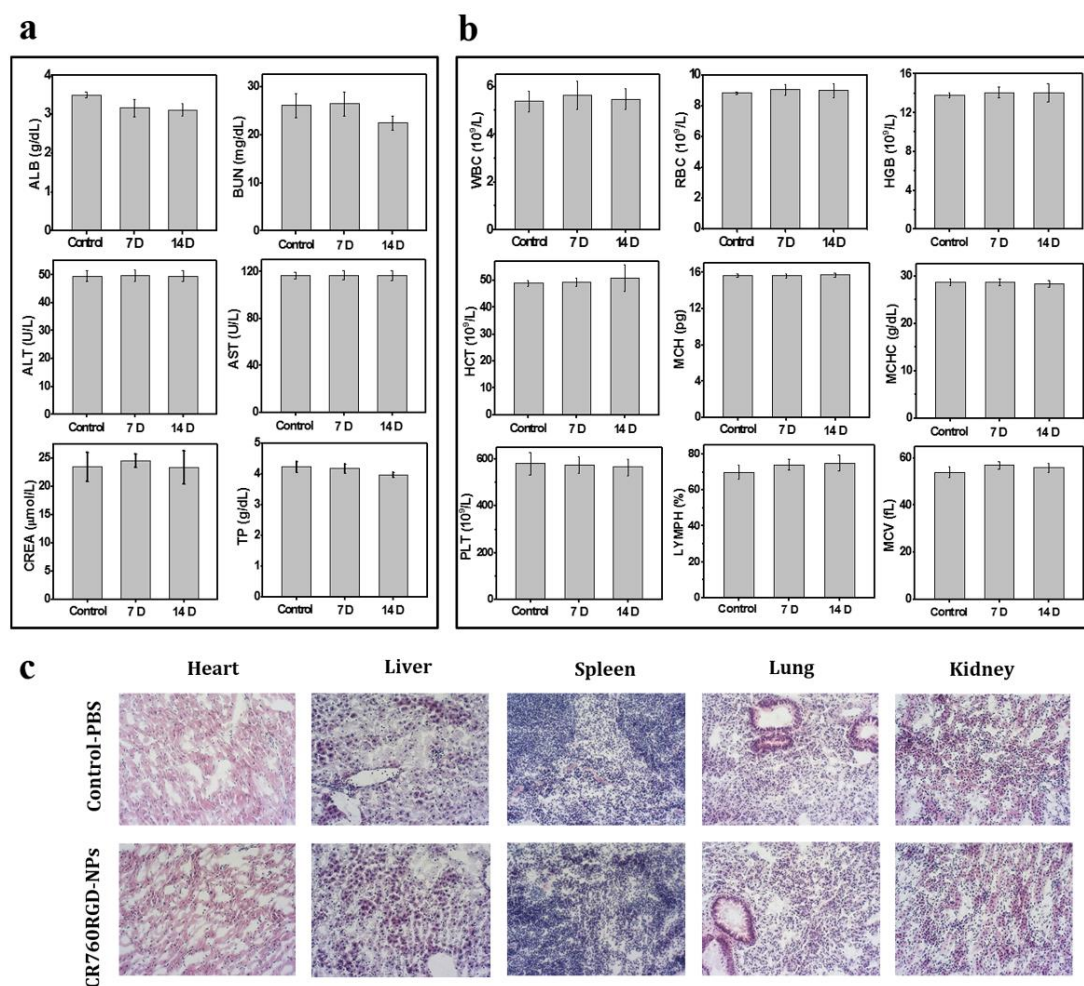
Figure 2.14. (a,b) Blood biochemistry and hematology data of healthy C57BL/6 mice after i.v. injection of CR760RGD-NPs (1mM) or PBS (control). ALB, albumin; BUN, blood urea nitrogen; ALT, alanine transferase; AST, aspartate transferase; CREA, creatinine; TP, total protein; WBC, white blood cells; RBC, red blood cells; HGB, hemoglobin; HCT, hematocrit; MCH, mean corpuscular hemoglobin; MCHC, mean corpuscular hemoglobin concentration; PLT, platelet; LYMPH, lymphocytes; MCV, mean corpuscular volume. **(c)** H&E staining of vital organs of mice treated after 14

days ($20\times$ magnification).

2.4 Discussion

Here we describe the generation of CR760-derived nanoparticles which we demonstrate as highly efficient optoacoustic and PTT agents for theranostics studies. CR760 can be synthesized in a single step with high purity, and was mono-conjugated to a PEG linker to enable self-assembling nanoparticles. The CR760 dye and self-assembled CR760RGD-NPs exhibited high OGE, high PCE, and good photostability when compared to the FDA-approved gold standard ICG. Based on the EPR effect and $\alpha_v\beta_3$ targeting, CR760RGD-NPs could effectively accumulate in the tumor tissue and exhibited strong optoacoustic signals. Furthermore, the strong photothermal performance of CR760RGD-NPs not only ensured high-efficiency cell-ablating capability, but also drove complete tumor elimination in mice, highlighting its superior phototherapeutic performance. Moreover, systemically administered CR760RGD-NPs showed no signs of systemic and organ-specific toxicity.

While many organic dyes possess limited solubility, hindering their biomedical applicability, these limitations can be addressed by nanoformulations. We have previously developed PEGylated liposomes incorporating ICG, which displayed efficient tumor accumulation as visualized by the MSOT system.[30] Furthermore, we employed a flash nanoprecipitaion method to encapsulate the iBu-TSBSH5 dye into QH2 nanoparticles.[76] Intrinsically self-assembled nanoparticles have recently attracted much attention because of their ability to achieve a robust nanostructure with high dye conjugation.[76] An expedient self-assembly nanoagent involves covalent linkage to PEG, an FDA-approved hydrophilic polymer, such as PEGylated cypate-derived nanoparticles[77], PEGylated IR780 nanoparticles[78], and PEGylated porphyrin nanoparticles[37]. In the current study, based on the hydrophilic linker and

hydrophobic dye interactions, we obtained self-assembling CR760RGD-NPs by covalent conjugation of the CR760 dye with NH_2-PEG_{2000}-SH and c(RGDyC). The ultra-small size distribution (around 23 nm) allows these NPs to accumulate at the tumor site via the EPR effect. Further modification with the RGD peptide assures active cancer-targeting and enhanced retention, suitable for longitudinal imaging.

Agents exhibiting a high absorption cross-section can enhance the contrast in visualizing and quantifying diverse biological processes and diseases by optoacoustic imaging.[7] In general, an ideal optoacoustic contrast agent should have the photophysical characteristics of a narrow NIR absorption peak, high molar extinction coefficient, low quantum yield, high OGE, good photostability, tumor specificity, and biocompatibility.[16] OGE values represent the ability of the compound to convert optically absorbed energy into pressure waves that give a strong optoacoustic signal. CR760RGD-NPs exhibit a superior OGE compared to other commercially available dyes.[31] The strong photostability of CR760RGD-NPs ensures continuous and accurate signal detection. Based on these promising optoacoustic properties and active tumor-targeting, CR760RGD-NPs efficiently accumulate in the tumor region and can be detected by MSOT with high sensitivity.

The 45.37% photothermal conversion efficiency of CR760RGD-NPs is greater than most reported PTT agents.[69, 79, 80] Moreover, CR760RGD-NPs generate a very low fluorescence signal, which quenches the radiative decay of fluorescence and enhances the nonradiative energy in the form of heat. Additionally, CR760RGD-NPs do not generate singlet oxygen to triplet state intersystem crossing, which indicates lack of a photodynamic effect under laser irradiation. Therefore, CR760RGD-NPs can serve as efficient PTT agents for tumor targeting and elimination.

In summary, CR760-derived nanoparticles were developed for efficient optoacoustic imaging and PTT of tumors. The self-assembled CR760RGD-NPs displayed efficient tumor targeting, while the high OGE and photostability ensured

strong optoacoustic contrast. The promising photothermal performance enables phototherapeutic efficacy *in vitro* and *in vivo*, while the absence of cytotoxic effects in major organs indicates the possibility for clinical translation. Therefore, CR760RGD-NPs provide a valuable approach to construct smart theranostic platforms for future clinical applications.

3 780nm-absorbed croconaine nanoparticles enable efficient optoacoustic imaging of murine brain tumors

Content in this chapter is based on (at parts verbatim) my published paper.

Nian Liu, Vipul Gujrati*, Jaber Malekzadeh-Najafabadi, Juan Pablo Fuenzalida Werner, Uwe Klemm, Longguang Tang, Zhenyue Chen, Jaya Prakash, Yuanhui Huang, Andre Stiel, Gabriele Mettenleiter, Michaela Aichler, Andreas Blutke, Axel Walch, Karin Kleigrewe, Daniel Razansky, Michael Sattler, Vasilis Ntziachristos*. Croconaine-based nanoparticles enable efficient optoacoustic imaging of murine brain tumors. *Photoacoustics* 2021, 100263.

Author contributions: Nian Liu identified the CR780 dye, developed CR780RGD-NPs, carried nanoparticle characterization (DLS, Zeta potential, photophysical properties, optoacoustic signals, photostability) and cell experiments (MTT assay, cell uptake, *in vitro* BBB penetration), whereas *in vivo* experiments (optoacoustic imaging, and biosafety) were assisted by Dr. Vipul Gujrati and technician Uwe Klemm. Dr. Vipul Gujrati along with Nian Liu designed the *in vitro* and *in vivo* experiments and analyzed the data. Jaber Malekzadeh-Najafabadi helped for optoacoustic phantoms experiments. Dr. Juan Pablo Fuenzalida Werner and Yuanhui Huang helped for the measurement and analysis of optoacoustic generation efficiency. Uwe Klemm assisted with animal experiment and animal maintenance. Dr. Longguang Tang synthesized CR780 dye and conjugation of PEG and RGD with CR780 dye. Gabriele Mettenleiter, Dr. Michaela Aichler, Dr. Andreas Blutke, Prof. Axel Walch carried out TEM measurements and analysis. Dr. Zhenyue Chen and Prof. Daniel Razansky provided intellectual input. Dr. Karin Kleigrewe did the MALDI-TOF characterization. Prof. Michael Sattler and Prof. Vasilis Ntziachristos helped interpret the results, provided significant intellectual input, and supervised the research. All authors contributed to writing the paper.

3.1 Motivation

Optoacoustic imaging is a versatile imaging tool that is highly applicable in preclinical research, it offers the ability to visualize organs or tissues with high contrast and high spatial resolution, and quantify sub-organ structures at a depth of centimeters.[3, 67] Besides, a variety of molecules, including endogenous hemoglobin, melanin, lipids, collagen, and exogenously delivered synthetic contrast agents, can boost strong optoacoustic signals to aid in the precise diagnosis of disease.[7] Benefiting from these superior advantages, optoacoustic imaging has been used for many biological applications, such as cancer, neuroimaging, and cardiovascular disease.

Brain tumors usually occur when abnormal cells form within the brain.[81] As the skull and endogenous hemoglobin in the blood can dramatically reduce the laser flux, thus it is a little difficult to catch the tumor site in the deep region by optoacoustic imaging without endogenous contrast agents.[82, 83] Besides, the particularly challenging target for exsogenous contrast agents is tumors in the brain because of the blood brain barrier (BBB) and blood tumor barrier (BTB).[84, 85] The BBB is a physical barrier mainly formed by endothelial cells in brain capillary walls and tight junctions which maintains and protects the sensitive environment of the brain.[86] The BBB moreover plays a significant metabolic role by disposing waste products, metabolizing chemicals and toxins, and markedly limiting the uptake of theranostic drugs in the brain [87]. Tumor growth and progression compromises the integrity of the BBB, such disrupted BBB is referred as blood tumor barrier (BTB) [86], which is characterized by a heterogeneous permeability of small and large molecules. The passive delivery of nanoparticles of appropriate size (20-70 nm) to the brain tumor is considered optimal [84, 88].Although several optoacoustic agents (such as gold nanoparticles [89, 90], MoS_2 nanosheets [91, 92], and semiconducting polymeric nanoparticles [93]) have been reported for optoacoustic imaging of deep brain tumors,

their biodegradability remains a major concern. Therefore, biocompatible nanoparticles with suitable size and high optoacoustic generation efficiency for deep brain tumor imaging are highly desirable

Croconaine dyes and their derivatives, which have narrow and strong absorption bands in the NIR region, express exceptional high chemical, thermal, and photochemical stabilities, and easy modification.[38] In view of their excellent performance, they have been widely applied in organic electronic devices, analytic chemistry, and biomedicine.[40-42, 46, 94] In this study, we hypothesized that PEGylated croconaine dye could be self-assembled into the ultrasmall, cancer-targeting nanoparticle formulations that would be exceptionally versatile as optoacoustic imaging agents for this challenging preclinical tumor models using multispectral optoacoustic tomography (MSOT). The selected croconaine-derived CR780 has a slightly longer absorption maxima, thus resulting in deeper penetration and non-overlapping from hemoglobin with easy unmixing.

To this end, we conjugated the croconaine backbone-derived CR780 dye with a NH2-PEG2000-MAL and the cancer-targeting c(RGDyC) peptide to generate self-assembled nanoparticles with the ability to actively target a brain tumor and enable longitudinal optoacoustic imaging. (**Scheme 3.1**). First, we compared CR780RGD-NPs to the free CR780 dye and the gold industry standard FDA-approved dye ICG in order to show that the physicochemical properties of the nanoparticles (molar absorptivity, OGE, and photostability) are optimal for effective application in optoacoustic imaging. Next, we tested the ability of MSOT to detect localized croconaine nanoparticles in vitro using tissue-mimicking phantoms at depths and beyond that of a mouse brain tumor. We also tested the in vitro BBB penetration capability and cell uptake of these nanoparticles. We further imaged a standard subcutaneous tumor model using CR780RGD-NPs and control non-targeted groups (CR780RAD-NPs) to evaluate whether the c(RGDyC) peptide-functionalized

nanoparticles exhibit active targeting. Finally, the CR780RGD-NPs and CR780RAD-NPs were systemically injected into a mouse brain tumor model to evaluate the ability of the nanoparticles to penetrate BTB and generate localized contrast from the tumor site. Optoacoustic images of the isolated brain and hematoxylin-eosin (H&E) staining of brain slices were used to confirm the presence of CR780RGD-NPs in the brain tumor, even after 24 hours. This study establishes ultrasmall particles based on croconaine dyes as comprehensive preclinical contrast agents which are photostable, and simple to manufacture and functionalize for enhanced tumor targeting. Furthermore, our biosafety study suggests that CR780RGD-NPs are safe for preclinical in vivo application.
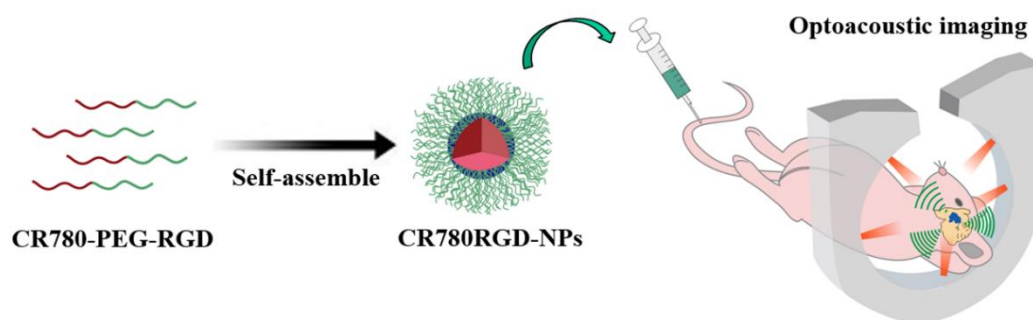
Scheme 3.1. Schematic of the CR780RGD-NPs synthesis and optoacoustic imaging of a brain tumor.

3.2 Experimental section

3.2.1 Materials

Cyclic-RGDyC peptide was bought from GL biochem (Shanghai, China), NH_2-PEG_{2000}-SH, $mPEG_{2000}$-NH_2 was bought from Creative PEGWorks (Chapel Hill, USA). ICG, IR780 iodide, IR820, and MTT were purchased from Sigma-Aldrich (Germany). IRDye800CW NHS Ester was bought from LI-COR Biosciences (Nebraska, USA). Other chemical reagents were obtained from TCI Deutschland GmbH (Eschborn,

Germany).

3.2 Synthesis of CR780, CR780-PEG-RAD, and CR780-PEG-RGD

CR780 was synthesized according to a previously reported method.[51] ^{1}H NMR (500 MHz, DMSO-d_6) δ8.52 (s, 2H), 7.03 (d, J = 6 Hz, 2H), 3.99 (d , J = 16.6 Hz, 4H), 3.52 (t, J = 14.1 Hz, 5H), 2.73 − 2.60 (m, 2H), 2.04 (d, J = 12.9 Hz, 4H), 1.73 (q, J = 13.3 Hz, 4H). MALDI: m/z = 529.183 [M + H]$^+$.
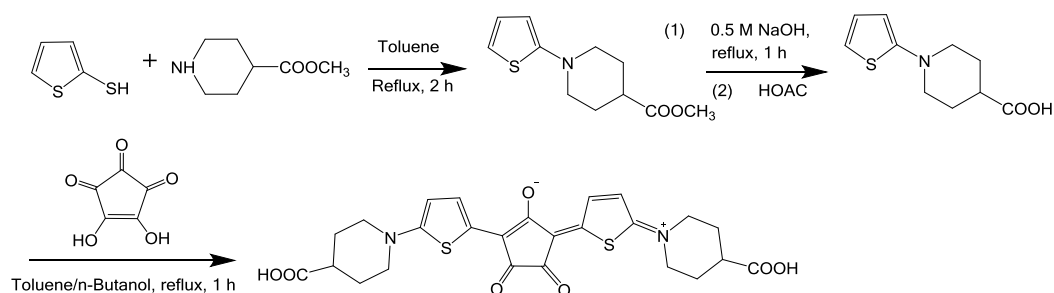
Scheme 3.2. Schematic for synthesizing CR780.
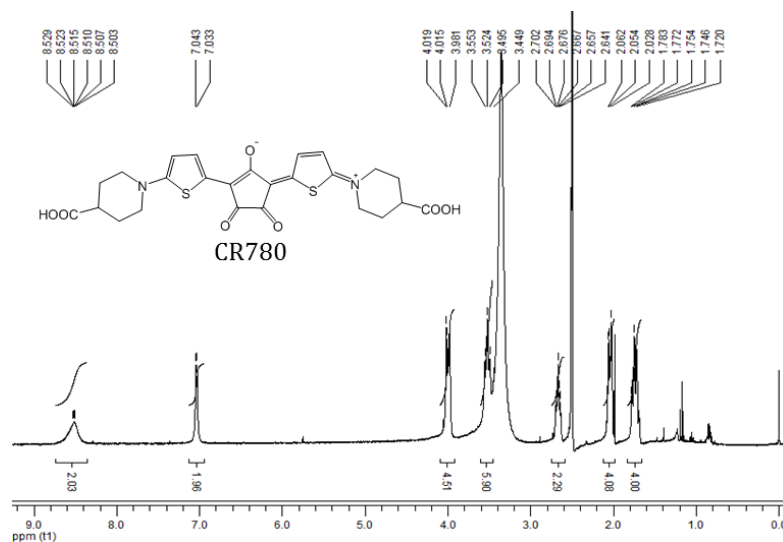
Figure 3.1. ^{1}H NMR (500 MHz, DMSO-d$_6$) of CR780.
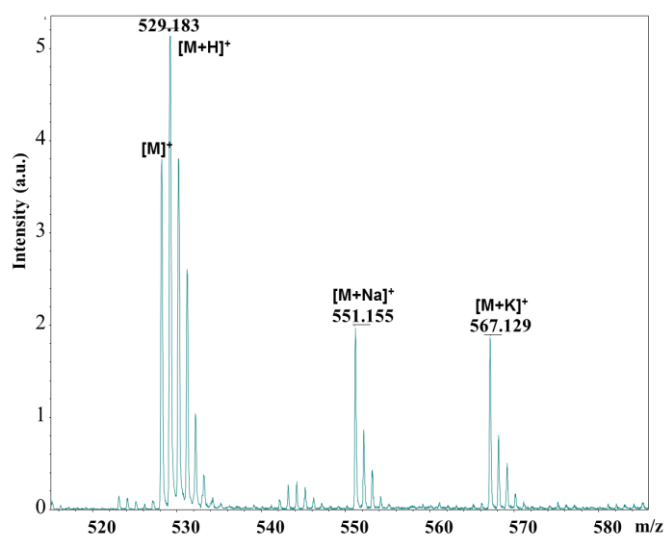
Figure 3.2. MALDI-TOF mass spectrum of CR780.

CR780-PEG-RAD or CR780-PEG-RGD was synthesized by esterification. Briefly, CR780 (0.1 mmol), EDC·HCl (0.12 mmol), NHS (0.12 mmol) were dissolved in 2 mL of DMF. The mixture was stirred for 2 h, followed by the addition of NH_2-PEG_{2000}-SH (0.1 mmol). After stirring at room temperature for 24 h, CR780-PEG-SH was purified by reversed-phase HPLC column. Then CR780-PEG-SH was reacted with c(RADyC) or c(RGDyC) peptide (0.1 mmol) under slightly acidic condition for 2 h. CR780-PEG-RAD or CR780-PEG-RGD were purified by reverse-phase HPLC column and then dry-freezing.
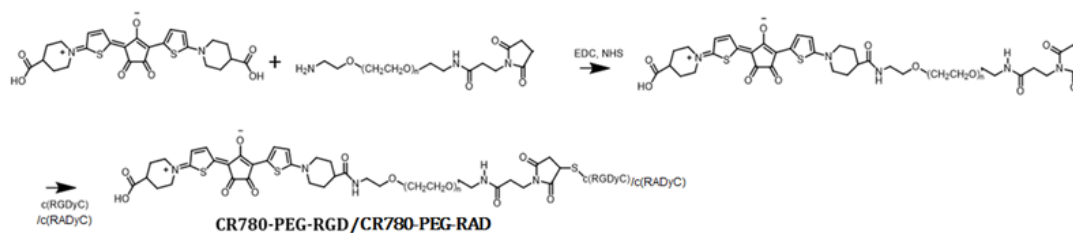
Scheme 3.3. Schematic for synthesizing CR780-PEG-RAD, and CR780-PEG-RGD.

3.3 Preparation of CR780RAD-NPs and CR780RGD-NPs

CR780-PEG-RAD (1 mg), or CR780-PEG-RGD (1 mg) was dissolved in deionized water (1 mL) and sonicated for 5 min, obtaining uniform-sized CR780RAD-NPs, or CR780RGD-NPs.

3.4 Characterization

^{1}H NMR spectrum was recorded on a Bruker spectrometer at 500 MHz. The m/z ratios of the compounds were measured with a MALDI UltrafleXtreme (Bruker) using dihydroxybenzoic acid as matrix. The molar absorption coefficient and quantum yield of dyes were calculated as previously described.[71] For the quantum yield measurement, three concentrations of dyes in ethanol (absorbance below 0.1) were prepared and corresponding fluorescence intensity was evaluated, then the fluorescence intensity was plotted against absorbance and fitted into a linear function. As the quantum yield of ICG (in ethanol) is 0.05, then the quantum yield of other dyes with the same solvent were calculated as follows: $Slope_{dyes}/Slope_{ICG}*0.05$.[95] The nanoformulations were characterized by ZEISS Libra 120 PLUS transmission electron microscopy (TEM) and dynamic light scattering (DLS) (Malvern Zetasizer). Absorption spectra were measured with UV-1800 spectrometer (Shimadzu, Japan). Optoacoustic spectra were collected by an MSOT inVision 256-TF measurement and further normalization with ink, Brilliant Black BN.[72] Optoacoustic generation efficiency (OGE) was equal to the slope of the line where corrected optoacoustic intensities are plotted against absorbance.[72] The photostability of samples was measured using an MSOT inVision 256-TF with pulsed laser irradiation (fluence 10 mJ/cm^2, 10 Hz pulse repetition rate, 1 hour).

3.5 Penetration depth estimation

Tissue-mimicking cylindrical phantoms with different radii were made by using the mixture of intralipid (2 mL), agar (2 g), India ink solution (98 mL, absorbance 0.15 at 780 nm).[96, 97] Then tubing containing different concentration of CR780RGD-NPs was inserted into the ink-agar phantoms. Optoacoustic signals were measured using MSOT. *In vivo* penetration depth experiments were done by injecting CR780RGD-NPs (5 μM) in the mice brains using small Hub RN needle (Hamilton, Timis, Romania)

(bregma + 1.0 mm, left lateral 2.0 mm and depth 5.0 mm). Then optoacoustic signal was measured using MSOT.

3.6 *In vitro* BBB penetration capability

The *in vitro* BBB model was constructed to explore the BBB permeability of nanoparticles.[98, 99] Briefly, 10^5 of HBEC-5i cells were cultured with multiple layers on a Transwell filter system (pore size 0.4 μm). CR780-derived nanoparticles (50μM) were added into the apical chamber for 4 h incubation time at 37 °C, then the medium in the basolateral chambers was collected to measure the absorption intensities at 780 nm. As the absorption intensity of CR780-derived nanoparticles has a linear relationship with the concentrations of NPs, the transport efficiency of NPs was calculated by dividing the weight of NPs in the basolateral chamber by the weight of 50μM NPs [100].

3.7 *In vitro* experiments

The cytotoxicity of CR780-based nanoparticles was assessed by MTT assay. Briefly, U87MG cells were sub-cultured in a 96-well plate (1×10^4 cells/well) overnight. The cells were treated with different concentrations of CR780RAD-NPs and CR780RGD-NPs for 24 h. Then the cells were washed with PBS followed by 10 μL of MTT solution (5 mg/mL). After an additional 4 h incubation, the medium was aspirated and refilled with 100 μL of DMSO. The absorbance at 565 nm of each well was measured using a Tecan Infinite M200 Plate Reader (Salzburg, Austria).

Cellular internalization was used to assess targeting by c(RGDyC) peptide-modified nanoparticles. A total of 1×10^4 of cells were sub-cultured on glass dishes for 24 h. Then CR780RAD-NPs or CR780RGD-NPs (50 μM) were added to incubate for another 4 h. Cellular uptake was observed based on fluorescence signal from CR780 based nanoparticles by Leica DMI3000 B Inverted Microscope (Wetzlar, Germany).

3.8 Brain tumor mice model

All procedures involving animal experiments were approved by the Animal Care and Handling Office of Helmholtz Zentrum München and by the Government of Upper Bavaria. Subcutaneous U87MG tumor models were prepared by subcutaneously implanting a suspension of 2×10^6 U87MG cells into nod scid shorn mice (6 weeks). The orthotopic tumor models were prepared using nod scid shorn mice (6 weeks). U87MG cells (4×10^5) in PBS (3 µL) were implanted into the mouse striatum (bregma + 1.0 mm, left lateral 2.0 mm, and depth 3.0 mm). The tumor models were ready after four weeks' implantation.[101]

3.9 *In vivo* optoacoustic imaging

Mice bearing brain tumors were anesthetized by 1% isoflurane delivered via a nose cone, and then 100 µL of CR780RAD-NPs or CR780RGD-NPs (1 mM) were injected via the tail vein. *In vivo* optoacoustic images were acquired at different time points before and after injection (0, 4, 24 h). The averaged optoacoustic signals of brain tumor regions were extracted using ViewMSOT 4.0 software (iThera Medical, Munich).

3.10 Ex vivo optoacoustic imaging, fluorescence imaging and histological analysis

The mice were sacrificed at 24 hour post-injection and the brain, kidney, heart, liver, and spleen were isolated and scanned by MSOT. Isolated brains were fixed and frozen in OCT embedding gel. The tissue blocks were sectioned in the axial dimension, at a 300 mm micron pitch, and bright field as well as fluorescence images were recorded from each slice using a fluorescence cryosectioning imaging (FCSI) system. The FCSI system is based on a cryotome (CM 1950, Leica Microsystems, Wetzlar, Germany), fitted with a motorized spectral illumination and multi-spectral CCD-based detection in epi-illumination mode. The cryosection slices were captured on glass slides. The slides obtained were stained by H&E and imaged with a light microscope (Carl Zeiss).

3.11 Blood hematology and biochemistry analyses

C57BL/6 mice were randomly divided into 4 groups (5 mice per group). The control group was i.v. injected with 100 µL of PBS buffer, and the other 3 groups were i.v. injected with 100 µL of CR780RGD-NPs (1 mM). On days 1, 7, and 14, blood from CR780RGD-NPs treated group was sampled. From the control group, blood was sampled on day 14. The blood samples were then used for hematology and blood biochemistry test using Hitachi 917 Clinical Chemistry Analyzer (Roche, Germany).

3.3 Results

3.3.1 Synthesis and characterization of CR780

CR780 with two carboxyl groups was prepared by a three-step reaction (nucleophilic substitution, condensation, and ester hydrolysis), which confirmed the right compound by ^{1}H-NMR spectrum and mass spectrum (**Scheme 3.1**, **Figure 3.1**,**3.2**). **Table 3.1** shows the experimental comparison of the photophysical properties of CR780 with previously reported optoacoustic dyes (ICG, IRDye800CW, IR780 iodide, and IR820) in ethanol. [27-29] Comparison data shows that CR780 has a strong absorption peak at 780 nm and a NIR fluorescence emission peak at 800 nm. CR780 exhibits a molar absorption coefficient significantly higher than ICG and other dyes and a much smaller quantum yield (88% less than ICG). We further experimentally compared the OGE of CR780 with ICG, IRDye800CW, IR780 iodide, and IR820. The slope value at each point indicates the OGE, the ratio of optoacoustic intensity and absorbance. OGE values indicate the ability of the compound to convert optically absorbed energy into pressure waves that give a strong optoacoustic signal. **Figure 3.3** shows that CR780 exhibits a much higher optoacoustic intensity compared with the other dyes. Our results clearly show that CR780 exhibits an OGE that is 1.79 times

higher than IR820, 1.85 times higher than ICG, 3.29 times higher than IRDye800CW, and 8.5 times higher than IR780 iodide. Based on the high molar absorption coefficient and OGE, we set out to use the CR780 to prepare ultrasmall, self-assembled nanoparticles that are suitable for brain tumor-targeted imaging.

Table 3.1. Photophysical properties of CR780, ICG, IRDye800CW, IR780 iodide, and IR820, measured in ethanol.

Dye	Fluorescence Ex/Em (nm)	Molar absorption coefficient ($M^{-1} cm^{-1}$) in ethanol	Quantum yield in ethanol
CR780	780/800	$3.4 \cdot 10^5$ at 780 nm	0.006
ICG	780/810	$2.1 \cdot 10^5$ at 780 nm	0.05
IRDye800CW	780/800	$2.54 \cdot 10^5$ at 780 nm	0.125
IR780 iodide	780/800	$2.8 \cdot 10^5$ at 780 nm	0.081
IR820	820/835	$3.03 \cdot 10^5$ at 820 nm	0.024
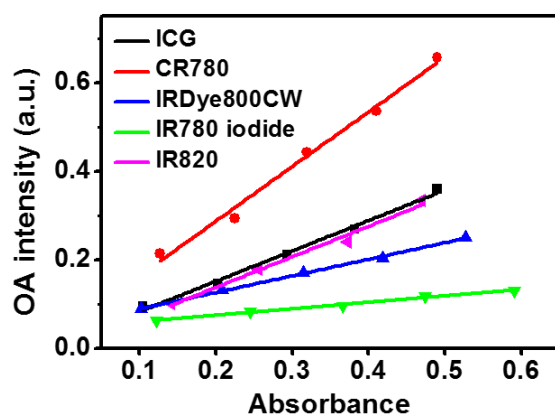
Dyes	OGE
ICG (800nm)	0.6855
CR780 (780nm)	1.2338
IRDye800 (780nm)	0.3741
IR780 iodine(795nm)	0.144
IR820 (840nm)	0.6892

Figure 3.3. OGE of ICG at 800 nm, CR780 at 780 nm, IRDye800CW at 780 nm, IR780 iodide at 795 nm, and IR820 at 840 nm. All the dyes were measured in 10% FBS.

3.3.2 Synthesis and characterization of CR780RGD-NPs

We conjugated the hydrophobic CR780 to hydrophilic NH$_2$-PEG$_{2000}$-SH and c(RGDyC) peptide to generate nanoparticles that can self-assemble based on

hydrophobic and hydrophilic interactions.[102] The c(RGDyC) peptide is used to target $\alpha_v\beta_3$ integrin receptors,[103] which are expressed on activated endothelial cells of tumor neovasculature and tumor cells.[104] In parallel, as controls for the tumor-targeting ability of the nanoparticles, we prepared CR780RAD-NPs. **Scheme 3.3**, **Figure 3.4** shows the CR780-PEG-RGD synthesis steps and corresponding MALDI-TOF analyses indicating the purity of the compounds. Based on the hydrophilic and hydrophobic interactions, CR780RGD-NPs can be formulated after a brief sonication in water. **Figure 3.5a** shows that the self-assembled CR780RGD-NPs generate a clear green, homogeneous aqueous solution. We evaluated the shape and size of the nanoparticles using transmission electron microscopy (TEM) and dynamic light scattering (DLS). **Figure 3.5b** and **Figure 3.6** show that the CR780RGD-NPs exhibit circular morphology with an average size of approximately 25 nm. The control groups from CR780RAD-NPs show a similar size distribution (**Figure 3.7**). **Figure 3.5c,d** shows the optical and optoacoustic spectrum of CR780RGD-NPs, which have a narrow and intense peak at 780 nm, similar to CR780RAD-NPs (**Figure 3.8**). The zeta potential of CR780RAD-NPs and CR780RGD-NPs are -16.9 mV and -17.2 mV, respectively. We measured the absorbance intensities, particle size, and zeta potential of CR780-derived nanoparticles for 14 days (**Figure 3.9**), with no significant changes recorded. Next, we compared the quantum yield and OGE of CR780 and CR780RGD-NPs in the water phase, where CR780RGD-NPs had a 2.33-fold higher quantum yield and a 1.63-fold higher OGE than CR780, as PEGylation and self-assembly improve the dispersibility of hydrophobic CR780 (**Figure 3.10**).[54] We then compared the OGE of CR780-derived nanoparticles with ICG in 10% FBS due to the instability of ICG in the water phase. **Figure 3.5e** shows a much higher slope value for CR780RAD-NPs and CR780RGD-NPs than for ICG. The calculated OGE value was 1.85 times higher for CR780-derived nanoparticles than for ICG, indicating that both nanoformulations are suitable for optoacoustic imaging. We further evaluated the photostability of

CR780RGD-NPs by continuously irradiating the samples with pulsed laser (fluence 10 mJ/cm^2) for 1 h and compared the changes in optoacoustic intensity against ICG. **Figure 3.5f** shows that CR780, CR780RAD-NPs, and CR780RGD-NPs remained unbleached, whereas ICG was completely bleached under the same irradiation conditions. These results of the characterization studies clearly indicate that CR780RGD-NPs are ultrasmall (average particle size 25 nm) and can generate strong optoacoustic signals. The optimal physicochemical properties of CR780RGD-NPs make them suitable for *in vivo* optoacoustic imaging of orthotopic brain tumors.
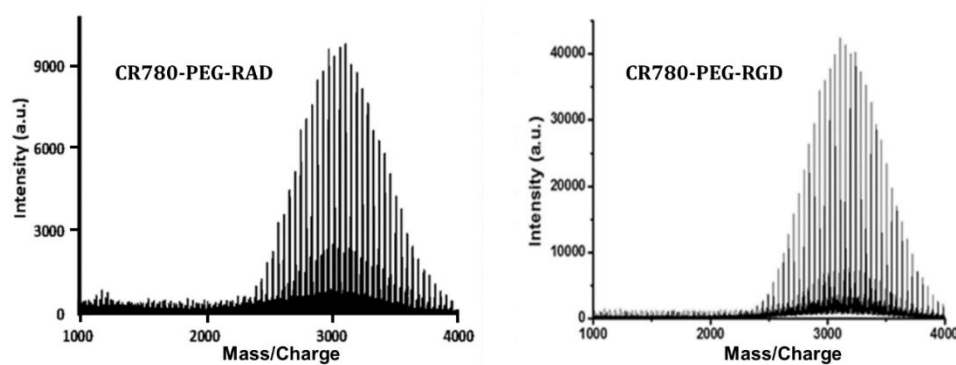
Figure 3.4. MALDI-TOF analyses of CR780-PEG-RAD, and CR780-PEG-RGD.
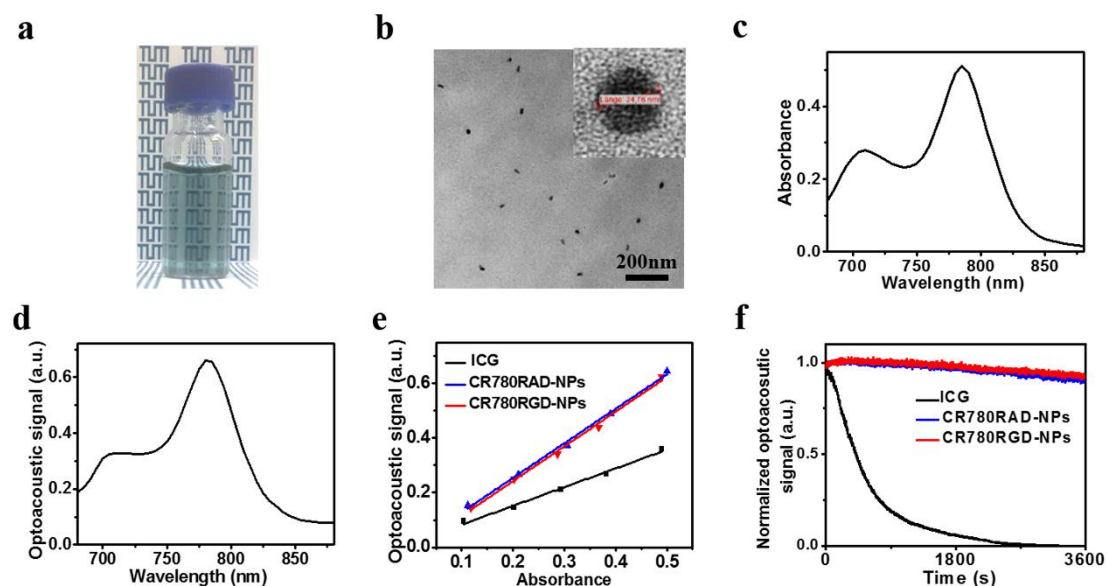
Figure 3.5. (**a**) CR780RGD-NPs in deionized water. (**b**) TEM image of CR780RGD-NPs. (**c**) Optical spectrum of CR780RGD-NPs. (**d**) Optoacoustic spectrum of

CR780RGD-NPs. (**e**) Optoacoustic signal intensity of ICG, CR780RAD-NPs, and CR780RGD-NPs at different concentration. (**f**) Optoacoustic signal changes of ICG, CR780RAD-NPs, and CR780RGD-NPs after pulsed laser irradiation (fluence 10 mJ/cm^2, 10 Hz pulse repetition rate, 1 h).
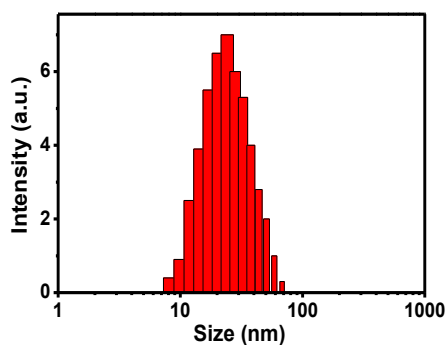
Figure 3.6. DLS analysis of CR780RGD-NPs.
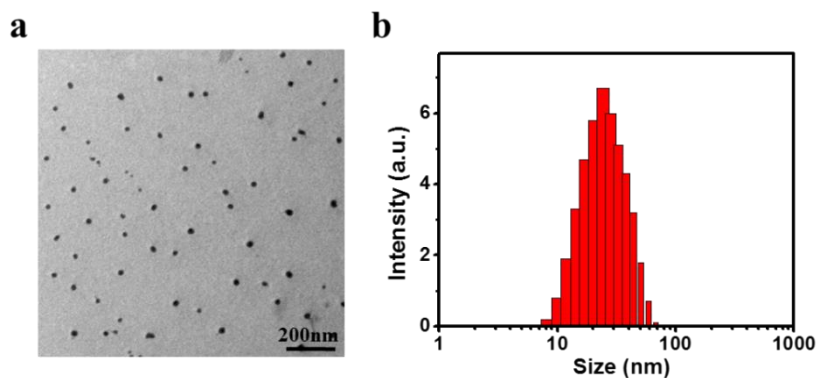
Figure 3.7. (**a**) TEM images and (**b**) DLS analysis of CR780RAD-NPs.
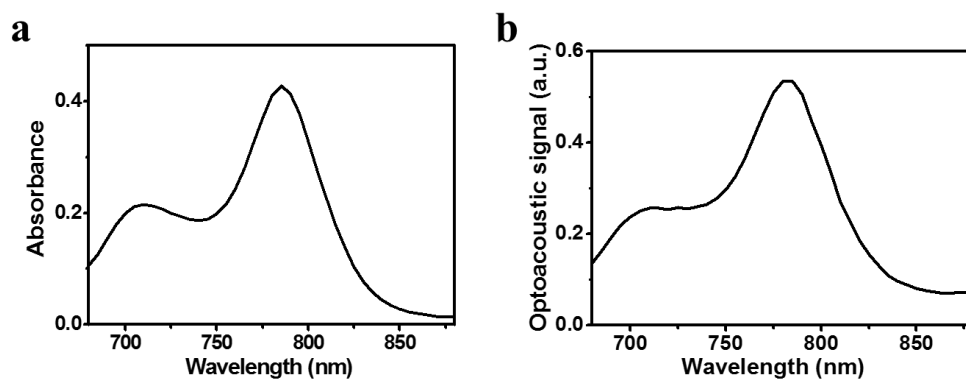
Figure 3.8. (**a**) Optical spectrum and (**b**) optoacoustic spectrum of CR780RAD -NPs.
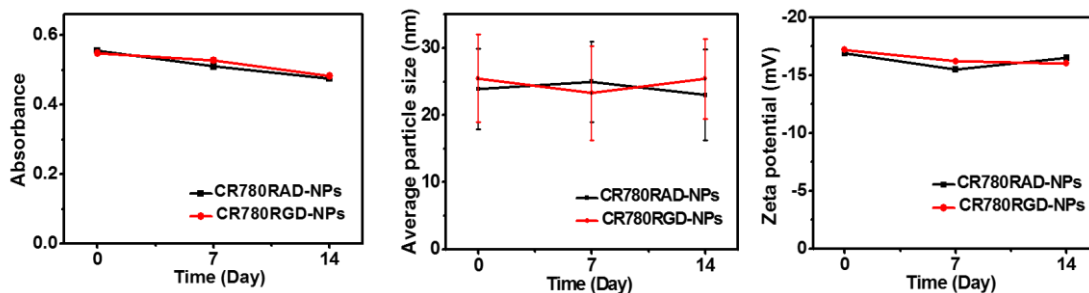
Figure 3.9. Absorption intensity, average particle size, and zeta potential of CR780RAD-NPs and CR780RGD-NPs in water over 14 days.
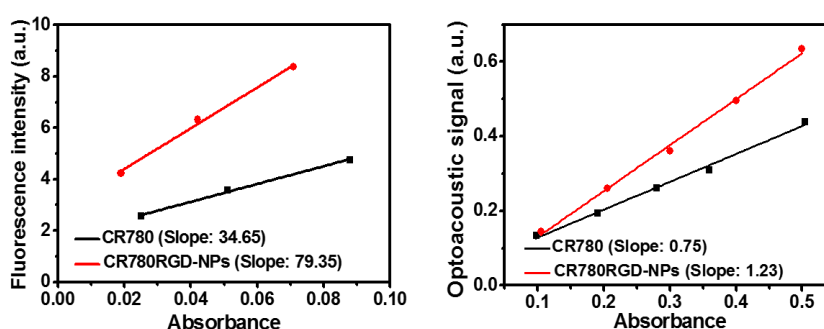
Figure 3.10. Fluorescent and optoacoustic signal intensities of CR780 and CR780RGD-NPs at different concentrations in the water phase.

3.3.3 Optoacoustic imaging at different depths with CR780RGD-NPs *in vitro* and *in vivo*

To explore the potential of CR780RGD-NPs for deep tissue imaging, we assessed the optoacoustic imaging depth at 780 nm using tissue-mimicking phantoms. Cylindrical phantoms of agar containing India ink were prepared to fit within a commercially available MSOT system, and tubing filled with 5 μM CR780RGD-NPs was placed in the center. Various phantoms were created with different radii to examine the imaging of nanoparticles at different depths. **Figure 3.11a** shows the optoacoustic images of tissue-mimicking phantoms of increasing thickness; the optoacoustic signal of CR780RGD-NPs placed in the tubing was monitored from the center. **Figure 3.11b** shows CR780RGD-NPs contrast levels correlated with phantom thickness and nanoparticles concentration. Detection limits is defined also in the context of lesion

concentration, lesion size and depth [105], thus the lower detection limit of the unmixing method for CR780RGD-NPs in the 7mm or 9mm depth of mimicking phantom is 1.25μM. Optoacoustic contrast due to CR780RGD-NPs was visible at different depths, confirming the potential for the optoacoustic detection of CR780RGD-NPs from deep brain tumor.

To examine whether CR780RGD-NPs could generate strong optoacoustic signals at different depths within tumors *in vivo*, despite background noise due to endogenous contrast agents like blood and reflections at the skull, we injected CR780RGD-NPs into a mouse brain at a depth of 5 mm. **Figure 3.11c** shows the unmixed optoacoustic images of the mouse brain before and after implantation of CR780RGD-NPs. A strong optoacoustic signal from the implanted CR780RGD-NPs at different depths in the brain was evident. **Figure 3.11d** shows no variation in optoacoustic intensity across different depths in animals prior to nanoparticle implantation, whereas the optoacoustic intensity was approximately 3.5 times higher at a 5 mm depth after CR780RGD-NP implantation. These results clearly indicate that upon uptake and accumulation in the brain tumor, the CR780RGD-NPs can generate a strong optoacoustic signal easily detectable over background noise from the skull bone, blood, and brain tissue.
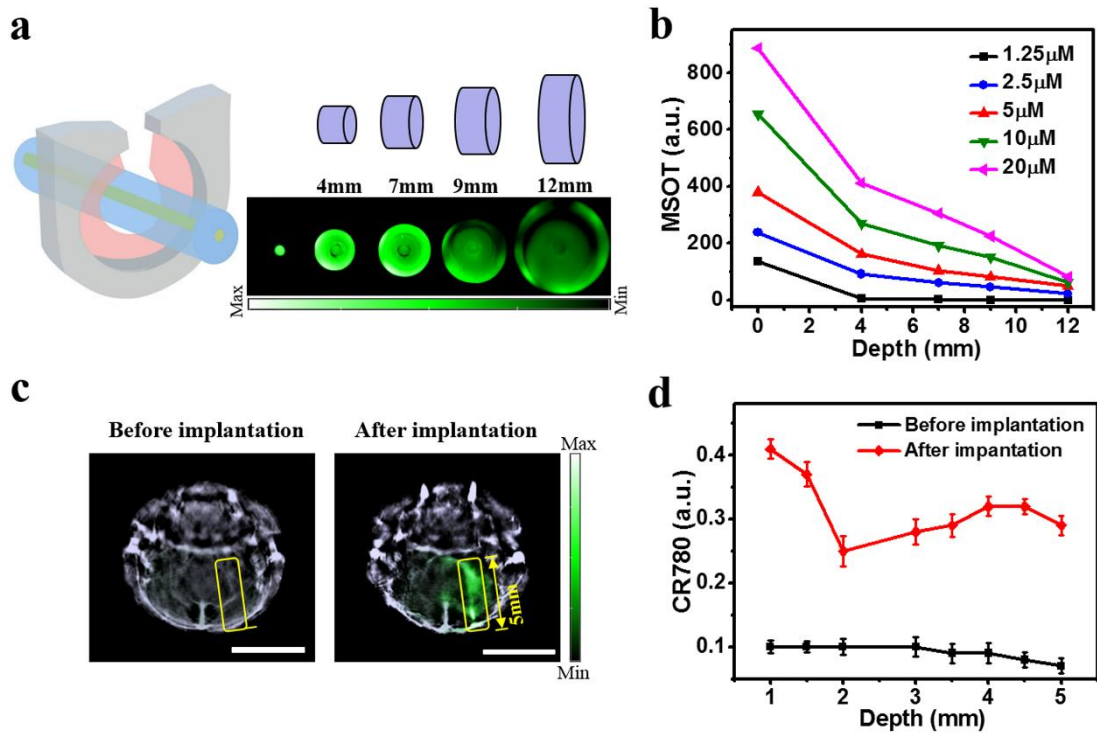
Figure 3.11. (**a**) Optoacoustic imaging of tissue-mimicking phantoms of increasing thickness containing 5 μM CR780RGD-NPs at 780 nm. (**b**) Optoacoustic intensities of different concentration of CR780RGD-NPs from phantoms of different thicknesses. (**c**) Unmixed MSOT imaging of a mouse brain before and after injection of CR780RGD-NPs (5 μM). Scale bar, 5 mm. (**d**) Optoacoustic intensities of ROI at different depths *in vivo*.

3.3.4 *In vitro* BBB penetration capability and cell uptake

We next carried out an *in vitro* BBB penetration test using HBEC-5i (human brain microvascular endothelial cell line) derived BBB model (**Figure 3.12**). HBEC-5i cells were cultured with multiple layers on a Transwell filter system (pore size 0.4 μm).[99] CR780-derived nanoparticles (50μM) were added into the apical chamber, and the absorbance of the solution in apical chambers and basolateral chambers was evaluated at 4 h to calculate the transport efficiency. The results show that the transmembrane transport efficiency of nanoparticles was 10.9±1.2%, 11.8±1% for CR780RAD-NPs,

CR780RGD-NPs, respectively. Results indicate that due to the ultrasmall size, these particles might also penetrate through the *in vivo* compromised BBTB. Next we tested the *in vitro* active targeting ability of CR780RGD-NPs using U87MG cells (glioblastoma cell line). Uptake of non-targeted CR780RAD-NPs and integrin $\alpha_v\beta_3$-targeted CR780RGD-NPs by U87MG cells were monitored by fluorescence microscopy after 4 h treatment with nanoparticles. Cells treated with CR780RGD-NPs showed a stronger fluorescence signal than those treated with the non-targeting groups (**Figure 3.13a**). We further evaluated the cytotoxic effects of nanoparticles in U87MG cells by treating them with different concentrations of CR780RAD-NPs and CR780RGD-NPs for 24 h. An MTT assay for assessing cell metabolic activity showed no appreciable cytotoxicity (**Figure 3.13b**).
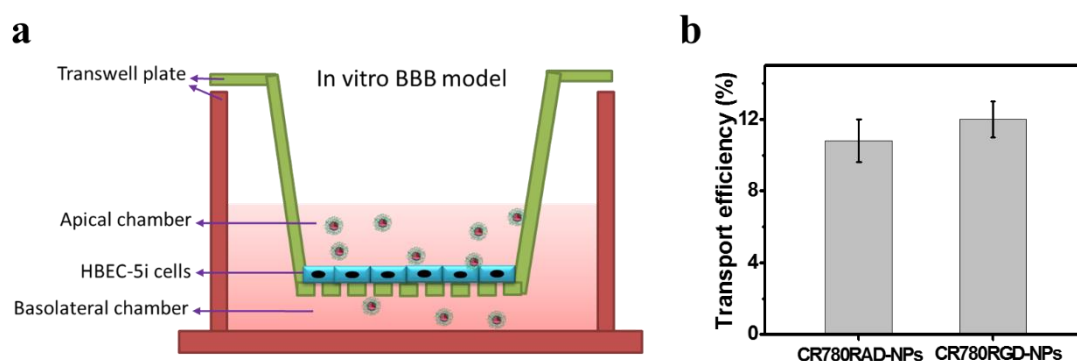
Figure 3.12. (**a**) Schematic overview of the *in vitro* BBB model and BBB penetration capability of nanoparticles. (**b**) Transport efficiency of CR780-derived nanoparticles (50μM) across the BBB model *in vitro* at the 4 hour time point.
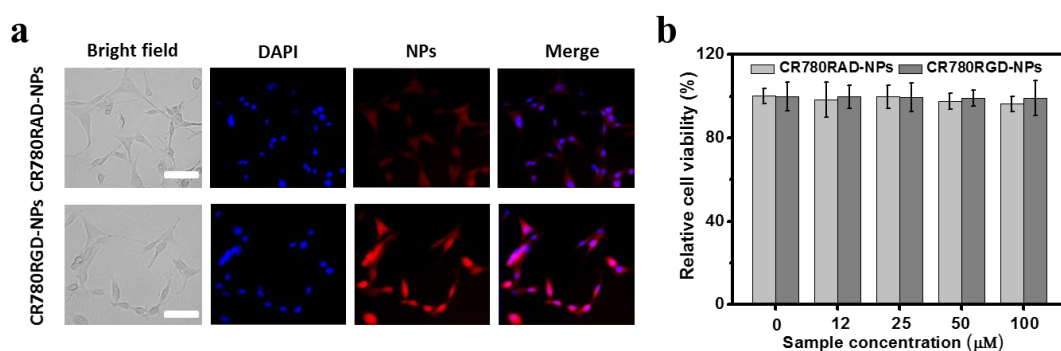
Figure 3.13. (**a**) Fluorescence images of U87MG cells after 4 h of treatment with CR780RAD-NPs, or CR780RGD-NPs. Blue color: DAPI staining, red color: nanoparticles fluorescence. Scale bar, 50 μm. (**b**) Viability of U87MG cells incubated with different concentrations of croconaine-based nanoparticles for 24 h.

3.3.5 *In vivo* optoacoustic imaging of brain tumor

To test the ability of CR780RGD-NPs to specifically accumulate in a brain tumor, we first subcutaneously implanted U87MG cells and subsequently injected a type of nanoparticle (i.e. CR780RAD-NPs or CR780RGD-NPs) *via* the tail vein. As expected due to their ultrasmall size, these nanoparticles reached the tumor within four hours of treatment (**Figure 3.14**). However, due to integrin $\alpha_v\beta_3$ receptor targeting ability, the CR780RGD-NPs were retained in the tumor longer than non-targeted CR780RAD-NPs. Based on these preliminary findings, we continued with the imaging of the orthotopic glioblastoma models that were injected with a type of nanoparticle (i.e. CR780RAD-NPs or CR780RGD-NPs) *via* the tail vein. **Figure 3.15a** shows representative optoacoustic images of orthotopic brain tumors from each treatment group, acquired using the MSOT system at different time points (0 h, 4 h, 24 h) and at multiple wavelengths (680-900 nm). As observed in MSOT images from 4 h, both targeted and non-targeted nanoparticles were able to effectively reach the brain region because of the disrupted BBB (BTB), while the BBB penetration capability of CR780RGD-NPs was not evident in the normal murine brain model because of an intact BBB (**Figure 3.17**). However, only CR780RGD-NPs were retained in the brain tumor for at least 24 h and generated strong optoacoustic signals due to the enhanced permeability and retention effect (EPR) and active targeting. The optoacoustic signals at 4 h and 24 h were much stronger in mice treated with CR780RGD-NPs than in mice treated with CR780RAD-NPs, indicating the advantage of active targeting and long-term persistence in the bloodstream. The optoacoustic signal due to CR780 at 4 h was higher

than at 24 h, indicating that some of CR780RGD-NPs undergo systemic clearance from the tumor vasculature. The optoacoustic signal was recorded in the tumor down to a depth of 5.5 mm, confirming the ability of MSOT to detect CR780RGD-NP in deep-seated brain tumors. **Figure 3.15b** shows the optoacoustic reconstruction spectrum at different time points from the CR780RGD-NPs' treated group. Spectral analysis of the brain tumor region at multiple wavelengths clearly indicates time-dependent absorption spectra changes and a strong peak at 780 nm, confirming the presence of CR780 in the region of interest. **Figure 3.15c** shows that the signal intensity with CR780RGD-NPs is approximately 3.15- and 3.7-fold stronger than with CR780RAD-NPs at 4 h and 24 h, respectively. **Figure 3.15d** shows optoacoustic signal intensity ratios of tumor-to-contralateral brain region, before and after treatment with CR780RAD-NPs and CR780RGD-NPs. Compared to control CR780RAD-NPs, the CR780RGD-NPs preferentially accumulated in the tumor region of the brain, These results in one mouse were confirmed in four additional mice treated with CR780RGD-NPs (**Figure 3.18a**). The tumor accumulation of CR780RGD-NPs confirms the accumulation of particles due to the EPR effect and active targeting via the c(RGDyC) peptide.

To validate the results of *in vivo* MSOT based optoacoustic tomography, the brains were isolated from all animals 24 h after MSOT imaging. Optoacoustic images were acquired for isolated whole brains, and fluorescence images were acquired following brain sectioning. **Figure 3.16** shows strong optoacoustic and fluorescence signals due to CR780 presence in the tumor region of animals treated with CR780RGD-NPs. A very weak optoacoustic and fluorescence signal was observed in the brains analyzed *in vivo* and *ex vivo* from animals treated with CR780RAD-NPs. We confirmed the presence of the tumor in the brain by cryo-slicing and H&E staining, while CR780RGD-NP accumulation was confirmed by fluorescence imaging (**Figure 3.16**, **3.18b**).
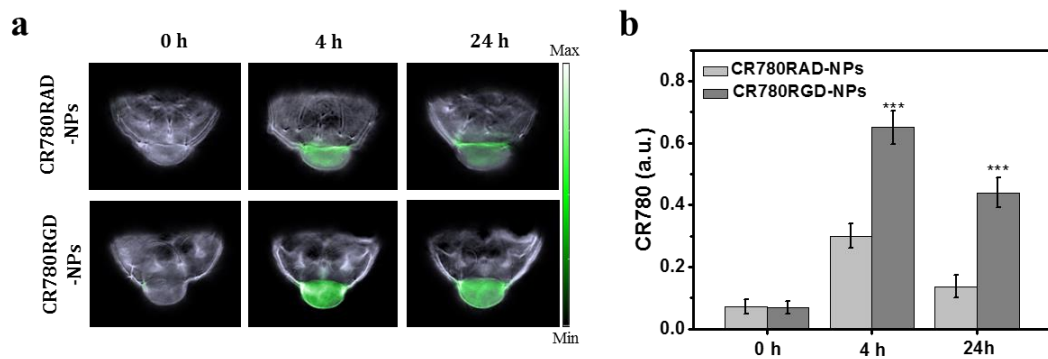
Figure 3.14. (a) Unmixed MSOT imaging of mice bearing subcutaneous U87MG tumors after intravenous injection of non-targeting CR780-NPs and CR780RAD-NPs or tumor-targeting CR780RGD-NPs. (b) CR780 concentrations in the tumors were measured over time. (***p < 0.001)
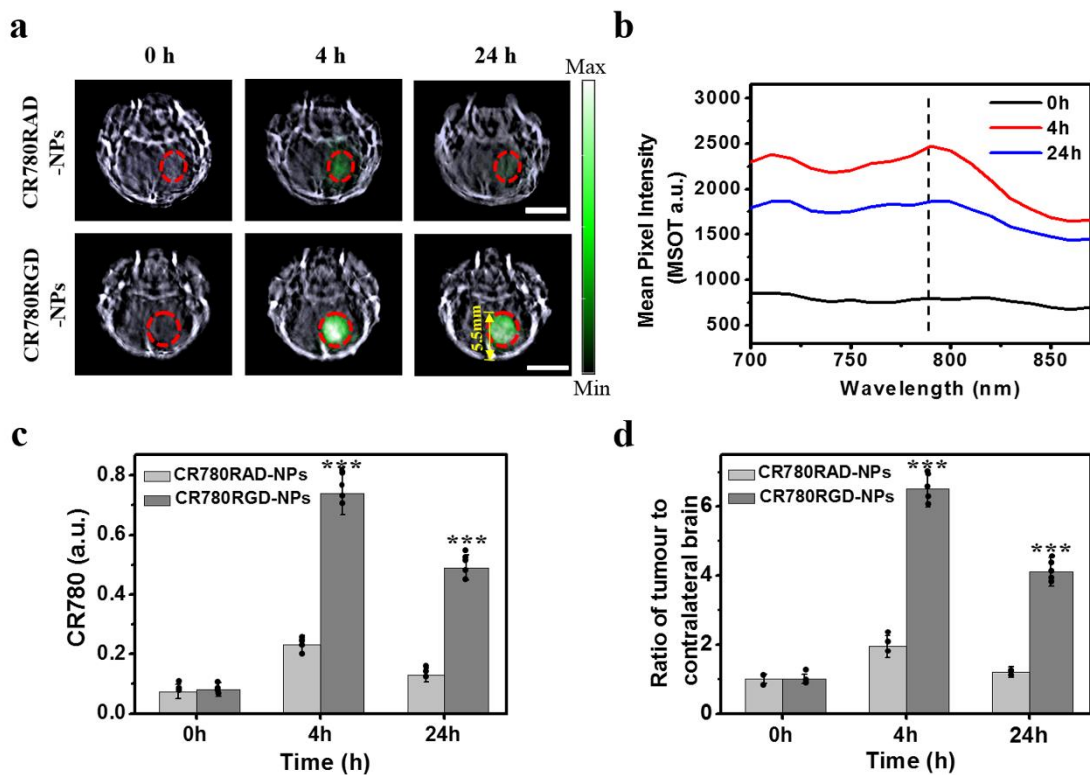
Figure 3.15. *In vivo* MSOT imaging of CR780RAD-NPs and CR780RGD-NPs in a mouse brain. (a) Representative unmixed image of U87MG bearing orthotopic glioblastoma i.v. injected with 100 μL of CR780RAD-NPs or CR780RGD-NPs (1 mM). Signals are shown only for the brain region (n=5). Scale bar, 5 mm. (b) Optoacoustic

spectra from the tumor region of the animal treated with CR780RGD-NPs at different time points. (c) CR780RAD-NPs and CR780RGD-NPs concentrations in the tumor region and (d) The derived optoacoustic signal intensity ratios of tumor-to-contralateral brain region, before and after treatment with CR780RAD-NPs and CR780RGD-NPs.
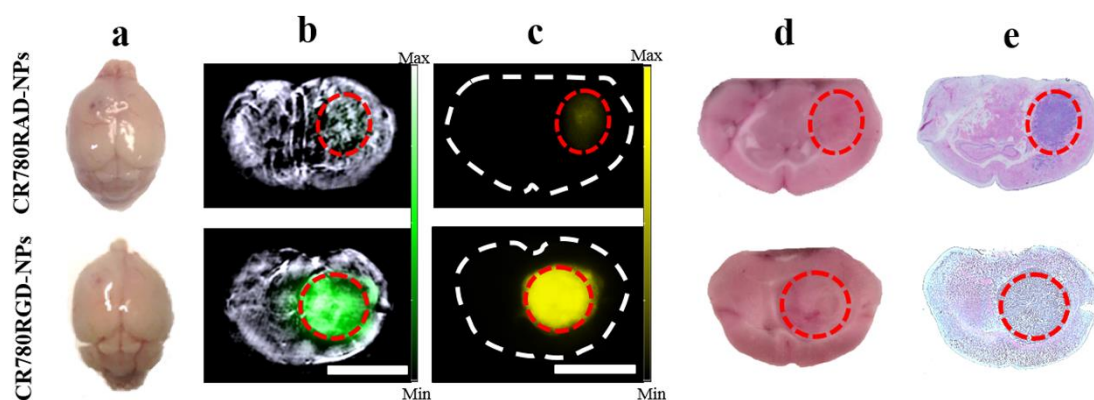
Figure 3.16. (a) Photographs of representative brains isolated from tumor-bearing mice treated with CR780RAD-NPs or CR780RGD-NPs (n=5). (b) Unmixed MSOT images of isolated brains. (c) Fluorescence images of isolated brain slices. (d, e) Bright fields and HE staining of brain tumor slices.
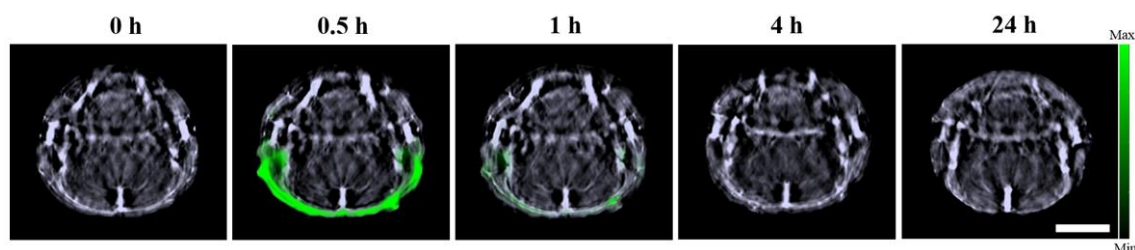
Figure 3.17. *In vivo* optoacoustic imaging of a normal murine brain using 100 μL CR780RGD-NPs (1mM). Scale bar, 5mm.
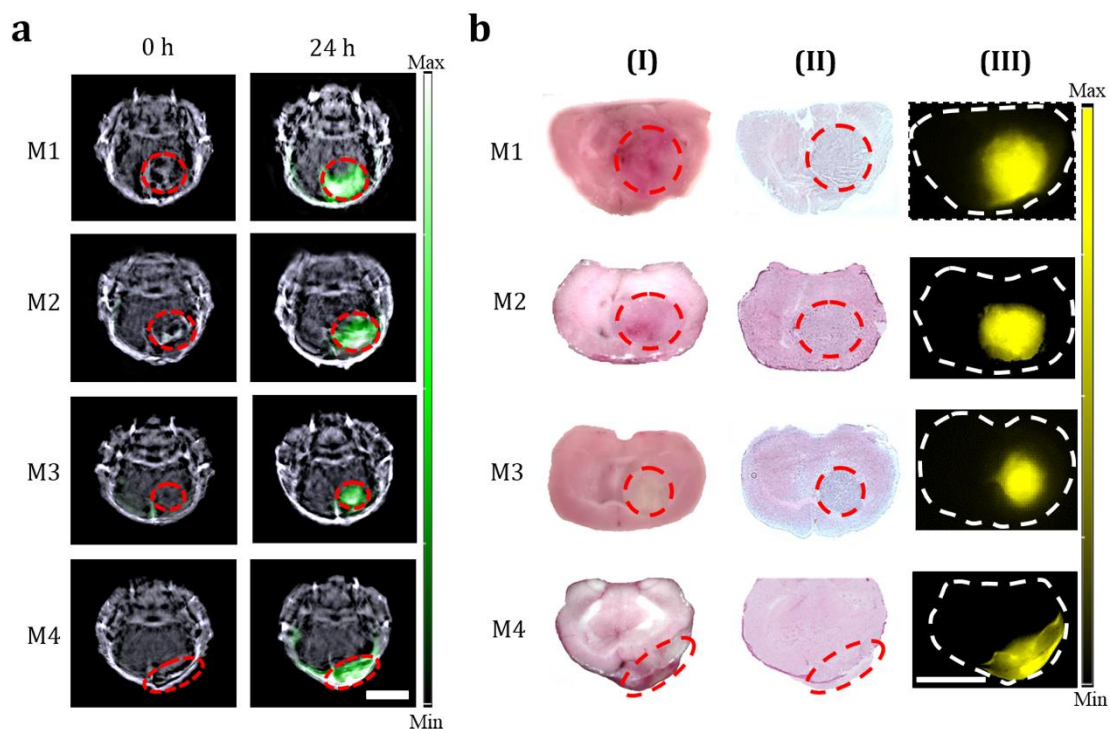
Figure 3.18. (a) *In vivo* MSOT imaging of orthotopic brain tumors in mice after intravenous injection of non-targeting tumor-targeting CR780RGD-NPs. Signals are shown only for the brain region. (b) Bright field, HE staining, and fluorescence imaging of brain slices.

3.3.6 *In vivo* biodistribution of CR780RGD-NPs

Biodistribution of CR780RAD-NPs and CR780RGD-NPs was monitored in vital organs. After intravenous injection of respective nanoparticles in mice, mice were sacrificed after 24 h of treatment, and all vital organs were isolated and scanned using MSOT. **Figure 3.19a** shows optoacoustic signal due to the presence of CR780 dye in different organs. Optoacoustic signal intensity was quantified in the resected organs (**Figure 3.19b**). The two types of nanoparticles showed the similar level of uptake in the liver and slightly lower uptake in kidney, heart, and spleen. This distribution pattern is similar to that reported for inorganic and organic nanoparticles, reflecting the fact that nanoparticles larger than 10 nm are cleared mainly through the hepatobiliary

61

system.[106, 107]
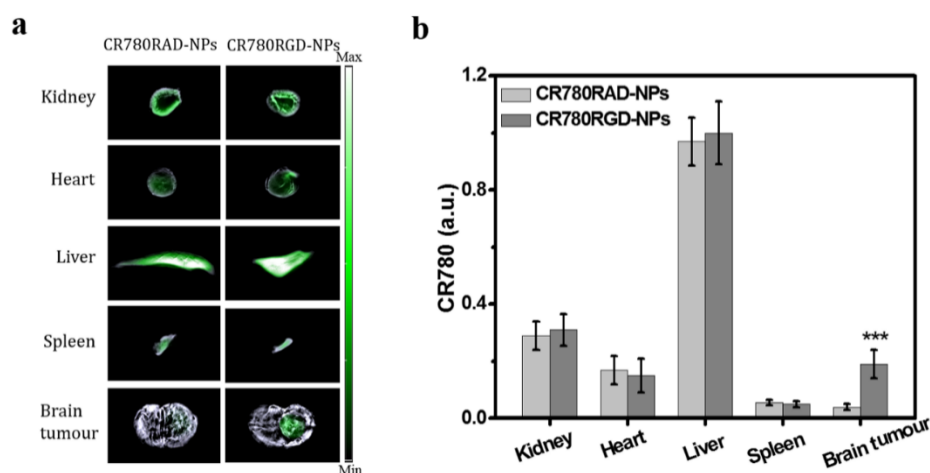
Figure 3.19. The biodistribution of CR780RAD-NPs and CR780RGD-NPs in major organs at 24 h after intravenous injection into mice bearing U87MG glioblastoma cells. Animals were injected with 100 µL of CR780RAD-NPs (1 mM) or CR780RGD-NPs (1 mM). **(a)** Optoacoustic coronal plane images of major organs. **(b)** Optoacoustic signal intensity of major organs. (***p < 0.001)

3.3.7 *In vivo* biosafety of CR780RGD-NPs

To evaluate the *in vivo* safety of CR780RGD-NPs, healthy C57BL/6 mice were injected with 100 µL of CR780RGD-NPs (1 mM). The mice were sacrificed on days 1, 7, and 14 post-injection, and blood samples were collected for organ function examination (**Figure 3.20a, b**). The blood chemistry parameters and hematology analysis results demonstrated no significant difference between mice treated with CR780RGD-NPs or PBS, and no signs of acute systemic toxicity were observed. The H&E staining and histology analysis of major organs (**Figure 3.20c**) confirmed no noticeable nanotoxicity or damage to key organs after intravenous administration of CR780RGD-NPs. None of the treated animals died during the observation period (14 days). These results suggest that CR780RGD-NPs are well tolerated.
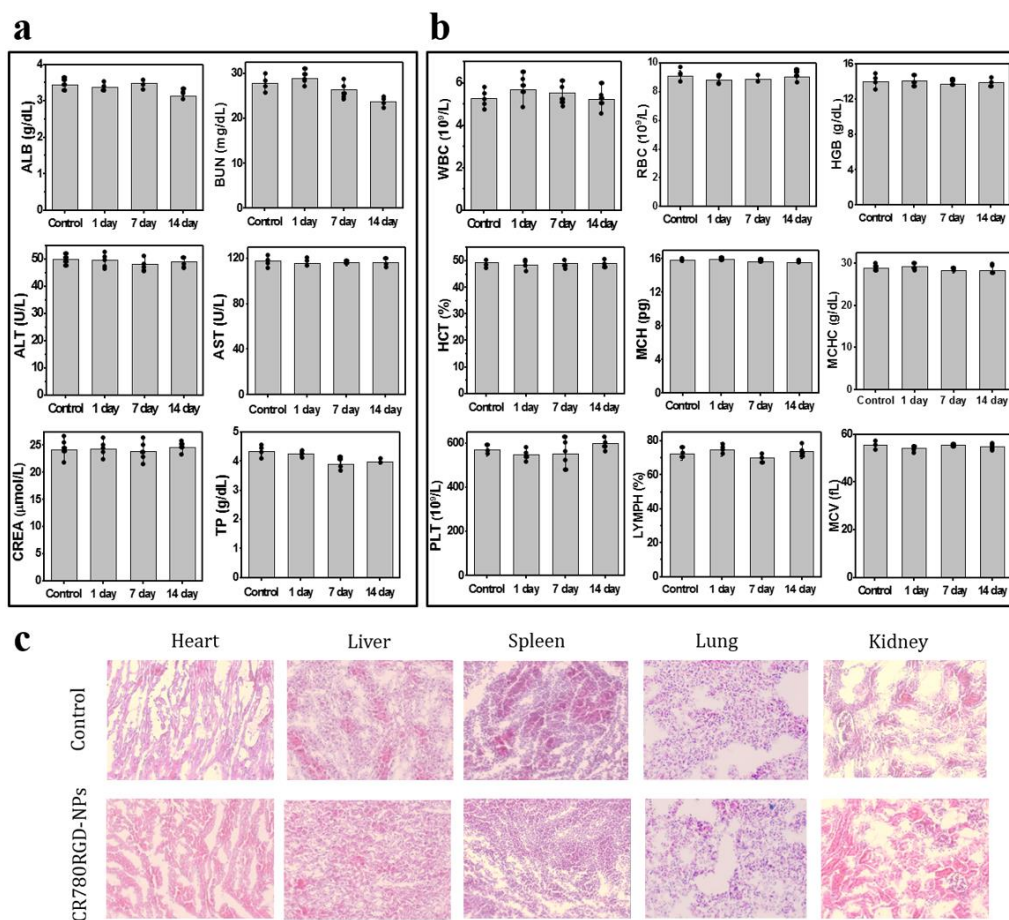
Figure 3.21. Biosafety study of CR780RGD-NPs. Blood and major organs were sampled after healthy C57BL/6 mice were injected with 100 μL of CR780RGD-NPs (1mM) or PBS (control). (a) Blood biochemistry. (b) Hematology. (c) Hematoxylin-eosin staining of vital organs (20×magnification).

3.4 Discussion

Here we describe c(RGDyC) peptide-modified CR780 nanoparticles as highly efficient optoacoustic agents for targeted brain tumor imaging. We compared the photophysical properties of CR780RGD-NPs with FDA-approved ICG, and found that CR780RGD-NPs have an improved OGE and photostability, resulting in strong, sustained optoacoustic signals. Due to the ultrasmall size and tumor-targeting ability,

CR780RGD-NPs could efficiently reach the deep-seated brain tumor to generate strong optoacoustic contrast from the targeted tumor region. Importantly, systemically injected CR780RGD-NPs show no signs of toxic side effects.

Ideal optoacoustic contrast agents should possess low quantum yield, high molar-extinction coefficient, high OGE, narrow NIR absorption peak, and excellent photostability as well as tumor specificity and low toxicity.[16] We found that the photostability of CR780 is very high compared to ICG under similar laser irradiation conditions, which allowed us to accurately detect the signal and quantify agent from various depths, both *in vitro* and *in vivo,* for at least 24 h. The OGE of CR780RGD-NPs is 1.8-8.5 times higher than that of the well-established NIR dyes ICG, IR780 iodide, IR820, IRDye800CW. Results clearly indicate that CR780RGD-NPs are suitable for *in vivo* optoacoustic imaging.

CR780RGD-NPs exhibit high optoacoustic signals and a high SNR, making them suitable for deep tissue imaging. Optoacoustic imaging of brain is challenging mainly due to strong optical scattering by the skull and brain tissue, which severely limits the optical fluence. Furthermore, the acoustic signals are attenuated in transit through the skull. However, CR780RGD-NPs showed a strong optoacoustic signal at a low dose and a 5 mm depth in brain tissue.

Deep-seated brain tumors are usually hard to reach because of the protection by the BBB, which normally substantially limits the brain uptake of externally administered compounds.[108] However, under disease conditions such as in cancer, the BBB is disrupted and the permeability increases, which allows nanoparticles of certain dimensions to pass through and reach different areas in the brain.[86] Nanoparticles above 100 nm in size exhibit poor brain tumor extravasation, whereas nanoparticles below 5 nm undergo rapid clearance via the kidney.[109, 110] Particles in the size range of 20-70 nm are considered optimal for brain tumor targeting, with other factors such as shape, charge, and targeting activity also playing important roles.[84] We observed

enhanced uptake and retention of CR780RGD-NPs (25 nm size) in the brain tumor which, when combined with active targeting via integrin $\alpha_v\beta_3$ receptors on the tumor surface, ensured a sustained optoacoustic signal from CR780 from within the tumor. The optoacoustic and fluorescence-based cryo-images of isolated organs clearly indicated the accumulation of CR780RGD-NPs in the brain tumor, whereas most of the particles that did not target the tumor were safely cleared out by the liver and kidney.

The strong optoacoustic signal due to CR780RGD-NPs for at least 24 h clearly indicates the prolonged circulation time and retention of nanoparticles in the body. It was therefore important to test the biosafety and biocompatibility of the nanoparticles, and we tested the potentially toxic effects due to CR780RGD-NPs treatment both *in vitro* and *in vivo*. Treatment of different concentrations of nanoparticles in U87MG cells showed no effect on cell viability. We next tested the acute toxicity of systemically injected CR780RGD-NPs in normal C57BL/6 mice for up to 14 days. The results of organ function tests and hematology clearly indicated that CR780RGD-NPs were well tolerated, and no signs of changes in blood parameters were observed throughout the observation period. Blood tests and histopathological examination suggested normal function of vital organs (heart, liver, spleen, and kidney), further confirming that the nanoparticles were well tolerated.

The multispectral optoacoustic technique MSOT allows simultaneous imaging of multiple endogenous chromophores in the brain for assessment of brain structure and function.[8, 101, 111] Here we extended the brain imaging abilities of MSOT by using an exogenous contrast agent that can target brain tumors and generate a strong optoacoustic signal even deep below the brain surface. The unique photophysical properties of ultrasmall CR780RGD-NPs may play a crucial role in the early diagnosis of brain tumors, identifying the margins of tumor tissue and therapy response. This is crucial for the application of MSOT and other optoacoustic techniques for diagnosis and intraoperative procedures, as well as for therapy decision-making. Our work

justifies further efficacy and safety studies in large animals as a prelude to human trials.

In summary, our results show the powerful capabilities of MSOT and the developed CR780RGD-NPs for targeted optoacoustic imaging of brain tumors. The ultrasmall size of the nanoparticles ensures efficient BBB penetration, while their tumor-targeting ability, high OGE, and photostability ensure enhanced optoacoustic contrast. Biocompatible CR780RGD-NPs may be a smart diagnostic tool for integrin-expressing, deep-seated tumors and may be able to selectively deliver drugs to such tumors. This sets the foundation to explore the theranostic potential of CR780RGD-NPs as imaging agents and photothermal therapeutics against brain tumors and other cancers in the future.

4 880nm-absorbed croconaine nanoparticles for efficient optoacoustic imaging of deep tumor and photothermal therapy

Content in this chapter is based on (at parts verbatim) my planned manuscript.

Nian Liu, Patrick O'Connor, Vipul Gujrati,* Pia Anzenhofer, Jaber Malekzadeh-Najafabadi, Karin Kleigrewe, Michael Sattler, Oliver Plettenburg, Vasilis Ntziachristos*. 880nm-absorbed croconaine nanoparticles for efficient optoacoustic imaging of deep tumor and photothermal therapy. (In preparation)

Author contributions: Nian Liu identified the CR880 dye, developed CR880-NPs, carried nanoparticle characterization (DLS, zeta potential, photophysical properties, optoacoustic signals, photostability, photothermal performance) and cell experiments (MTT assay, AM/PI, cell treatment), whereas *in vivo* experiments (optoacoustic imaging, photothermal therapy, and biosafety) were assisted by Dr. Vipul Gujrati and technician Pia Anzenhofer. Dr. Patrick O'Connor synthesized and characterized the CR880 dye. Dr. Vipul Gujrati along with Nian Liu designed the *in vitro* and *in vivo* experiments and analyzed the data. Pia Anzenhofer assisted with animal experiments and maintenance. Jaber Malekzadeh-Najafabadi helped for optoacoustic phantoms experiments. Dr. Karin Kleigrewe did the MALDI-TOF characterization. Prof. Oliver Plettenburg supervised dye synthesis, characterization, and provided intellectual input, and Prof. Michael Sattler and Prof. Vasilis Ntziachristos helped interpret the results, provided significant intellectual input, and supervised the research. All authors contributed to writing the paper.

4.1 Motivation

NIR light-triggered cancer phototherapy which utilizes fluorophores that undergo photoconversion from ground to excited states are considered a promising therapeutic modality owing to their favorable characteristics such as noninvasiveness, spatiotemporal controllability, negligible drug resistance, and minimized systemic toxicity.[112-114] Such light-activated therapeutics can be categorized according to their mechanism of action, for example, photothermal therapy (PTT), which employ photothermal agents to produce thermal effect through the nonradiative transition.[66, 69] Meanwhile, under the laser irradiation, the generated thermoelastic expansion from tumor areas can produce subsequent ultrasonic signals, which can be detected by optoacoustic imaging.[7, 67] Therefore, the photothermal agents which have both excellent optoacoustic and photothermal performance in the NIR region are sought after for *in vivo* cancer theranostics.

Recently, various NIR light-absorbing organic agents have been developed for optoacoustic imaging-guided photothermal therapy, such as cyanine, squaraine, BODIPY, and tetrapyrrole dyes or derived nanoparticles.[26, 69] However, these structural classes of dyes have inherent problems associated with difficult multistep synthesis, low molar extinction coefficients, high quantum yield, and poor photostability, contributing to weak optoacoustic signals and little generated heat.[26] Croconaine dyes have been shown to overcome the mentioned problems with a strong NIR absorption coefficient and excellent photostability.[46] Four croconaine structures [51-53, 70] have been reported as nanoformulations with stable NIR optical properties for biomedical application. Most of the reported croconaine exhibit absorption maxima at around 800 nm, a wavelength at which light scattering is still high, limiting deep tissue imaging.[115] There is therefore a need to develop a nanoformulated croconaine optimized for use at a longer wavelengths.

Inspired by the above considerations, we developed an 880 nm-absorbed croconaine nanoformulation as an improved platform for efficient optoacoustic imaging of deep tumors and PPT. The selected croconaine dye (CR880) was previously reported by Tang et al. for use in solar energy harvesting and water evaporation.[45] Structurally, CR880 possesses two electron-donating tetraphenylethylene (TPE) units symmetrically conjugated to a thiophene-substituted croconaine backbone. Interestingly CR880 has conflicting evidence favoring both H- and J-aggregation, however irrespective of the type of solid-phase packing the dye possesses, the dye does not blue shift upon condensing to the solid phase. Tang et al gave an electronic rationale for the dyes properties involving a di-radical electronic configuration, and strong π-π stacking of the coplanar structure, CR880 displays a NIR absorbance in the desired range of 880nm. Meanwhile, the extremely low energy-gap enables to enhance the nonradiative decay for boosting more heat. Therefore, after encapsulated CR880 into DSPE-PEG2000, the formulated CR880-NPs exhibited superior optoacoustic generation efficiency and photostability at 880 nm, which not only efficiently weaken the light scattering for deep tissue penetration but also produce a strong optoacoustic signal to be detected from deep tissue (breast tumor, brain tumor and colon tumor). Besides, 58.14% of photothermal conversion efficiency from CR880-NPs is much higher than most of the reported PTT agents, which are sufficient for cancer PTT with lower laser energy *in vitro* and *in vivo*. In addition, CR880-NPs have no biosafety concerns. Overall, CR880-derived nanoparticles can be able to use as a high-efficient photo-theranostic agent for deep tumors' diagnosis and therapy.

4.2 Experimental section

4.2.1 Materials

All the chemical reagents were purchased from abcr GmbH (Germany). DSPE-

PEG2000 was obtained from Nanocs Inc. (USA). Indocyanine green (ICG) and MTT were purchased from Sigma-Aldrich (Germany).

4.2.2 Synthesis of CR880

CR880 was synthesized according to a known two-step literature procedure (**Scheme 4.1**).[45] Firstly, *in situ* boronation of bis(4-bromophenyl)amine with bis(pinacolato)diboron was followed by Suzuki coupling with the appropriate vinyl bromide in a one-pot procedure giving secondary amine in high yield. The sterically hindered amine then underwent Buchwald Hartwig coupling under forcing conditions giving the 2-amino thiophene which was then coupled with croconic acid under standard conditions to afford the desired dye in low yield 400 MHz ^{1}H NMR and MALDI-TOF were used for further characterization analysis of the resulting product. ^{1}H NMR (400 MHz, DMSO-d_6) δ: 8.85–8.69 (m, 2H), 7.16–7.02 (m, 76H), 6.54 (m, 2H). MALDI: m/z = 1625.826 [M + H]$^+$ (**Figure 4.1**).
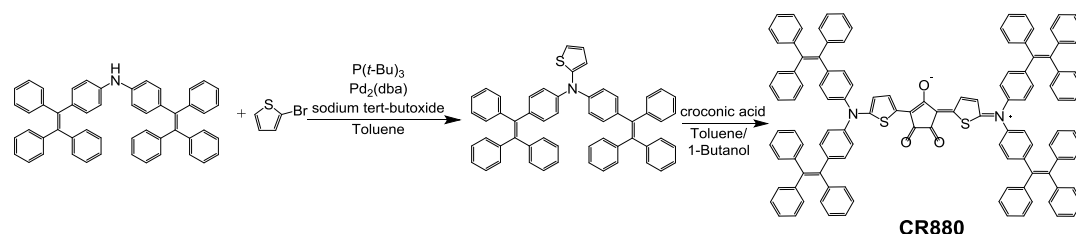
Scheme 4.1. Synthetic methods of CR880.
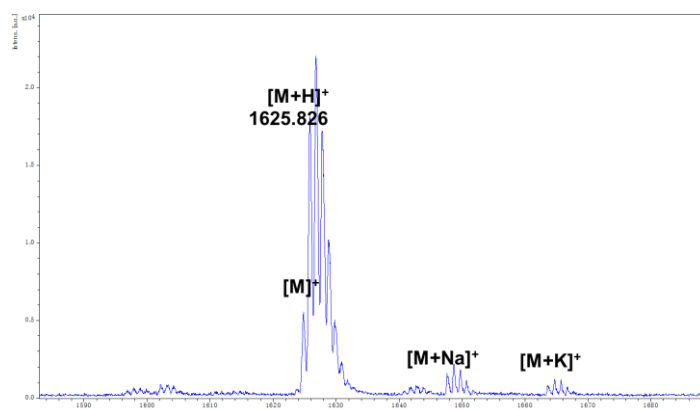
Figure 4.1. MALDI-TOF mass spectrum of CR880.

4.2.3 Preparation of CR880-NPs

CR880 (1 mg) and DSPE-PEG2000 (2 mg) were first dissolved well into tetrahydrofuran (1mL). Then the mixed solution was quickly injected into 9 mL deionized water. Then a microtip probe sonicator (12 W) was employed to sonicate the solution for 2 min, followed by removing the remaining tetrahydrofuran with a rotary evaporator. The final CR880-NPs were filtered by a 200 nm filter and then concentrated with a centrifugal-filter (MWCO = 100 kDa) for further use.

4.2.4 Characterization

^{1}H NMR spectra were measured on a Bruker spectrometer at 400 MHz. HRMS were recorded with a MALDI UltrafleXtreme (Bruker) using dihydroxybenzoic acid as the matrix. The particle dimensions of CR880-NPs were assessed by transmission electron microscopy (TEM) using a JEM 100-CX (JEOL GmbH, Germany) and dynamic light scattering (DLS) (Malvern Zetasizer). Absorption spectra were recorded with a UV-1800 spectrometer (Shimadzu, Japan). Optoacoustic spectra of samples were measured using an MSOT inVision 256-TF and then normalize with India ink and Brilliant Black BN.[72] The optoacoustic generation efficiency (OGE) of samples was calculated by the slope of the normalized optoacoustic intensities and absorbance of samples.[72] The photostability of samples was monitored by an MSOT inVision 256-TF with pulsed laser irradiation for 60 min (fluence 10 mJ/cm^2).

4.2.5 *In vitro* penetration depth estimation

Tissue-mimicking cylindrical phantoms with different radii were made by using the mixture of intralipid (2 mL), agar (2 g), India ink solution (98 mL, absorbance 0.15 at 780 nm).[96, 97] Then tubing containing ICG (0.5 at 800 nm), CR780-NPs (0.5 at 800 nm), and CR880-NPs (0.5 at 880 nm) was inserted into the ink-agar phantoms with different thicknesses, separately. Optoacoustic phantom images were measured using

MSOT. The image contrast was calculated by $(OA_{sig}-OA_{bg})/ (OA_{sig}+OA_{bg})$, where OA_{sig} and OA_{bg} are the mean optoacoustic intensities of sample and agar phantom at their specific wavelengths.[28]

4.2.6 *In vivo* optoacoustic imaging of various tumor models

4T1 tumor models were prepared using nude mice (6 weeks) by implanting 4T1 cells (1×10^6, 30 μL) on the back of the mice. Upon reaching a tumor volume of 100 mm^3, *in vivo* optoacoustic imaging was carried out. The orthotopic tumor models were made using 3 nod scid shorn mice (6 weeks) by slowly implanting U87MG cells (4×10^5, 3 μL) into the mouse striatum (bregma + 1.0 mm, left lateral 2.0 mm and depth 3.0 mm). The brain tumor models were ready after four weeks' implantation.[101] The orthotopic colon tumor model was prepared with 3 normal nude mice (6 weeks). After HCT116 cells (3×10^6, 100μL) were intraperitoneally injected for two weeks, the tumor model was ready for MSOT imaging. All procedures involving animal experiments were approved by the Animal Care and Handling Office of Helmholtz Zentrum München and Government of Upper Bavaria.

Each tumor-bearing mouse per treatment was i.v. injected with CR880-NPs (100 μL, 0.3 mM). *In vivo* optoacoustic images were taken at different time points before and after injection using an MSOT inVision 256-TF. The averaged optoacoustic signals of tumor regions were measured using ViewMSOT 4.0 software (iThera Medical, Munich).

4.2.7 *In vitro* photothermal effect of CR880-NPs

The photothermal conversion abilities of CR880-NPs were assessed by recording their temperature changes at different concentrations of CR880-NPs upon exposure to a 885 nm CW laser at different laser power using an IR thermal camera. The photothermal conversion efficiency (PCE) of CR880-NPs was calculated by the

equation $\eta=[(hS(T-T_{surr})-Q_{Dis}]/I(1-10^{-A885})$, Here the absorbance (A885) of CR760RGD-NPs was 0.18 at 885 nm and the power density (I) of 885 nm CW laser was 0.8 W/cm^2.[73]

4T1 cells were sub-cultured in a 96-well plate overnight (1×10^4 cells/well). Then the cells were first treated with PBS or different concentrations of CR880-NPs for 4 h, followed by laser irradiation (885 nm CW laser) for 5 min. Then the cells were kept culturing for another 24 h to calculate the relative cell viabilities by MTT assay. Live/dead cell assays were visualized the PTT effect from the cellular level. The treated cells were co-stained with Calcein-AM and EthD1 for 30 min and then were imaged using Leica DMI3000 B Inverted Microscope (Wetzlar, Germany).

4.2.8 *In vivo* PTT of 4T1 tumor-bearing mice

The 4T1 tumor-bearing mice with around 100 mm^3 tumor volume were randomly divided into four groups (n =5 per group) and subjected to 4 different treatments including: PBS, PBS + laser, CR880-NPs, and CR880-NPs + laser, separately (laser power: 0.8 W/cm^2 885nm CW laser for 10 min, CR880-NPs concentration: 100 μL, 0.3 mM). An infrared thermal camera was used to record the temperature changes of tumor areas from each group. The tumor volume and body weight were measured until 8 days, then the mice were sacrificed and the tumors from each group were isolated for H&E staining.

4.2.9 Blood hematology and biochemistry analyses

C57BL/6 mice were randomly divided into 3 groups (n=5 per group). The control group was i.v. injected with 100 μL of PBS and collected the blood on day 14. The other 2 groups were i.v. injected with 100 μL of CR880-NPs (0.3 mM) and collated the blood on days 7, and 14, respectively. Hitachi 917 Clinical Chemistry Analyzer (Roche, Germany) was used to test the detailed parameters of blood hematology and

biochemistry. The vital organs were isolated for H&E staining.

4.3 Results

4.3.1 Synthesis and characterization of CR880

CR880 was prepared according to the reported method by condensation of two electron-donating segments with the electron-withdrawing croconic acid core to give the "D-A-D" dye.[45] The chemical structure of CR880 was confirmed by ^{1}H NMR spectroscopy and MALDI-TOF mass spectrometry. CR880 has moderate solubility in common organic solvents such as DMSO, tetrahydrofuran, chloroform, and ethanol (**Figure 4.2**). Remarkably, CR880 shows a strong absorption peak at 880 nm with a significantly higher molar absorption coefficient in ethanol which is well consistent of as-reported croconaine dyes. Furthermore, the OGE of CR880 and ICG were measured in 10% FBS. CR880 exhibits an excellent OGE which is 2.16 times higher than that of ICG. The reported HOMO-LUMO energy gap was 0.75 eV, [45] the lower value indicates the strong charge-transfer, which proved the red-shifted absorption of CR880.
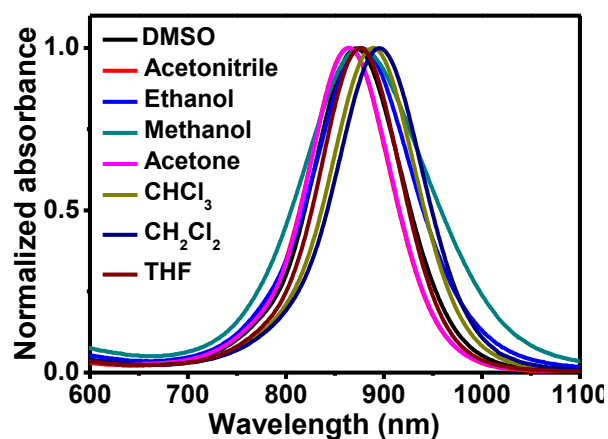
Figure 4.2 Normalized optical spectra of CR880 in different organic solvents.

4.3.2 Synthesis and characterization of CR880-NPs

To apply hydrophobic CR880 for *in vivo* biomedical application, water-soluble

CR880-NPs were synthesized by the nanoprecipitation method with DSPE-PEG2000. The morphology and size of CR880-NPs were characterized by TEM and DLS. **Figure 4.3a, b** show that the CR880-NPs had a spherical morphology with an average diameter of around 45 nm. **Figure 4.3c, d** shows the optical and optoacoustic spectrum of CR880-NPs with the narrow and intense peaks at 880 nm. Next, **Figure 4.3e** demonstrated that the OGE of CR880-NPs was also 2.16 times higher than ICG, which indicates that CR880-NPs can be an efficient optoacoustic agent. Furthermore, the photostability of CR880-NPs was assessed by continuously irradiating with pulsed laser for 60 min and comparing the changes in optoacoustic signal (indicator for photostability) against ICG. **Figure 4.3f** shows that CR880-NPs are photostable, while ICG was completely bleached at the same irradiation conditions. Then CR880-NPs were cultured at PBS buffer until 14 days, there were little changes from nanoparticles' size and optical intensities (**Figure 4.4**). These results suggest that the water-soluble CR880-NPs have excellent optical properties which are sufficient for *in vivo* optoacoustic imaging.
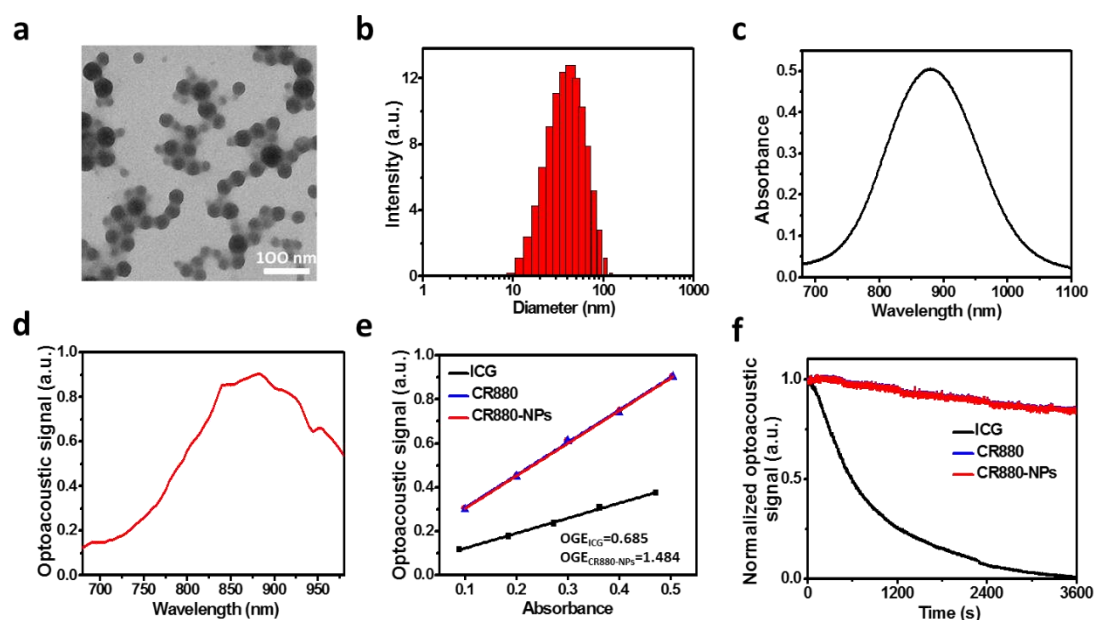
Figure 4.3 (a, b) TEM image and DLS profile of CR880-NPs. **(c, d)** Optical spectrum and optoacoustic spectrum of CR880-NPs. **(e)** Optoacoustic signals of ICG, CR880,

CR880-NPs at different concentrations. (**f**) Optoacoustic signal degradation of ICG, CR880, and CR880-NPs after pulsed laser irradiation (fluence 10 mJ/cm^2, 60 min).
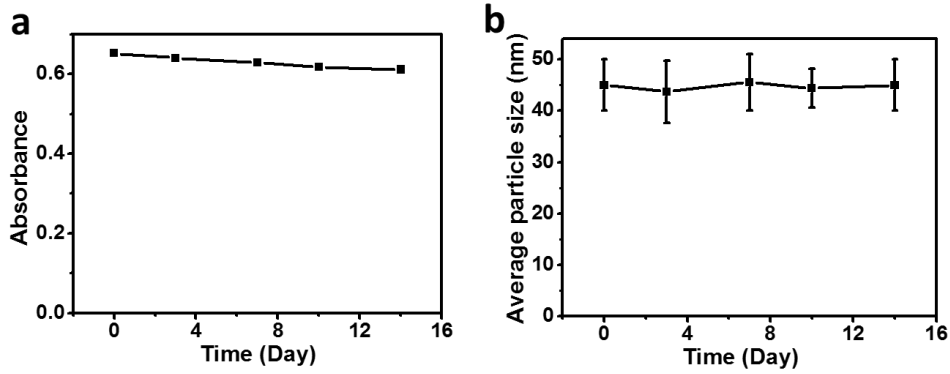
Figure 4.4. (**a**) Optical stability and (**b**) size stability of CR880-NPs during 14 days.

4.3.3 Optoacoustic imaging at different depths with CR880-NPs *in vitro*

To check the capacity of CR880-NPs for deep tissue imaging, we used different thicknesses of tissue-mimicking phantoms to evaluate the optoacoustic signals from deep tissue. Various cylindrical agar phantoms with different radii were prepared by mixed with India ink to keep the absorbance to be 0.15 at 780 nm. Then the tubing containing the samples (ICG, CR780-NPs, or CR880-NPs) with 0.5 absorbance were inserted into the center. **Figure 4.5a** shows that the optoacoustic images captured from tissue-mimicking phantoms with increasing thickness, where the optoacoustic signal of samples inserted in the tubing was detected from the center. We can see that agar phantoms at 880 nm have much lower noise signals compare to 780 nm and 800 nm, while the phantom images of CR880-NPs at different thicknesses also exhibited higher optoacoustic intensities than ICG and CR780-NPs. The reconstructed optoacoustic spectra of these three at 9 mm of thickness clearly showed a significant difference from the optoacoustic intensities at their specific absorption peaks (**Figure 4.5b**). The concept of image contrast was used to reflect the imaging performance and depth. CR880-NPs showed a much higher image contrast than the other two, even in the depth of 9 mm (**Figure 4.5c**). These results confirm that the superior ability of CR880-NPs

for optoacoustic imaging of deep tissues.
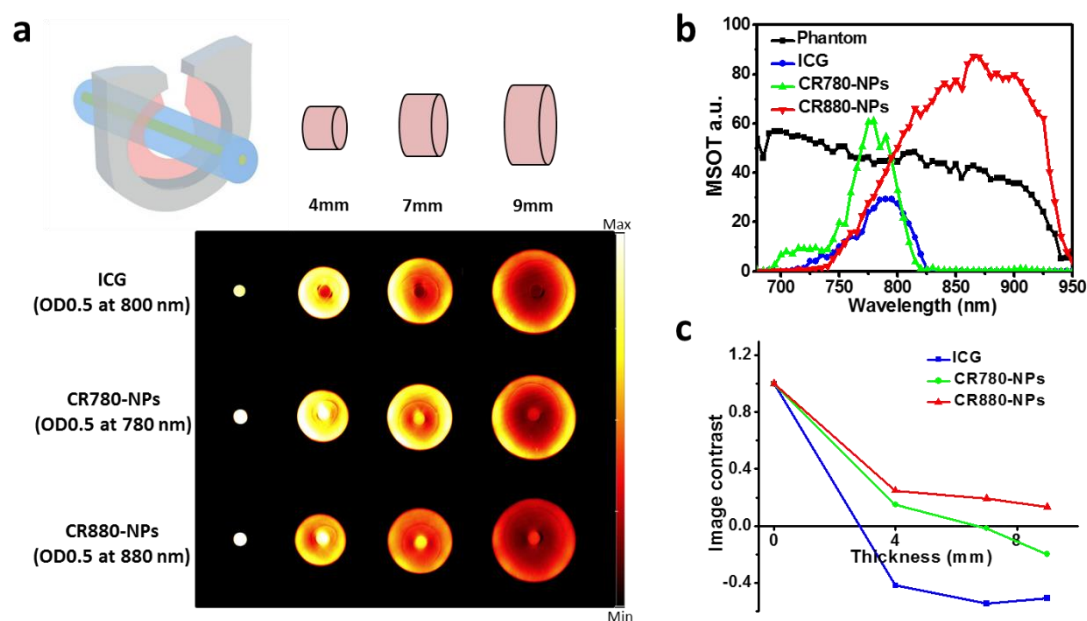
Figure 4.5 (a) Optoacoustic imaging of tissue-mimicking phantoms of increasing thickness containing different samples with the same absorption intensity (0.5) at their absorption peak. Phantom absorbance, 0.15 at 780 nm. The optoacoustic images were acquired from their absorption peaks, individually. (**b**) Optoacoustic signals of ICG, CR780-NPs, and CR880-NPs in the 9 mm phantom. (**c**) Image contrast of ICG, CR780-NPs, and CR880-NPs from phantoms of different thicknesses.

4.3.5 *In vivo* optoacoustic imaging with CR880-NPs

Owing to the excellent optoacoustic image contrast on phantoms and the suitable nanoformulation, CR880-NPs were studied on different tumor models to validate the capability of deep tissue imaging. CR8880-NPs were first studied in 4T1 subcutaneous tumor model. **Figure 4.6a** shows representative unmixing optoacoustic images of 4T1 tumor-bearing mice, acquired using MSOT system at different time points (0h, 1h, 4h, 8h, 12h, and 24h). The yellow colors were the unmixed CR880-NPs signal. As observed from 1 h MSOT image, CR880-NPs due to their small nano-size, could start to accumulate in the tumor due to the enhanced permeability and retention (EPR) effect.

CR880-NPs showed maximum tumor accumulation 12 hours post-injection. Extending the delay time between injection and optoacoustic measurement to 24h resulted in a decreased signal, indicating that some of CR880-NPs had undergone systemic clearance from tumor vasculature. **Figure 4.6b** shows that the signal intensities of the tumor region at 4 h and 12 h relative to 0 h were increased by a factor of 6.2 and 10.15 folds respectively. The data indicates that PTT is optimally conducted with a post-injection delay of 4-12h.

To ensure whether CR880-NPs could be used for *in vivo* deep tumor imaging, we made another two types of orthotopic tumors (brain tumor and colon tumor). **Figure 4.6c** shows representative optoacoustic images of orthotopic brain tumors and colon tumors at 0 h and 24 h. As observed in MSOT images of brain tumors, it is clear to see that CR880-NPs can efficiently target to brain tumor due to the suitable size distribution, where the CR880-NPs' signal can be detected from the depth of ~5 mm. The presence of the brain tumor was validated by cryo-slicing and H&E staining (**Figure 4.6d,e**). Next, the MSOT imaging for colon cancer models showed the strong optoacoutic signals from the enterocoelia wall, where 15 mm width of tumor can be visualized directly. Besides, the colon tumors from a depth over 6 mm were also detected because of the presence of CR880-NPs. The cryo-slicing and H&E staining also confirmed the existence of colon tumors. Therefore, CR880-NPs can generate efficient optoacoustic signals from deep tumors using the commercially available MSOT system.

After 24 h postinjection of CR880-NPs, the major organ (kidney, liver, spleen, heart) and tumors from each tumor model were isolated to analyze the *in vivo* biodistribution using MSOT imaging. **Figure 4.7a,b** showed the optoacoustic coronal plane images corresponding to signal intensities in major organs and the tumor. These data indicated that most of CR880-NPs accumulated in the liver, spleen, and tumor with a small degree of accumulation in the kidney and heart.
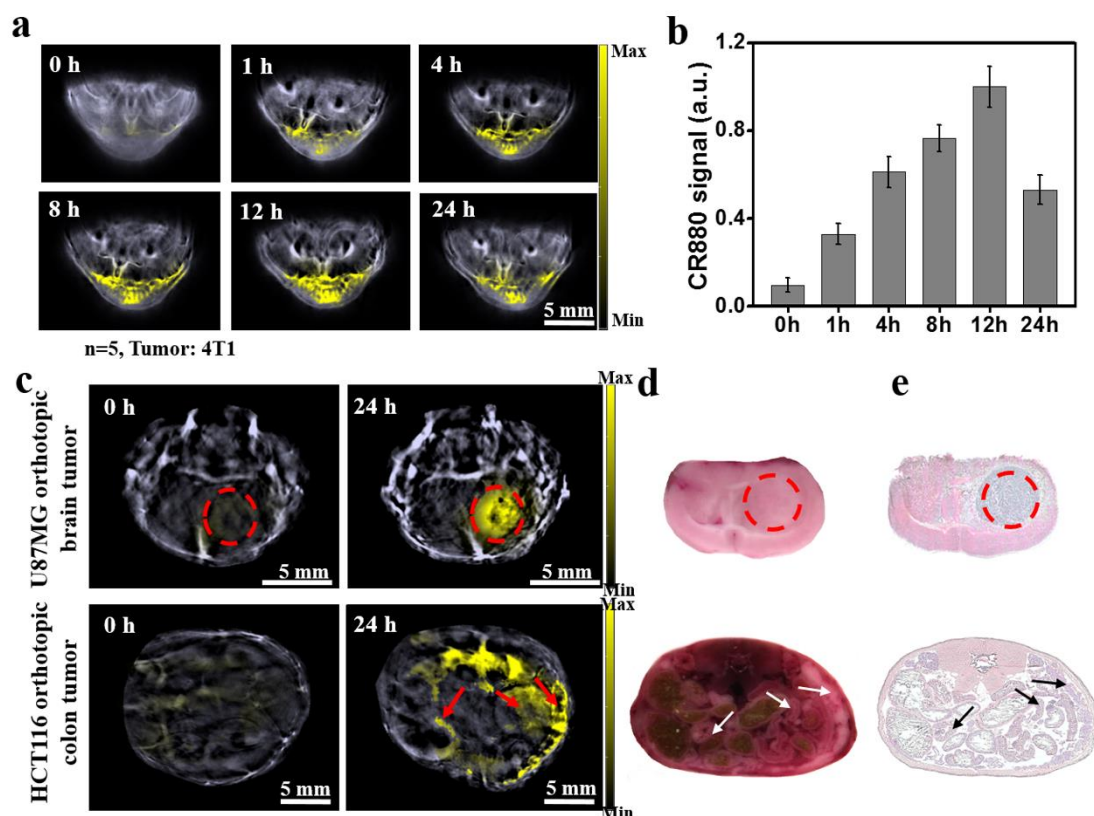
Figure 4.6 (**a**) Representative unmixed MSOT images of 4T1 subcutaneous tumor models i.v. injected with 100 µL of CR880-NPs (0.3 mM), (n=5). Unmixed CR880 signal is shown by the hot color in the tumor region. (**b**) Quantification of panel (a): CR880-NPs concentrations in the tumor region measured over time. (**c**) Representative unmixed image of U87MG bearing orthotopic glioblastoma and HCT116 orthotopic colon tumor i.v. injected with 100 µL of CR880-NPs (0.3 mM). (n=3). (**d, e**) Bright fields and HE staining of brain tumor slices and colon tumor slices.
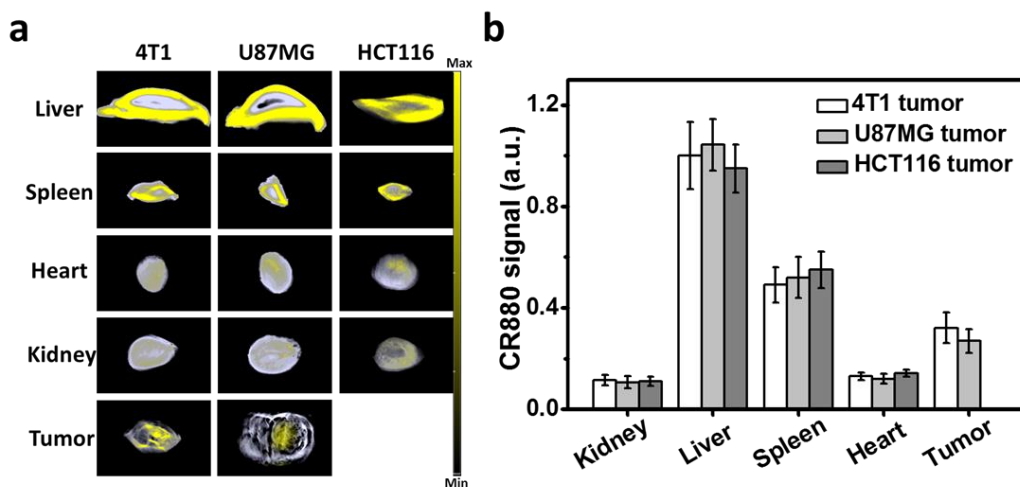
Figure 4.7 (a) Optoacoustic coronal plane images of major organs at 24 h after intravenous injection of CR880-NPs (0.3 mM, 100 μL) into different tumor models. **(b)** Optoacoustic signal intensities of major organs.

4.3.4 *In vitro* photothermal effect of CR880-NPs

The intense NIR absorbance of CR880-NPs suggested that CR880-NPs could be an excellent photo-absorbing agent for PTT. To evaluate the PTT effect of CR880-NPs, differing concentrations of CR880-NPs at 0, 1.25, 2.5, 5, or 10 μM were irradiated by a 885 nm CW laser at 0.8 W/cm^2 of power density. **Figure 4.8a** shows that the temperature increase of CR880-NPs was concentration-dependent. Under the same laser irradiation condition, 10 μM of CR880-NPs solution have a 36.9 ℃ change, while DI water only increased for 5.2 ℃. It is reported that the condition of 42–50 ℃ for 5 min can lead to killing cancer cells.[65] The effect of laser power intensity (0.2, 0.4, 0.6, or 0.8 W/cm^2) on the temperature change of CR880-NPs (10 μM) was explored next. **Figure 4.8b** shows a clear laser power intensity dependence on the temperature increase. **Figure 4.8c** shows that CR880-NPs exhibited a 58.21% photothermal conversion efficiency, though it depends on the concentration and molar absorptivity of samples.[65]

To further evaluate the PTT potential of CR880-NPs on cancerous cell lines, a

standard MTT assay was employed to assess the photothermal effect of CR880-NPs on 4T1 cells by incubating for 4 h. CR880-NPs showed negligible cytotoxicity at a concentration of up to 10 μM. However, upon 5 min of irradiation with a 885 nm CW laser at 0.8 W/cm^2, the viability of cells decreased in proportion to the concentration of CR880-NPs (**Figure 4.8d**). Specifically, more than 96% of cells were killed at CR880-NPs concentration of 10 μM under 0.8 W/cm^2 laser irradiation. Furthermore, different laser powers were also used to assess the photothermal cytotoxicity of the cells incubated with 10 μM CR880-NPs (**Figure 4.8e**). As expected, cell viability decreased obviously with the increase of laser power. Besides, the PTT capability of CR880-NPs on the cells can be visualized by live/dead cells assays. 4T1 cells were done with different treatments for 4 h, and then co-stained with calcein-AM and EthD-1. **Figure 4.8f** demonstrated the significant difference in cellular cytotoxicity among the 4 groups, which are in agreement with MTT results**.**
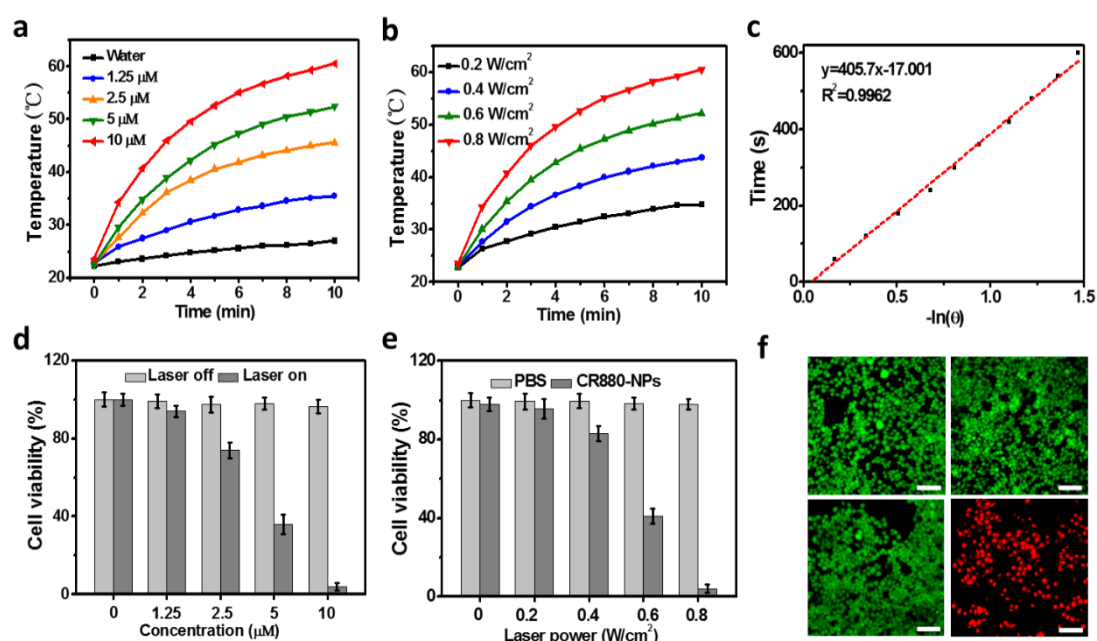
**Figure 4.8 (a)** Temperature change curves of CR880-NPs at different concentrations upon exposure to a 885 nm CW laser (0.8 W/cm^2). **(b)** Temperature change curves of CR880-NPs (10 μM) upon exposure to a 885 nm CW laser at different power densities. **(c)** Linear correlation of the cooling times of CR880-NPs versus negative logarithm of

temperatures. **(d)** Relative viabilities of 4T1 cells after treatment with CR880-NPs (10 µM) with (or without) 885 nm CW laser irradiation at 0.8 W/cm^2 for 5 min. **(e)** Relative viabilities of 4T1 cells after treatment with 10 µM CR880-NPs (or PBS) under 885 nm CW laser irradiation at different power densities. **(f)** Fluorescence images of the treated 4T1 cells co-stained with calcein AM (green color, live cells) and EthD1 (red color, dead cells). Scale bars, 100 µm.

4.3.6 *In vivo* **PTT of 4T1 tumor-bearing mice**

To evaluate *in vivo* tumor PTT using CR880-NPs, 4T1 tumor-bearing mice were randomly divided into four groups including: PBS, PBS + laser, CR880-NPs, and CR880-NPs + laser. We established the 12 h post-injection as the optimum laser irradiation time, according to *in vivo* optoacoustic imaging of 4T1 tumor model with CR880-NPs. The temperature changes of tumor areas from different groups were recorded until 10 min by a thermal camera. **Figure 4.9a, b** shows that the temperature of the tumor region i.v. injected with CR880-NPs reached a temperature of 51.7 ℃, which is sufficient to achieve cell killing. However, mice treated with PBS showed negligible temperature changes under the same irradiation condition.

After the different treatments for each group, the tumor volumes and body weights of the four groups were continuously measured for another 8 days. As shown in **Figure 4.9c,d**, the tumors treated with CR880-NPs + laser displayed complete tumor elimination, while the tumor from the other 3 control groups showed persistently high growth rates. These results suggested that CR880-NPs can be induced to generate significant heat for eliminating cancerous cells. The body weights from these four groups did not show significant changes during the 8 days (**Figure 4.9e**). After 8 days, the residual tumor tissues and major organs from each group were resected and done with the pathological examination by H&E staining. The CR880-NPs + laser treated group showed cell shrinkage, separation, and fragmentized nuclei, which suggested the

well recovery (**Figure 4.9f**). All these results suggested that C880-NPs can be an efficient PTT agent for cancer treatment.
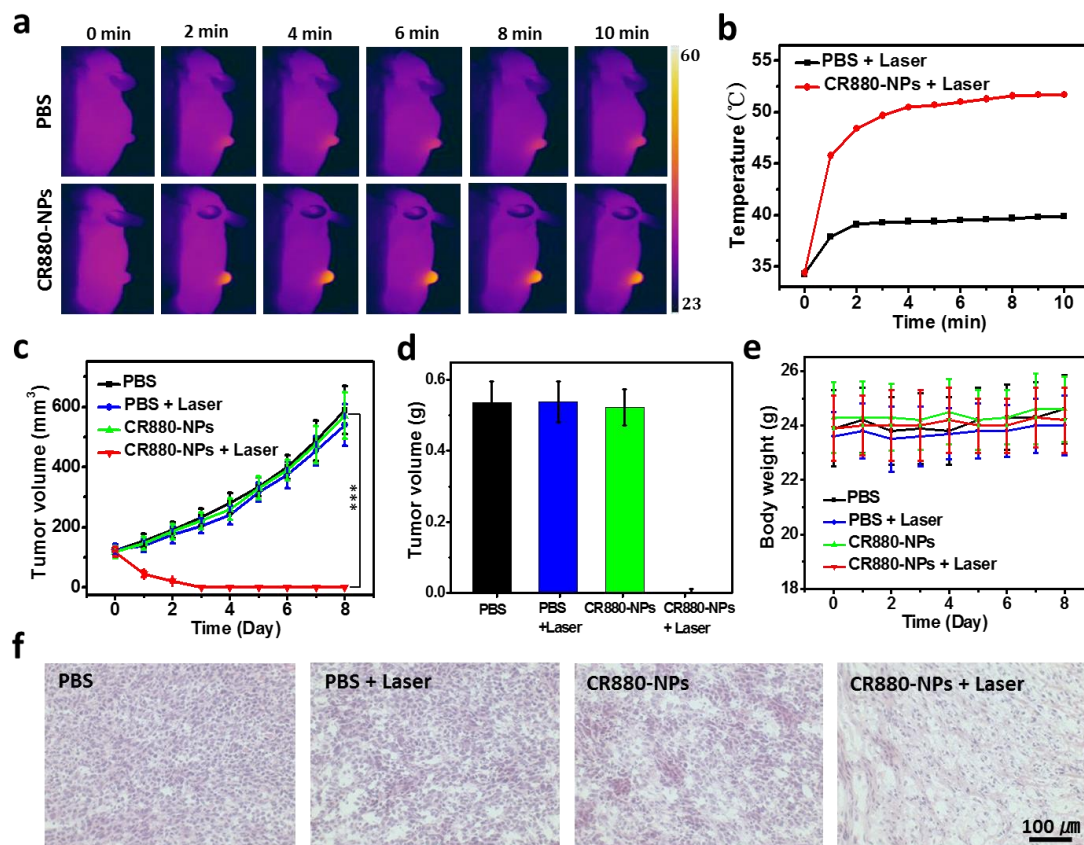
Figure 4.9 (**a**) Thermal images of 4T1 tumor-bearing mice with different treatments under laser irradiation (885 nm CW laser, 0.8 W/cm^2), respectively. (**b**) The temperature changes of tumors recorded at different time points as shown in (**a**). (**c-e**) Relative tumor volumes, tumor weight, and bodyweight of mice treated with different administrations. (**f**) H&E stained images of tumors resected from different groups at day 8. (***P < 0.001)

4.3.7 *In vivo* biosafety of CR880-NPs

100 μL of CR880-NPs (0.3 mM) were i.v. injected into healthy C57BL/6 mice and the blood samples were collected on day 7 and 14 to test organ function. There were no evident differences between CR880-NPs treated mice and the PBS-treated mice

from blood biochemistry and hematology data (**Figure 4.10a,b**). The H&E stained images of vital organs (**Figure 4.10c**) also proved no detectable damages or inflammatory lesions to the organs using CR880-NPs. Our results indicate that CR880-NPs have the well toleration and good biocompatibility *in vivo*.
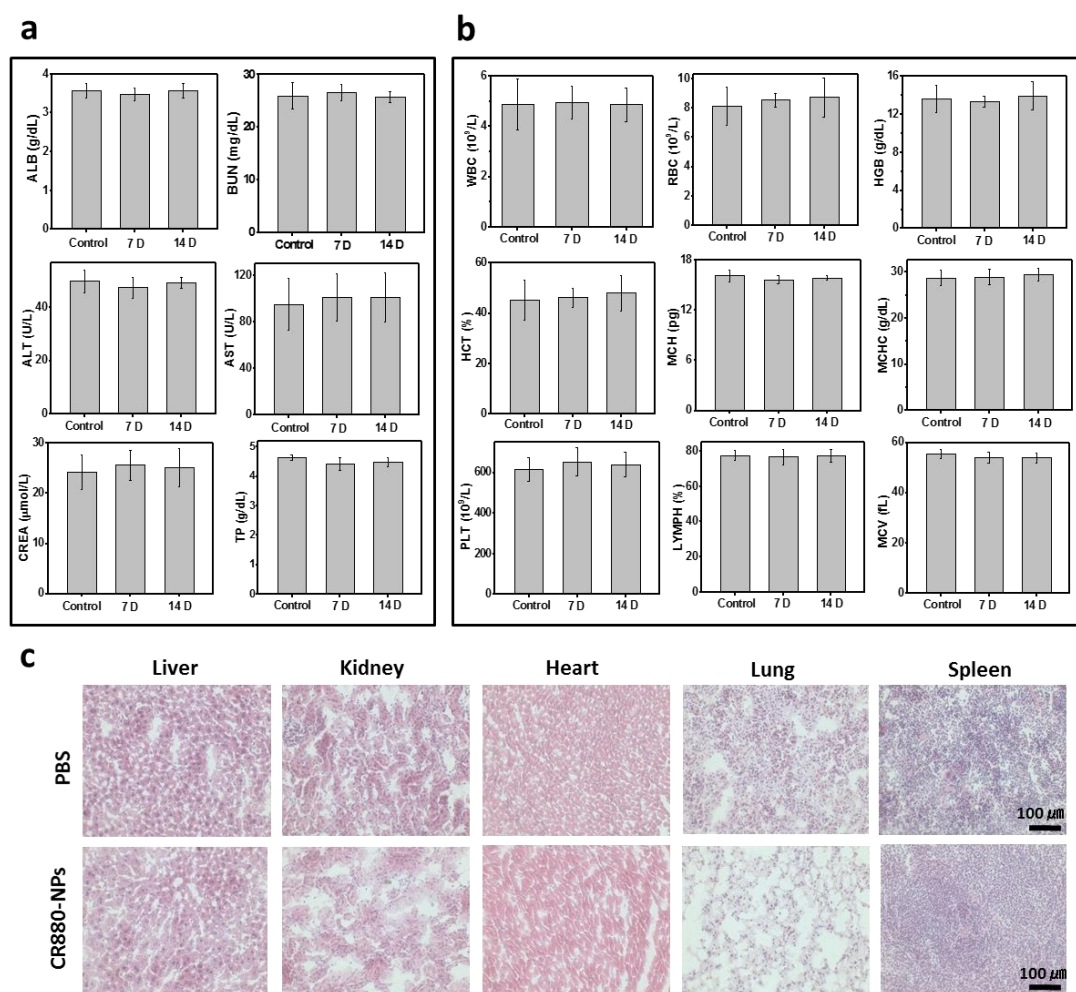
Figure 4.10 (a,b) Blood biochemistry and hematology data of healthy C57BL/6 mice after i.v. injection of CR880-NPs (0.3 mM) or PBS (control). **(c)** Representative H&E stained images of major organs harvested from mice in different groups after 14 days.

4.4 Discussion

Croconaine dye-CR880 having a D-A-D type chromophore was prepared and

converted to a nanoparticle formulation for highly efficient deep tumor optoacoustic imaging and PTT. CR880 is unique having a highly sterically hindered and electron-donating tetraphenylethylene (TPE) core which imparts an unusual property to the croconaine of not blue shifting upon aggregation. Then the formulated CR880-NPs exhibited high OGE, good photostability, and high photothermal conversion efficiency (58.14%). The longer wavelength and high OCE of CR880-NPs bring about the excellent image contrast from deep tissue with minimal background. Based on the EPR effect, CR880-NPs can effectively accumulate to tumor region which be easily detected by optoacoustic imaging. Besides, the superior photothermal performance of CR880-NPs not only allow the high-efficient ablation of cancer cell but also ensure the complete tumor inhibition in live mice. Furthermore, CR880-NPs show the good biocompatibility and non-toxicity on the mice.

In general, organic dyes have problems with solubility in aqueous systems which often limits their biomedical application. Nanoformulation makes it possible to solubilize highly lipophilic organic dyes. In our group, we developed PEGylated liposomes incorporating ICG which showed good tumor accumulation by MSOT imaging.[30] Moreover, we encapsulated the iBu-TSBSH5 dye into QH2 nanoparticles using a flash nanoprecipitation method.[76] Based on our previous work, we used DSPE-PEG2000 to be the nanocarrier to load the hydrophobic CR880. The formulated nanoparticles have a mean size of 45 nm. Due to the nanosize, the CR880-NPs can be easily accumulated at the tumor region based on EPR effect.

When a laser beam illuminates tissue, reflection, scattering, conduction, and absorption can occur. Reflected light accounts for about 4% to 7% of the light, which does not affect the tissue. Scattering occurs in the presence of dermal collagen and gradually decreases with increasing dye wavelength. Light in the NIR range is minimally scattered resulting in deeper tissue penetration. Despite the benefits of using NIR light for tissue imaging, the signal-to-noise ratio and the depth of tissue penetration

remain limited because of absorption by hemoglobin and skin, and residual scattering in this wavelength range. Therefore, longer-wavelength dyes with optimized absorbance profiles remain attractive targets. Most of croconaine dyes or derived nanoparticles have absorption peaks around or below 800nm. On the basis of the tissue-mimicking phantom experiments, the longer wavelength absorption of CR880-NPs enabled good image quality with lower signal-to-noise. Thus different tumor models can be easily detected, even the challenged brain tumor. These results clearly demonstrated the capability of tissue penetration using CR880-NPs.

Optoacoustic imaging resolves tissue images based on intrinsic tissue absorbers of light, such as hemoglobin, water, and lipids. Contrast enhancement can be achieved with agents that exhibit high absorption cross-section, high photostability, low quantum yield, low toxicity, and preferential bio-distribution and clearance profiles. [7, 16] Based on advantageous photophysical properties of croconaine dyes or derived nanoparticles, CR880-NPs exhibits the high-efficient ability to absorb light energy to convert into ultrasonic waves. Meanwhile, the high photostability of CR880-NPs also provides the persistent optoacoustic signal for disease detection. Thus combining with the high-sensitive MSOT systems, optoacoustic imaging of deep tumors can be easily achieved. On the other hand, when contrast agents are irradiated with laser, the generate thermal energy between can be used for PTT of tumors. CR880-NPs show 58.14% of PCE, which much higher than most of PTT agents.[69, 79, 80] This is because most of light energy mainy relases non-radiative energy as heat. Encouraged by the good PTT effect, CR880-NPs shows good cell-killing and tumor inhabitation.

In conclusion, CR880-derived nanoparticles were constructed for efficient optoacoustic imaging of deep tumor and PTT. The formulated CR880-NPs have the advantages of high OGE, high PCE, high photostability, and deep tissue penetration. Thus CR880-NPs could be passively targeted to various deep tumors and be easily detected using optoacoustic imaging. Besides, the superior photothermal property of

CR880-NPs ensured high-efficient cell-killing and tumor elimination. Furthermore, CR880-NPs have no cytotoxicity in vital organs. Therefore, croconaine derived CR880-NPs can be an ideal class of optoacoustic and photothermal agents for cancer theranostics, which also provide a new way for designing NIR light absorbed agents.

5 Conclusion and outlook

As described in this thesis, we synthesized three stable NIR-absorbing croconaine nanoparticles, and then performed the characterization of their photophysical properties and the corresponding biological applications. Specifically, the obtained results can be divided into three parts, as described below.

First, a facile synthesis protocol of CR760 nanoparticles was developed for efficient optoacoustic imaging-guided PTT of subcutaneous tumors. CR760 can be synthesized in one step and then mono-conjugated to a PEG linker and RGD peptide to generate self-assembling nanoparticles. CR760RGD-NPs can generate a stronger optoacoustic signal and more heat than the industry-leading ICG. Due to the passive and active targeting effect, the MSOT system can easily detect the effective accumulation of CR760RGD-NPs in tumors. Meanwhile, the strong photothermal performance of CR760RGD-NPs enabled complete tumor inhibition in mice. Additionally, CR760RGD-NPs also showed good biocompatibility and no obvious toxicity.

Secondly, to achieve efficient optoacoustic imaging of preclinically challenging brain tumors, we developed croconaine-derived CR780 nanoparticles with absorption of slightly longer wavelength, which enables deeper tissue imaging and also avoids an overlap of the optoacoustic spectrum. Through appropriate nanomodification methods and ligand targeting, c(RGDyC) peptide-modified CR780 nanoparticles were developed with uniform size (25 nm), which were able to pass the blood-brain barrier easily and efficiently target the brain tumor areas. Meanwhile, the strong optoacoustic signal generated from CR780RGD-NPs enables a much better detection of deep brain tumors by optoacoustic imaging.

Thirdly, because the absorption peaks of both CR780 and CR760 fall mainly below 800 nm and are still affected by strong background signals from tissue and

hemoglobin, croconaine-derived CR880 nanoparticles with longer absorption wavelengths were developed to enable deeper tissue penetration for tumor imaging and efficient photothermal therapy. The formulated CR880-NPs can produce a much stronger optoacoustic signal compared with ICG. Several models such as agar phantoms, brain tumors, and colon cancer were also used to demonstrate the highly efficient imaging ability from deep tissue. Furthermore, the much higher PCE (58.14%) enabled excellent cell-killing and tumor elimination.

As demonstrated by the three sets of results above, we believe that croconaine-derived nanoparticles can be used effectively for optoacoustic imaging and photothermal therapy. Importantly, there still remains additional work that can be done to refine this into a more systematic system. For example, we are investigating different ligand modifications on croconaine nanoformulations, so that they can be used for the diagnosis of different disease models, such as atherosclerosis, arthritis, etc. Additionally, longer absorption wavelengths of croconaine dye derivatives are worthy of further exploration due to the superior optoacoustic generation and heat production. Synergistic carriers (chemotherapeutic agents, photosensitizers, siRNA) could be co-loaded with croconaine nanoparticles in one single system, thus enabling combination therapy of tumors at lower laser power. We are excited to potentially see the many possibilities of this technology come to fruition in the near future.

Bibliography

[1]   Rosencwaig, A.; Gersho, A. Theory of the photoacoustic effect with solids. *Journal of Applied Physics* **1976**, *47*, 64-69.

[2]   Attia, A. B. E.;Balasundaram, G.;Moothanchery, M.;Dinish, U. S.;Bi, R.;Ntziachristos, V.; Olivo, M. A review of clinical photoacoustic imaging: Current and future trends. *Photoacoustics* **2019**, *16*, 100144.

[3]   Dean-Ben, X. L.;Gottschalk, S.;Mc Larney, B.;Shoham, S.; Razansky, D. Advanced optoacoustic methods for multiscale imaging of in vivo dynamics. *Chemical Society Reviews* **2017**, *46*, 2158-2198.

[4]   Beard, P. Biomedical photoacoustic imaging. *Interface Focus* **2011**, *1*, 602-631.

[5]   Fu, Q.;Zhu, R.;Song, J.;Yang, H.; Chen, X. Photoacoustic Imaging: Contrast Agents and Their Biomedical Applications. *Advanced Materials* **2019**, *31*, e1805875.

[6]   Taruttis, A.; Ntziachristos, V. Advances in real-time multispectral optoacoustic imaging and its applications. *Nature Photonics* **2015**, *9*, 219-227.

[7]   Gujrati, V.;Mishra, A.; Ntziachristos, V. Molecular imaging probes for multi-spectral optoacoustic tomography. *Chemical Communications* **2017**, *53*, 4653-4672.

[8]   Olefir, I.;Ghazaryan, A.;Yang, H.;Malekzadeh-Najafabadi, J.;Glasl, S.;Symvoulidis, P.;O'Leary, V. B.;Sergiadis, G.;Ntziachristos, V.; Ovsepian, S. V. Spatial and Spectral Mapping and Decomposition of Neural Dynamics and Organization of the Mouse Brain with Multispectral Optoacoustic Tomography. *Cell Reports* **2019**, *26*, 2833-2846.

[9]   Reber, J.;Willershauser, M.;Karlas, A.;Paul-Yuan, K.;Diot, G.;Franz, D.;Fromme, T.;Ovsepian, S. V.;Beziere, N.;Dubikovskaya, E.;Karampinos, D. C.;Holzapfel, C.;Hauner, H.;Klingenspor, M.; Ntziachristos, V. Non-invasive Measurement of Brown Fat Metabolism Based on Optoacoustic Imaging of Hemoglobin Gradients. *Cell Metabolism* **2018**, *27*, 689-701.

[10]   Aguirre, J.;Schwarz, M.;Garzorz, N.;Omar, M.;Buehler, A.;Eyerich, K.; Ntziachristos, V. Precision assessment of label-free psoriasis biomarkers with ultra-broadband optoacoustic mesoscopy. *Nature Biomedical Engineering* **2017**, *1*.

[11]   Liapis, E.;Klemm, U.;Karlas, A.;Reber, J.; Ntziachristos, V. Resolution of spatial and temporal heterogeneity in bevacizumab-treated breast tumors by eigenspectra multispectral optoacoustic tomography. *Cancer Research* **2020**, *80*, 5291-5304.

[12]   Tzoumas, S.;Nunes, A.;Olefir, I.;Stangl, S.;Symvoulidis, P.;Glasl, S.;Bayer, C.;Multhoff, G.; Ntziachristos, V. Eigenspectra optoacoustic tomography

achieves quantitative blood oxygenation imaging deep in tissues. *Nature Communications* **2016**, *7*, 12121.

[13]   Herzog, E.;Taruttis, A.;Beziere, N.;Lutich, A. A.;Razansky, D.; Ntziachristos, V. Optical imaging of cancer heterogeneity with multispectral optoacoustic tomography. *Radiology* **2012**, *263*, 461-468.

[14]   Zhang, H. F.;Maslov, K.;Stoica, G.; Wang, L. V. Functional photoacoustic microscopy for high-resolution and noninvasive in vivo imaging. *Nature Biotechnology* **2006**, *24*, 848-851.

[15]   Guggenheim, J. A.;Allen, T. J.;Plumb, A.;Zhang, E. Z.;Rodriguez-Justo, M.;Punwani, S.; Beard, P. C. Photoacoustic imaging of human lymph nodes with endogenous lipid and hemoglobin contrast. *Journal of Biomedical Optics* **2015**, *20*, 50504.

[16]   Weber, J.;Beard, P. C.; Bohndiek, S. E. Contrast agents for molecular photoacoustic imaging. *Nature Methods* **2016**, *13*, 639-650.

[17]   Wang, S.;Lin, J.;Wang, T.;Chen, X.; Huang, P. Recent Advances in Photoacoustic Imaging for Deep-Tissue Biomedical Applications. *Theranostics* **2016**, *6*, 2394-2413.

[18]   Du, Y.;Jiang, Q.;Beziere, N.;Song, L.;Zhang, Q.;Peng, D.;Chi, C.;Yang, X.;Guo, H.;Diot, G.;Ntziachristos, V.;Ding, B.; Tian, J. DNA-Nanostructure-Gold-Nanorod Hybrids for Enhanced In Vivo Optoacoustic Imaging and Photothermal Therapy. *Advanced Materials* **2016**, *28*, 10000-10007.

[19]   Song, M.;Liu, N.;He, L.;Liu, G.;Ling, D.;Su, X.; Sun, X. Porous hollow palladium nanoplatform for imaging-guided trimodal chemo-, photothermal-, and radiotherapy. *Nano Research* **2018**, *11*, 2796-2808.

[20]   Ju, Y.;Zhang, H.;Yu, J.;Tong, S.;Tian, N.;Wang, Z.;Wang, X.;Su, X.;Chu, X.;Lin, J.;Ding, Y.;Li, G.;Sheng, F.; Hou, Y. Monodisperse Au-Fe2C Janus Nanoparticles: An Attractive Multifunctional Material for Triple-Modal Imaging-Guided Tumor Photothermal Therapy. *ACS Nano* **2017**, *11*, 9239-9248.

[21]   Pang, B.;Zhao, Y.;Luehmann, H.;Yang, X.;Detering, L.;You, M.;Zhang, C.;Zhang, L.;Li, Z. Y.;Ren, Q.;Liu, Y.; Xia, Y. ^{64}Cu-Doped PdCu@Au Tripods: A Multifunctional Nanomaterial for Positron Emission Tomography and Image-Guided Photothermal Cancer Treatment. *ACS Nano* **2016**, *10*, 3121-3131.

[22]   Huang, X.; El-Sayed, M. A. Gold nanoparticles: Optical properties and implementations in cancer diagnosis and photothermal therapy. *Journal of Advanced Research* **2010**, *1*, 13-28.

[23]   De la Zerda, A.;Zavaleta, C.;Keren, S.;Vaithilingam, S.;Bodapati, S.;Liu, Z.;Levi, J.;Smith, B. R.;Ma, T. J.;Oralkan, O.;Cheng, Z.;Chen, X.;Dai, H.;Khuri-Yakub, B. T.; Gambhir, S. S. Carbon nanotubes as photoacoustic molecular imaging agents in living mice. *Nature Nanotechnology* **2008**, *3*, 557-562.

[24]   Yoo, J. M.;Kang, J. H.; Hong, B. H. Graphene-based nanomaterials for versatile

imaging studies. *Chemical Society Reviews* **2015**, *44*, 4835-4852.

[25] Li, Y. F.; Chen, C. Fate and toxicity of metallic and metal-containing nanoparticles for biomedical applications. *Small* **2011**, *7*, 2965-2980.

[26] Cai, Y.;Si, W.;Huang, W.;Chen, P.;Shao, J.; Dong, X. Organic Dye Based Nanoparticles for Cancer Phototheranostics. *Small* **2018**, *14*, e1704247.

[27] Laramie, M. D.;Smith, M. K.;Marmarchi, F.;McNally, L. R.; Henary, M. Small Molecule Optoacoustic Contrast Agents: An Unexplored Avenue for Enhancing In Vivo Imaging. *Molecules* **2018**, *23*, 2766.

[28] Chen, Z.;Dean-Ben, X. L.;Gottschalk, S.; Razansky, D. Performance of optoacoustic and fluorescence imaging in detecting deep-seated fluorescent agents. *Biomedical Optics Express* **2018**, *9*, 2229-2239.

[29] Huang, P.;Rong, P.;Jin, A.;Yan, X.;Zhang, M. G.;Lin, J.;Hu, H.;Wang, Z.;Yue, X.;Li, W.;Niu, G.;Zeng, W.;Wang, W.;Zhou, K.; Chen, X. Dye-loaded ferritin nanocages for multimodal imaging and photothermal therapy. *Advanced Materials* **2014**, *26*, 6401-6408.

[30] Beziere, N.;Lozano, N.;Nunes, A.;Salichs, J.;Queiros, D.;Kostarelos, K.; Ntziachristos, V. Dynamic imaging of PEGylated indocyanine green (ICG) liposomes within the tumor microenvironment using multi-spectral optoacoustic tomography (MSOT). *Biomaterials* **2015**, *37*, 415-424.

[31] Sreejith, S.;Joseph, J.;Lin, M.;Menon, N. V.;Borah, P.;Ng, H. J.;Loong, Y. X.;Kang, Y.;Yu, S. W.-K.; Zhao, Y. Near-Infrared Squaraine Dye Encapsulated Micelles for in Vivo Fluorescence and Photoacoustic Bimodal Imaging. *ACS Nano* **2015**, *9*, 5695-5704.

[32] Anees, P.;Joseph, J.;Sreejith, S.;Menon, N. V.;Kang, Y.;Wing-Kwong Yu, S.;Ajayaghosh, A.; Zhao, Y. Real time monitoring of aminothiol level in blood using a near-infrared dye assisted deep tissue fluorescence and photoacoustic bimodal imaging. *Chemical Science* **2016**, *7*, 4110-4116.

[33] Zhang, Y.;Feng, L.;Wang, J.;Tao, D.;Liang, C.;Cheng, L.;Hao, E.; Liu, Z. Surfactant-Stripped Micelles of Near Infrared Dye and Paclitaxel for Photoacoustic Imaging Guided Photothermal-Chemotherapy. *Small* **2018**, *14*, e1802991.

[34] Chen, L.;Chen, D.;Jiang, Y.;Zhang, J.;Yu, J.;DuFort, C. C.;Hingorani, S. R.;Zhang, X.;Wu, C.; Chiu, D. T. A BODIPY-Based Donor/Donor-Acceptor System: Towards Highly Efficient Long-Wavelength-Excitable Near-IR Polymer Dots with Narrow and Strong Absorption Features. *Angewandte Chemie International Edition* **2019**, *58*, 7008-7012.

[35] Nyman, E. S.; Hynninen, P. H. Research advances in the use of tetrapyrrolic photosensitizers for photodynamic therapy. *Journal of Photochemistry and Photobiology B: Biology* **2004**, *73*, 1-28.

[36] Overchuk, M.;Zheng, M.;Rajora, M. A.;Charron, D. M.;Chen, J.; Zheng, G. Tailoring Porphyrin Conjugation for Nanoassembly-Driven Phototheranostic

Properties. *ACS Nano* **2019**, *13*, 4560-4571.

[37]   Cheng, L.;Jiang, D.;Kamkaew, A.;Valdovinos, H. F.;Im, H. J.;Feng, L.;England, C. G.;Goel, S.;Barnhart, T. E.;Liu, Z.; Cai, W. Renal-Clearable PEGylated Porphyrin Nanoparticles for Image-guided Photodynamic Cancer Therapy. *Advance Functional Materials* **2017**, *27*, 1702928.

[38]   Lynch, D. E.; Hamilton, D. G. Croconaine Dyes - the Lesser Known Siblings of Squaraines. *European journal of Organic Chemistry* **2017**, *2017*, 3897-3911.

[39]   Yang, Q.;Peng, C.;Ren, J.;Zhao, W.;Zheng, W.;Zhang, C.;Hu, Y.; Zhang, X. A Near‐Infrared Photoactuator Based on Shape Memory Semicrystalline Polymers toward Light‐Fueled Crane, Grasper, and Walker. *Advanced Optical Materials* **2019**, *7*, 1900784.

[40]   Liu, L.;Liu, M. H.;Deng, L. L.;Lin, B. P.; Yang, H. Near-Infrared Chromophore Functionalized Soft Actuator with Ultrafast Photoresponsive Speed and Superior Mechanical Property. *Journal of the American Chemical Society* **2017**, *139*, 11333-11336.

[41]   Xu, Z.;Zhang, C.;Zheng, X.;Li, Z.; Xu, S. A highly sensitive and selective optical probe for detection of Hg^{2+} based on a 2,5-bis[2-(benzylthio)aniline]-croconaine. *Optik* **2018**, *175*, 54-62.

[42]   Ye, S.;Zhang, C.;Mei, J.;Li, Z.;Xu, S.;Li, X.; Yao, C. A highly selective optical probe for sensing of Fe^{3+} based on a water-soluble croconaine. *Journal of Photochemistry and Photobiology A: Chemistry* **2017**, *347*, 130-137.

[43]   Zhang, X.;Li, C.;Cheng, X.;Wang, X.; Zhang, B. A near-infrared croconium dye-based colorimetric chemodosimeter for biological thiols and cyanide anion. *Sensors and Actuators B: Chemical* **2008**, *129*, 152-157.

[44]   Avirah, R. R.;Jyothish, K.; Ramaiah, D. Infrared Absorbing Croconaine Dyes: Synthesis and Metal Ion Binding Properties. *The Journal of Organic Chemistry* **2008**, *73*, 274-279.

[45]   Chen, G.;Sun, J.;Peng, Q.;Sun, Q.;Wang, G.;Cai, Y.;Gu, X.;Shuai, Z.; Tang, B. Z. Biradical-Featured Stable Organic-Small-Molecule Photothermal Materials for Highly Efficient Solar-Driven Water Evaporation. *Advanced Materials* **2020**, 1908537.

[46]   Lei, S.;Zhang, Y.;Blum, N. T.;Huang, P.; Lin, J. Recent Advances in Croconaine Dyes for Bioimaging and Theranostics. *Bioconjugate Chemistry* **2020**, *9*, 2072-2084.

[47]   Capozzi, M. A. M.;Punzi, A.;Babudri, F.;Musio, R.; Farinola, G. M. Synthesis and Computational Study of Semicroconaines and non-Symmetric Croconaines. *The Journal of Organic Chemistry* **2018**, *83*, 14396-14405.

[48]   Spence, G. T.;Hartland, G. V.; Smith, B. D. Activated photothermal heating using croconaine dyes. *Chemical Science* **2013**, *4*, 4240.

[49]   Demchenko, A. Photobleaching of organic fluorophores: Quantitative characterization, mechanisms, protection. *Methods and Applications in*

Fluorescence **2020**, *8*, 022001.

[50]   Harmatys, K. M.;Battles, P. M.;Peck, E. M.;Spence, G. T.;Roland, F. M.; Smith, B. D. Selective photothermal inactivation of cells labeled with near-infrared croconaine dye. *Chemical Communications* **2017**, *53*, 9906-9909.

[51]   Song, X.; Foley, J. W. A new water-soluble near-infrared croconium dye. *Dyes and Pigments* **2008**, *78*, 60-64.

[52]   Encinas, C.;Otazo, E.;Rivera, L.;Miltsov, S.; Alonso, J. Croconines: new acidochromic dyes for the near infrared region. *Tetrahedron Letters* **2002**, *43*, 8391-8393.

[53]   Tian, M.;Tatsuura, S.;Furuki, M.;Sato, Y.;Iwasa, I.; Pu, L. S. Discovery of Novel Dyes with Absorption Maxima at 1.1 μm. *Journal of the American Chemical Society* **2003**, *125*, 348-349.

[54]   Tang, L.;Zhang, F.;Yu, F.;Sun, W.;Song, M.;Chen, X.;Zhang, X.; Sun, X. Croconaine nanoparticles with enhanced tumor accumulation for multimodality cancer theranostics. *Biomaterials* **2017**, *129*, 28-36.

[55]   Tang, L.;Sun, X.;Liu, N.;Zhou, Z.;Yu, F.;Zhang, X.;Sun, X.; Chen, X. Radiolabeled Angiogenesis-Targeting Croconaine Nanoparticles for Trimodality Imaging Guided Photothermal Therapy of Glioma. *ACS Applied Nano Materials* **2018**, *1*, 1741-1749.

[56]   Yu, F.;Zhang, F.;Tang, L.;Ma, J.;Ling, D.;Chen, X.; Sun, X. Redox-responsive dual chemophotothermal therapeutic nanomedicine for imaging-guided combinational therapy. *Journal of Materials Chemistry B* **2018**, *6*, 5362-5367.

[57]   Tang, L.;Yang, Z.;Zhou, Z.;Ma, Y.;Kiesewetter, D. O.;Wang, Z.;Fan, W.;Zhu, S.;Zhang, M.;Tian, R.;Lang, L.;Niu, G.;Zhang, X.; Chen, X. A Logic-Gated Modular Nanovesicle Enables Programmable Drug Release for On-Demand Chemotherapy. *Theranostics* **2019**, *9*, 1358-1368.

[58]   Guha, S.;Shaw, G. K.;Mitcham, T. M.;Bouchard, R. R.; Smith, B. D. Croconaine rotaxane for acid activated photothermal heating and ratiometric photoacoustic imaging of acidic pH. *Chemical Communications* **2016**, *52*, 120-123.

[59]   Chen, Q.;Liu, X.;Zeng, J.;Cheng, Z.; Liu, Z. Albumin-NIR dye self-assembled nanoparticles for photoacoustic pH imaging and pH-responsive photothermal therapy effective for large tumors. *Biomaterials* **2016**, *98*, 23-30.

[60]   Liu, Y.;Liu, H.;Yan, H.;Liu, Y.;Zhang, J.;Shan, W.;Lai, P.;Li, H.;Ren, L.;Li, Z.; Nie, L. Aggregation-Induced Absorption Enhancement for Deep Near-Infrared II Photoacoustic Imaging of Brain Gliomas In Vivo. *Advanced Science* **2019**, *6*, 1801615.

[61]   Liu, H.;Wang, X.;Huang, Y.;Li, H.;Peng, C.;Yang, H.;Li, J.;Hong, H.;Lei, Z.;Zhang, X.; Li, Z. Biocompatible Croconaine Aggregates with Strong 1.2–1.3 μm Absorption for NIR-IIa Photoacoustic Imaging in Vivo. *ACS Applied Materials & Interfaces* **2019**, *11*, 30511-30517.

[62] Ng, K. K.; Zheng, G. Molecular Interactions in Organic Nanoparticles for Phototheranostic Applications. *Chemical Reviews* **2015**, *115*, 11012-11042.

[63] Jokerst, J. V.; Gambhir, S. S. Molecular Imaging with Theranostic Nanoparticles. *Accounts of Chemical Research* **2011**, *44*, 1050-1060.

[64] Zhu, H.;Cheng, P.;Chen, P.; Pu, K. Recent progress in the development of near-infrared organic photothermal and photodynamic nanotherapeutics. *Biomaterials Science* **2018**, *6*, 746-765.

[65] Gujrati, V.;Prakash, J.;Malekzadeh-Najafabadi, J.;Stiel, A.;Klemm, U.;Mettenleiter, G.;Aichler, M.;Walch, A.; Ntziachristos, V. Bioengineered bacterial vesicles as biological nano-heaters for optoacoustic imaging. *Nature Communications* **2019**, *10*, 1114.

[66] Liu, Y.;Bhattarai, P.;Dai, Z.; Chen, X. Photothermal therapy and photoacoustic imaging via nanotheranostics in fighting cancer. *Chemical Society Reviews* **2019**, *48*, 2053-2108.

[67] Ntziachristos, V.; Razansky, D. Molecular Imaging by Means of Multispectral Optoacoustic Tomography (MSOT). *Chemical Reviews* **2010**, *110*, 2783-2794.

[68] Zou, L.;Wang, H.;He, B.;Zeng, L.;Tan, T.;Cao, H.;He, X.;Zhang, Z.;Guo, S.; Li, Y. Current Approaches of Photothermal Therapy in Treating Cancer Metastasis with Nanotherapeutics. *Theranostics* **2016**, *6*, 762-772.

[69] Jung, H. S.;Verwilst, P.;Sharma, A.;Shin, J.;Sessler, J. L.; Kim, J. S. Organic molecule-based photothermal agents: an expanding photothermal therapy universe. *Chemical Society Reviews* **2018**, *47*, 2280-2297.

[70] Zhang, R.;Xia, Z.;Spivack, J. L.;Gui, J. Y.; Lei, H. Organic dye compositions and use thereof in photovoltaic cells. *European Patent 1752497A2* **2008**.

[71] Rurack, K.; Spieles, M. Fluorescence quantum yields of a series of red and near-infrared dyes emitting at 600-1000 nm. *Analytical Chemistry* **2011**, *83*, 1232-1242.

[72] Fuenzalida Werner, J. P.;Huang, Y.;Mishra, K.;Janowski, R.;Vetschera, P.;Heichler, C.;Chmyrov, A.;Neufert, C.;Niessing, D.;Ntziachristos, V.; Stiel, A. C. Challenging a Preconception: Optoacoustic Spectrum Differs from the Optical Absorption Spectrum of Proteins and Dyes for Molecular Imaging. *Analytical Chemistry* **2020**, *92*, 10717-10724.

[73] Roper, D. K.;Ahn, W.; Hoepfner, M. Microscale Heat Transfer Transduced by Surface Plasmon Resonant Gold Nanoparticles. *The Journal of Physical Chemistry C,* **2007**, *111*, 3636-3641.

[74] Fabian, J. TDDFT-calculations of Vis/NIR absorbing compounds. *Dyes and Pigments* **2010**, *84*, 36-53.

[75] Jing, X.;Zhi, Z.;Jin, L.;Wang, F.;Wu, Y.;Wang, D.;Yan, K.;Shao, Y.; Meng, L. pH/redox dual-stimuli-responsive cross-linked polyphosphazene nanoparticles for multimodal imaging-guided chemo-photodynamic therapy. *Nanoscale* **2019**, *11*, 9457-9467.

[76]   Nunes, A.;Pansare, V. J.;Beziere, N.;Ntoukas, A. K.;Reber, J.;Bruzek, M.;Anthony, J.;Prud'homme, R. K.; Ntziachristos, V. Quenched hexacene optoacoustic nanoparticles. *Journal of Materials Chemistry B* **2018**, *6*, 44-55.

[77]   Miao, W.;Kim, H.;Gujrati, V.;Kim, J. Y.;Jon, H.;Lee, Y.;Choi, M.;Kim, J.;Lee, S.;Lee, D. Y.;Kang, S.; Jon, S. Photo-decomposable Organic Nanoparticles for Combined Tumor Optical Imaging and Multiple Phototherapies. *Theranostics* **2016**, *6*, 2367-2379.

[78]   Yuan, A.;Qiu, X.;Tang, X.;Liu, W.;Wu, J.; Hu, Y. Self-assembled PEG-IR-780-C13 micelle as a targeting, safe and highly-effective photothermal agent for in vivo imaging and cancer therapy. *Biomaterials* **2015**, *51*, 184-193.

[79]   Li, X.;Liu, L.;Li, S.;Wan, Y.;Chen, J. X.;Tian, S.;Huang, Z.;Xiao, Y. F.;Cui, X.;Xiang, C.;Tan, Q.;Zhang, X. H.;Guo, W.;Liang, X. J.; Lee, C. S. Biodegradable pi-Conjugated Oligomer Nanoparticles with High Photothermal Conversion Efficiency for Cancer Theranostics. *ACS Nano* **2019**, *13*, 12901-12911.

[80]   Gao, D.;Zhang, B.;Liu, Y.;Hu, D.;Sheng, Z.;Zhang, X.; Yuan, Z. Molecular Engineering of Near-Infrared Light-Responsive BODIPY-Based Nanoparticles with Enhanced Photothermal and Photoacoustic Efficiencies for Cancer Theranostics. *Theranostics* **2019**, *9*, 5315-5331.

[81]   Fomchenko, E. I.; Holland, E. C. Mouse models of brain tumors and their applications in preclinical trials. *Clinical Cancer Research* **2006**, *12*, 5288-5297.

[82]   Balasundaram, G.;Ding, L.;Li, X.;Attia, A. B. E.;Dean-Ben, X. L.;Ho, C. J. H.;Chandrasekharan, P.;Tay, H. C.;Lim, H. Q.;Ong, C. B.;Mason, R. P.;Razansky, D.; Olivo, M. Noninvasive Anatomical and Functional Imaging of Orthotopic Glioblastoma Development and Therapy using Multispectral Optoacoustic Tomography. *Translational Oncology* **2018**, *11*, 1251-1258.

[83]   Deliolanis, N. C.;Ale, A.;Morscher, S.;Burton, N. C.;Schaefer, K.;Radrich, K.;Razansky, D.; Ntziachristos, V. Deep-tissue reporter-gene imaging with fluorescence and optoacoustic tomography: a performance overview. *Molecular imaging and biology* **2014**, *16*, 652-660.

[84]   Tang, W.;Fan, W.;Lau, J.;Deng, L.;Shen, Z.; Chen, X. Emerging blood-brain-barrier-crossing nanotechnology for brain cancer theranostics. *Chemical Society Reviews* **2019**, *48*, 2967-3014.

[85]   Chen, L.;Zeng, D.;Xu, N.;Li, C.;Zhang, W.;Zhu, X.;Gao, Y.;Chen, P. R.; Lin, J. Blood-Brain Barrier- and Blood-Brain Tumor Barrier-Penetrating Peptide-Derived Targeted Therapeutics for Glioma and Malignant Tumor Brain Metastases. *ACS Applied Materials & Interfaces* **2019**, *11*, 41889-41897.

[86]   Arvanitis, C. D.;Ferraro, G. B.; Jain, R. K. The blood–brain barrier and blood–tumour barrier in brain tumours and metastases. *Nature Reviews Cancer* **2020**, *20*, 26-41.

[87]   Ceña, V.; Játiva, P. Nanoparticle crossing of blood–brain barrier: a road to new

therapeutic approaches to central nervous system diseases. *Nanomedicine* **2018**, *13*, 1513-1516.

[88]   Seo, J. W.;Ang, J.;Mahakian, L. M.;Tam, S.;Fite, B.;Ingham, E. S.;Beyer, J.;Forsayeth, J.;Bankiewicz, K. S.;Xu, T.; Ferrara, K. W. Self-assembled 20-nm (64)Cu-micelles enhance accumulation in rat glioblastoma. *Journal of Controlled Release* **2015**, *220*, 51-60.

[89]   Kircher, M. F.;de la Zerda, A.;Jokerst, J. V.;Zavaleta, C. L.;Kempen, P. J.;Mittra, E.;Pitter, K.;Huang, R.;Campos, C.;Habte, F.;Sinclair, R.;Brennan, C. W.;Mellinghoff, I. K.;Holland, E. C.; Gambhir, S. S. A brain tumor molecular imaging strategy using a new triple-modality MRI-photoacoustic-Raman nanoparticle. *Nature Medicine* **2012**, *18*, 829-834.

[90]   Liu, C.;Li, S.;Gu, Y.;Xiong, H.;Wong, W. T.; Sun, L. Multispectral Photoacoustic Imaging of Tumor Protease Activity with a Gold Nanocage-Based Activatable Probe. *Molecular Imaging and Biology* **2018**, *20*, 919-929.

[91]   Liu, C.;Chen, J.;Zhu, Y.;Gong, X.;Zheng, R.;Chen, N.;Chen, D.;Yan, H.;Zhang, P.;Zheng, H.;Sheng, Z.; Song, L. Highly Sensitive MoS_2-Indocyanine Green Hybrid for Photoacoustic Imaging of Orthotopic Brain Glioma at Deep Site. *Nano-micro letters* **2018**, *10*, 48.

[92]   Chen, J.;Liu, C.;Hu, D.;Wang, F.;Wu, H.;Gong, X.;Liu, X.;Song, L.;Sheng, Z.; Zheng, H. Single-Layer MoS2Nanosheets with Amplified Photoacoustic Effect for Highly Sensitive Photoacoustic Imaging of Orthotopic Brain Tumors. *Advanced Functional Materials* **2016**, *26*, 8715-8725.

[93]   Pu, K.;Shuhendler, A. J.;Jokerst, J. V.;Mei, J.;Gambhir, S. S.;Bao, Z.; Rao, J. Semiconducting polymer nanoparticles as photoacoustic molecular imaging probes in living mice. *Nature Nanotechnology* **2014**, *9*, 233-239.

[94]   Guo, L.-X.;Liu, M.-H.;Sayed, S. M.;Lin, B.-P.;Keller, P.;Zhang, X.-Q.;Sun, Y.; Yang, H. A calamitic mesogenic near-infrared absorbing croconaine dye/liquid crystalline elastomer composite. *Chemical Science* **2016**, *7*, 4400-4406.

[95]   Würth, C.;Grabolle, M.;Pauli, J.;Spieles, M.; Resch-Genger, U. Comparison of Methods and Achievable Uncertainties for the Relative and Absolute Measurement of Photoluminescence Quantum Yields. *Analytical Chemistry* **2011**, *83*, 3431-3439.

[96]   Lepore, M.; Delfino, I. Intralipid-Based Phantoms for the Development of New Optical Diagnostic Techniques. *The Open Biotechnology Journal* **2019**, *13*, 163-172.

[97]   Rehman, A.;Ahmad, I.;Rehman, K.;Anwar, S.;Firdous, S.; Nawaz, M. Optical properties measurement of highly diffusive tissue phantoms for biomedical applications. *Laser Physics* **2015**, *25*, 025605.

[98]   Ni, D.;Zhang, J.;Bu, W.;Xing, H.;Han, F.;Xiao, Q.;Yao, Z.;Chen, F.;He, Q.;Liu, J.;Zhang, S.;Fan, W.;Zhou, L.;Peng, W.; Shi, J. Dual-Targeting Upconversion Nanoprobes across the Blood–Brain Barrier for Magnetic

Resonance/Fluorescence Imaging of Intracranial Glioblastoma. *ACS Nano* **2014**, *8*, 1231-1242.

[99] Gujrati, V.;Lee, M.;Ko, Y.-J.;Lee, S.;Kim, D.;Kim, H.;Kang, S.;Lee, S.;Kim, J.; Jeon, H. Bioengineered yeast-derived vacuoles with enhanced tissue-penetrating ability for targeted cancer therapy. *Proceedings of the National Academy of Sciences* **2016**, *113*, 710-715.

[100] Song, Y.;Du, D.;Li, L.;Xu, J.;Dutta, P.; Lin, Y. In Vitro Study of Receptor-Mediated Silica Nanoparticles Delivery across Blood-Brain Barrier. *ACS Applied Materials & Interfaces* **2017**, *9*, 20410-20416.

[101] Burton, N. C.;Patel, M.;Morscher, S.;Driessen, W. H.;Claussen, J.;Beziere, N.;Jetzfellner, T.;Taruttis, A.;Razansky, D.;Bednar, B.; Ntziachristos, V. Multispectral opto-acoustic tomography (MSOT) of the brain and glioblastoma characterization. *NeuroImage* **2013**, *65*, 522-528.

[102] Wang, L.;Yang, P. P.;Zhao, X. X.; Wang, H. Self-assembled nanomaterials for photoacoustic imaging. *Nanoscale* **2016**, *8*, 2488-2509.

[103] Sun, X.;Li, Y.;Liu, T.;Li, Z.;Zhang, X.; Chen, X. Peptide-based imaging agents for cancer detection. *Advanced Drug Delivery Reviews* **2017**, *110-111*, 38-51.

[104] Liu, S. Radiolabeled cyclic RGD peptides as integrin alpha(v)beta(3)-targeted radiotracers: maximizing binding affinity via bivalency. *Bioconjugate Chemistry* **2009**, *20*, 2199-2213.

[105] Razansky, D.;Baeten, J.; Ntziachristos, V. Sensitivity of molecular target detection by multispectral optoacoustic tomography (MSOT). *Medical physics* **2009**, *36*, 939-945.

[106] Zhang, Y.-N.;Poon, W.;Tavares, A. J.;McGilvray, I. D.; Chan, W. C. W. Nanoparticle–liver interactions: Cellular uptake and hepatobiliary elimination. *Journal of Controlled Release* **2016**, *240*, 332-348.

[107] Longmire, M.;Choyke, P. L.; Kobayashi, H. Clearance properties of nano-sized particles and molecules as imaging agents: considerations and caveats. *Nanomedicine* **2008**, *3*, 703-717.

[108] Pandey, P. K.;Sharma, A. K.; Gupta, U. Blood brain barrier: An overview on strategies in drug delivery, realistic in vitro modeling and in vivo live tracking. *Tissue Barriers* **2016**, *4*, e1129476.

[109] Furtado, D.;Bjornmalm, M.;Ayton, S.;Bush, A. I.;Kempe, K.; Caruso, F. Overcoming the Blood-Brain Barrier: The Role of Nanomaterials in Treating Neurological Diseases. *Advanced Materials* **2018**, *30*, 1801362.

[110] Hoshyar, N.;Gray, S.;Han, H.; Bao, G. The effect of nanoparticle size on in vivo pharmacokinetics and cellular interaction. *Nanomedicine* **2016**, *11*, 673-692.

[111] Park, S. J.;Ho, C. J. H.;Arai, S.;Samanta, A.;Olivo, M.; Chang, Y. T. Visualizing Alzheimer's Disease Mouse Brain with Multispectral Optoacoustic Tomography using a Fluorescent probe, CDnir7. *Scientific Reports* **2019**, *9*, 12052.

[112] Li, L.;Pang, X.; Liu, G. Near-Infrared Light-Triggered Polymeric Nanomicelles for Cancer Therapy and Imaging. *ACS Biomaterials Science & Engineering* **2018**, *4*, 1928-1941.

[113] Yang, T.;Liu, L.;Deng, Y.;Guo, Z.;Zhang, G.;Ge, Z.;Ke, H.; Chen, H. Ultrastable Near-Infrared Conjugated-Polymer Nanoparticles for Dually Photoactive Tumor Inhibition. *Advanced Materials* **2017**, *29*, 1700487.

[114] Gai, S.;Yang, G.;Yang, P.;He, F.;Lin, J.;Jin, D.; Xing, B. Recent advances in functional nanomaterials for light–triggered cancer therapy. *Nano Today* **2018**, *19*, 146-187.

[115] Upputuri, P. K.; Pramanik, M. Photoacoustic imaging in the second near-infrared window: a review. *Journal of Biomedical Optics* **2019**, *24*, 1-20.

Publication lists

1. **Nian Liu**, Patrick O'Connor, Vipul Gujrati,* Dimitris Gorpas, Sarah Glasl, Andreas Blutke, Axel Walch, Karin Kleigrewe, Michael Sattler, Oliver Plettenburg, Vasilis Ntziachristos*. Facile synthesis of a croconaine-based nanoformulation for optoacoustic imaging and photothermal therapy. *Advanced Healthcare Materials* 2021, 2002115.

   Nian Liu identified the CR760 dye, developed CR760RGD-NPs, carried nanoparticle characterization (DLS, zeta potential, photophysical properties, optoacoustic signals, photostability, photothermal performance) and cell experiments (MTT assay, AM/PI, cell uptake), whereas *in vivo* experiments (optoacoustic imaging, photothermal therapy, and biosafety) were assisted by Dr. Vipul Gujrati and technician Sarah Glasl. Nian Liu wrote the manuscript with the support from all the authors.

2. **Nian Liu**, Vipul Gujrati*, Jaber Malekzadeh-Najafabadi, Juan Pablo Fuenzalida Werner, Uwe Klemm, Longguang Tang, Zhenyue Chen, Jaya Prakash, Yuanhui Huang, Andre Stiel, Gabriele Mettenleiter, Michaela Aichler, Andreas Blutke, Axel Walch, Karin Kleigrewe, Daniel Razansky, Michael Sattler, Vasilis Ntziachristos*. Croconaine-based nanoparticles enable efficient optoacoustic imaging of murine brain tumors. *Photoacoustics* 2021, 100263.

   Nian Liu identified the CR780 dye, developed CR780RGD-NPs, carried nanoparticle characterization (DLS, Zeta potential, photophysical properties, optoacoustic signals, photostability) and cell experiments (MTT assay, cell uptake, in vitro BBB penetration), whereas in vivo experiments (optoacoustic imaging, and biosafety) were assisted by Dr. Vipul Gujrati and technician Uwe Klemm. Nian Liu wrote the manuscript with the support from all the authors.

3. Zhenyue Chen, Xosé Luís Deán-Ben, **Nian Liu,** Vipul Gujrati, Sven Gottschalk,

Vasilis Ntziachristos, Daniel Razansky*. Concurrent fluorescence and volumetric optoacoustic tomography of nanoagent perfusion and bio-distribution in solid tumors. *Biomedical Optics Express* 2019, *10*, 5093-5102.

Nian Liu prepared and characterized liposome-ICG

International conference

1. **Nian Liu**, Vipul Gujrati, Jaber Malekzadeh-Najafabadi, Juan Pablo Fuenzalida Werner, Yuanhui Huang, Longguang Tang, Jaya Prakash, Zhenyue Chen, Uwe Klemm, Andre C. Stiel, Gabriele Mettenleiter, Michaela Aicheler, Axel Walch, Daniel Razansky, Michael Sattler, Vasilis Ntziachristos. "Croconaine-derived CR780 nanoparticles enable efficient optoacoustic imaging of deep brain tumor" In 15th European Molecular Imaging Meeting-EMIM 2020, Thessaloniki, Greece, 2020. (Oral presentation)

List of abbreviations

MSOT	multi-spectral optoacoustic tomography
OGE	optoacoustic generation efficiency
ICG	indocyanine green
NIR	near-infrared
PDT	photodynamic therapy
D-A-D	donor-acceptor-donor
PEG	polyethylene glycol
HSA	human serum albumin
ROS	reactive oxygen species
PTT	photothermal therapy
PCE	photothermal conversion efficiency
MTT	3-(4,5-dimethylthiazol-2-yl)-2,5-diphenyltetrazolium bromide
calcein-AM	calcein-acetoxymethyl
EthD1	ethidium homodimer-1
DFT	density functional theory
TEM	transmission electron microscopy
DLS	dynamic light scattering
DMA	9,10-dimethylnathracene
H&E	hematoxylin and eosin
i.v.	intravenous
i.t.	intratumoral
ALB	albumin
BUN	blood urea nitrogen
ALT	alanine transferase
AST	aspartate transferase

CREA	creatinine
TP	total protein
WBC	white blood cells
RBC	red blood cells
HGB	hemoglobin
HCT	hematocrit
MCH	mean corpuscular hemoglobin
MCHC	mean corpuscular hemoglobin concentration
PLT	platelet
LYMPH	lymphocytes
MCV	mean corpuscular volume
BBB	blood brain barrier
BBTB	blood brain tumor barrier
PBS	phosphate-buffered saline
FCSI	fluorescence cryosectioning imaging
SD	standard deviations
EPR	enhanced permeability and retention
TPE	tetraphenylethylene

Acknowledgements

During my PhD study, I have received so much help and advice from many individuals that I could be able to successfully complete my thesis with these three projects.

First of all, I would like to thank my supervisor Prof. Vasilis Ntziachristos for giving me the opportunity to be a part of this great team. Thanks for providing me with the excellent platform, project funding, and discussion of scientific ideas that allowed me to focus my projects without any concern. His scientific thinking and attitude has profoundly influenced the way I think about my future career. Thank you very much for your continuous help.

I would also like to thank my first supervisors, Prof. Michael Sattler, and my collaborator, Prof. Oliver Plettenburg, for their useful discussion and supervision of my PhD projects.

Special thanks to my mentor, Dr. Vipul Gujrati, who guided me through all the details of my projects, from the project design, experimental operation, results' discussion, figures' drawing, and paper writing. His rigorous scientific attitude and scientific thinking deeply influenced me and I will continue to learn from him.

I am equally thankful for Dr. Patrick O'Connor's for carrying out the synthesis of various derivatives of croconaine, including CR760, CR880, and other 8 croconaine derivatives. He gave me several inputs on organic chemistry. I also would like to thank Dr. Longguang Tang, my previous colleague in Xiamen University for synthesizing the CR780 dye.

Thanks to my colleagues, Jaber Malekzadeh, Dr. Juan Pablo Fuenzalida Werner, Dr. Jaya Prakash, Yuanhui Huang, Kanuj Mishra, Dr. Dimitris Gorpas, Dr. Andre Stiel, Dr. Doris Bengel, Pia Anzenhofer, Uwe Klemm, Sarah Glasl, Prof. Daniel Razansky, Dr. Zhenyue Chen. Their professional advice helped me a lot for experiments'